Co-funded by the

CEBAMA

➢ (Contract Number: 662147)

Deliverable n° D3.06

Final results and interpretation of the modelling of experiments within CEBAMA

Editors: Andrés Idiart (Amphos 21)

Date of issue of this report: 27.02.2019

Report number of pages: 94

Start date of project: 01/06/2015 Duration: 48 Months

Project co-funded by the European Commission under the Euratom Research and Training Programme on Nuclear Energy within the Horizon 2020 Framework Programme		
Dissemination Level		
PU	Public	X
PP	Restricted to other programme participants (including the Commission Services)	
RE	Restricted to a group specified by the partners of the CEBAMA project	
CO	Confidential, only for partners of the CEBAMA project	

ABSTRACT

The present deliverable D3.06 contains a description of modelling approaches and final results obtained by WP3 partners on the simulation of experiments performed within CEBAMA. Each partner contribution below summarizes the modelling work and presents the most recent results obtained, with application to WP1/WP2 experiments.

1 KIT/ V. Montoya, N. Ait Mouheb, T. Schäfer

Abstract

This contribution gives details of the work undertaken by KIT on WP3, related to the application of geochemical, mass transport and reactive transport modelling to experiments performed by KIT in WP1 and WP2.

1.1 DESCRIPTION OF THE MODELLING WORK

KIT-INE is mainly involved in 3 different and interconnected modelling activities related with the experiments performed in WP1 and WP2:

- Hydration modelling of low-pH cements
- Migration of tritiated water (HTO) and $^{36}Cl^-$ through low-pH cement pastes
- Reactive transport modelling of radionuclides migration in the low-pH cement/clay interface

All these experiments are being performed by KIT-INE.

1.2 HYDRATION MODELLING

The hydration model of 3 low-pH cement pastes manufactured at KIT-INE has been performed by using the Gibbs free energy minimization code GEMS (Wagner et al., 2012; Kulik et al., 2013) and the recently updated thermodynamic database CEMDATA18 (Lothenbach et al., 2019). The final purpose of this modelling work is to use the hydration model as input parameters in a more complex reactive transport model of low-pH cement/bentonite interactions within this same work package (see Section 3).

The solid phases present after 90 days of hydration have been identified experimentally and were described within WP1 (Ait Mouheb et al., 2017, 2018) together with the raw materials characterization which is used as input data. This helps to compare experimental and modelling results. The main hydrated phases identified experimentally are C-S-H and C-A-S-H phases with a Ca:Si ratio between 0.6 - 1.1 and Al:Si ratio of 0.05. Ettringite is present as a minor phase and no portlandite or Friedel's salt are identified. Experimental studies of the iron containing phases is on-going in WP1 and not compared with the model results.

The modelling approach followed is based on coupling a set of kinetic rates (Parrot et al., 1984, Lothenbach et al., 2008) of the dissolution of the raw materials (clinker and silica fume) with thermodynamic calculations between the solution and the hydrates formed (Lothenbach et al., 2014). All other cement constituents, mainly alkali hydroxides and sulphates (gypsum), were not kinetically controlled and therefore assumed to be thermodynamically dissolved.

Although included in the database, kaolinite, gibbsite, quartz, zeolites or crystalline iron phases were not allowed to precipitate in the system. Alkali uptake for Na and K was modelled as ideal solid solutions. Two different C-S-H solid solution models were used and compared: a) the quaternary CSHQ model with 4 different Ca:Si ratio end-members (Kulik et al., 2011) and b) the CNASH_ss model which includes Al and Na in the structure of the C-S-H phases (Myers et al., 2014). Selected results (hydration model of one of the low-pH cement pastes) of both models are presented in Figure 1.1, showing the volume of solids formed as a function of the hydration time for one of the low-pH cement pastes. The hydrates phases after 90 days predicated from both models are: silica-rich C-S-H, ettringite, gypsum, silica fume not reacted and hydrotalcite, as well as traces of monosulfate and monocarbonate. The main differences between both models, are related to the formation of phases containing aluminium. While the CSHQ model predict the formation of

strätlingite and $Al(OH)_3$, the CNASH_ss model predicts the formation of C-A-S-H phases as the only Al-containing phase.

The experimental observations from the solid phase analysis are well reproduced by using the CNASH_ss model. However, the incorporation of the processes controlling the aqueous speciation, especially the potassium concentration is under progress. These results demonstrate that the choice of the appropriate C-S-H model which considers the Al uptake by C-S-H phases is essential to reproduce the hydration phases observed experimentally.

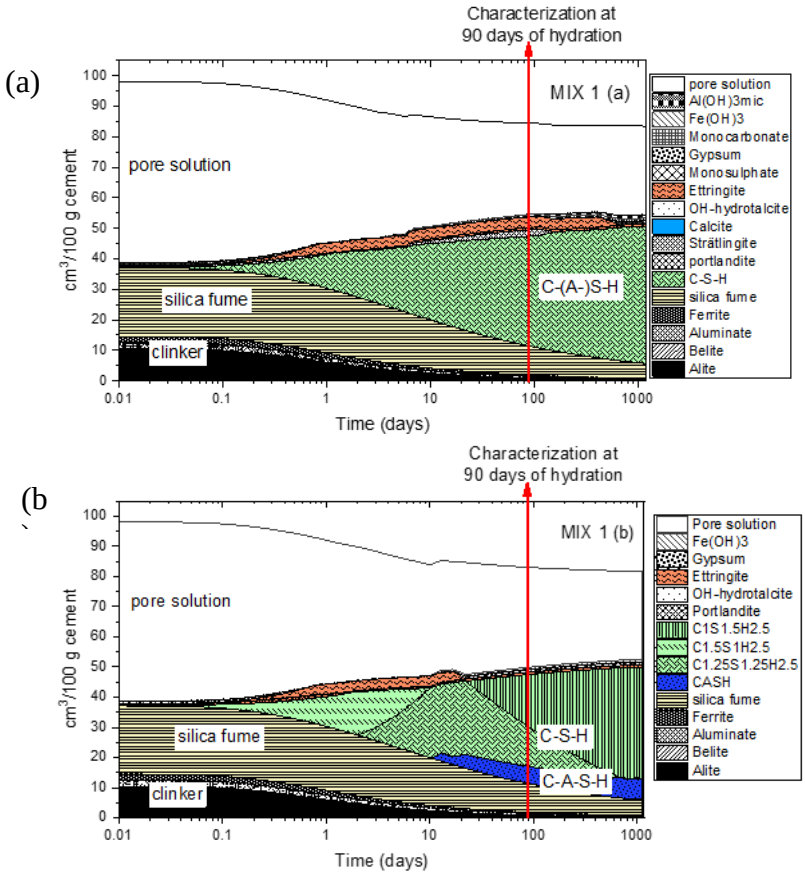

Figure 1.1: *Modelled changes in volume during the hydration of a low-pH cement using: (a) the CSHQ and (b) the CNASH_ss model for C-S-H.*

1.3 MIGRATION OF TRITIATED WATER (HTO) AND $^{36}Cl^-$ THROUGH LOW-pH CEMENTS

Different numerical approximations are used here to determine the effective diffusion coefficient, D_e, and the accessible porosity of tritiated water (HTO) and $^{36}Cl^-$ in 3 low-pH cement pastes. Through-diffusion experiments were performed inside a glove box under a controlled Ar atmosphere at 25°C in WP1, allowing a direct comparison of model and experimental results (Ait Mouheb et al., 2019). Two of the samples (MIX 3C and MIX 3E) have been prepared by mixing different solids (Table 1.1). After 90 days of hydration, they were characterized, mainly chemically, using various complementary analytical techniques (Ait Mouheb et al., 2017, 2018). The third sample corresponds to the reference material of the project (RPM) described in e.g. Vehmas et al. (2017) and Table 1.1. Briefly, the main hydrated phases identified in all the samples are C-S-H and C-A-S-H gels with a Ca:Si ratio between 0.7 - 1.0 and an Al:Si ratio of 0.05. No portlandite or Friedel's salt are present in any of the samples. Unreacted clinker (alite and belite) has also been identified in the RPM sample. The experimental set-up consists on a cylindrical diffusion cell where

a thin cement sample of 10 mm thickness sealed with PMMA is mounted between two compartments, called upstream and downstream reservoirs, with total volumes of 50 mL and 3.8 mL, respectively.

Table 1.1: *Composition (wt.%) of the solid mixtures used to prepare the low pH cement pastes.*

Component	(wt.%)		
	MIX 3C	MIX 3E	RPM
CEM I	39[a]	50	25[b]
Silica fume	39	50	27
Limestone filler	19	-	-
Superplasticizer	3[c]	-	4[d]
Blast furnace slag	-	-	16
Quartz filler	-	-	28
Water/binder ratio	0.6		0.25

[a] CEM I 52.5N SR. [b] CEM I 42.5 MH/SR/LA; [c] Inorganic superplasticizer (SioxX®); [d] Superplasticizer naphthalene-based Pantarhit LK (FM).

Transport parameters for HTO and $^{36}Cl^-$ were obtained by inverse modelling of the diffusive flux data [mol/m^2·s] determined at the downstream reservoir by measuring the accumulated activity (in Bq) of both radionuclides (details on flux calculations are given in Tits et al., 2003). Fickian diffusion in a homogeneous isotropic material has been considered as the only transport process. Fick´s first law states that the diffusive flux (J) is proportional to the concentration gradient:

$$J = -D_e \cdot \frac{\partial c}{\partial x} \tag{1.1}$$

where $\frac{\partial c}{\partial x}$ is the concentration gradient [mol/m^4]; and D_e is the effective diffusion coefficient [m^2/s]. The change of concentration with time, t [s], is described by Fick's second law (Equation 1.2):

$$\frac{\partial c}{\partial \mathrm{t}} = -D_e \cdot \frac{\partial^2 c}{\partial \mathrm{x}^2} \tag{1.2}$$

The effective diffusion coefficient can be estimated using Archie's law:

$$D_e = \varepsilon_{acc}^m \, D_W \tag{1.3}$$

with m [-] being an empirical constant, D_w [m^2/s] the diffusion coefficient of the tracer in free water, and ε_{acc} the accessible porosity [-], which is related to the constrictivity (δ) and tortuosity (τ) factors as:

$$\varepsilon_{acc}^m = \frac{\delta}{\tau} = \frac{1}{G} \tag{1.4}$$

Constrictivity (δ) and tortuosity (τ) are assembled together in the geometrical factor (G). The finite element code Comsol Multiphysics 5.3 (Comsol, 2017) has been used to solve the partial differential equations. Based on the experimental setup, a one-dimensional (1D) single porous medium model is considered. Initial and boundary conditions of the tracer concentration are described according to the measured experimental data:

$c(x = 0, t > 0) = f_0(t)$ and

$c(x = H, t > 0) = f_1(t)$.

Where H (m) is the thickness of the sample. The initial condition is:

$c(x, t \leq 0) = 0, \forall\, x \in$ transport domain

where x [m] is the spatial coordinate, and $f_0(t)$ and $f_1(t)$ are the time-dependent change of the radiotracer concentrations (HTO and $^{36}Cl^-$) in the upstream and downstream reservoir, respectively.

The accumulated amounts (mol) of HTO and $^{36}Cl^-$ in the downstream reservoir of two experiments with the same material are shown in Figure 1.2. The upstream concentration of HTO and $^{36}Cl^-$ are equal to $1.86 \cdot 10^{-9}$ M and $4.55 \cdot 10^{-6}$ M, respectively, and keep approximately constant during the studied time.

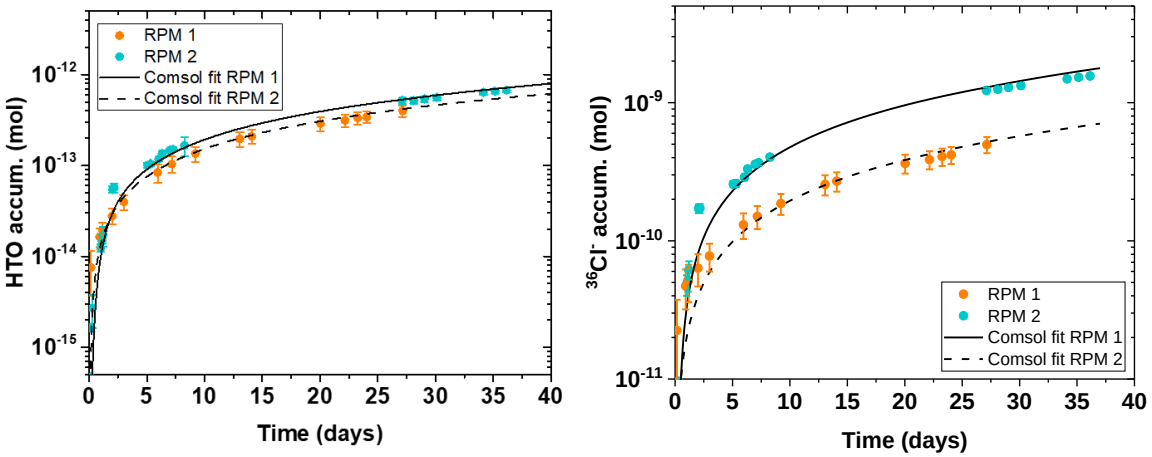

Figure 1.2: *Accumulated amount of HTO and $^{36}Cl^-$ in the downstream reservoir vs. time during diffusion experiments through two low-pH cement (RPM) samples.*

Experiments are reproducible and within the first hours the fluxes reached a steady state with a value of ~ $5 \cdot 10^{-16}$ mol·m^{-2}·s^{-1} for HTO and ~ 10^{-13} mol·m^{-2}·s^{-1} for $^{36}Cl^-$. Transport parameters values for HTO and $^{36}Cl^-$ were obtained (average of two samples) with D_e (HTO) = (2.28 ± 0.22)·10^{-12} m^2/s, ε_{acc} (HTO) = 0.004± 0.009 and D_e ($^{36}Cl^-$) = (1.55± 6.74)·10^{-12} m^2/s, ε_{acc} ($^{36}Cl^-$) = 0.002± 0.009. As observed, to obtain a good fit of the experimental data a very small (unrealistic) accessible porosity was needed. These findings indicate that the porosity-effective diffusion correlation, which is generally described by empirical laws such as Archie´s law with m values expected for the studied material is not applicable or other transport processes are occurring in the system. This could probably be due to the heterogeneous small pore scale (< 10 nm) network. Future work focuses on the fitting of the experimental data with a more complex multiporosity approach model.

1.4 REACTIVE TRANSPORT MODELLING OF RADIONUCLIDES MIGRATION IN LOW-pH CEMENT/CLAY INTERFACES

A predictive reactive transport model consisting of a three-dimensional (3D) fully water saturated isothermal (298.15 K) system has been performed. This modelling work represents laboratory through-diffusion experiments of HTO, Be(II), and $^{36}Cl^-$ across the interface between MX-80 bentonite porewater and low-pH cement (see Figure 1.3) performed in KIT (WP1). Coupling between porosity changes due to dissolution/precipitation reactions and transport properties (i.e. effective diffusion coefficient) is also studied.

A schematic representation of the diffusion experiments is presented in Figure 1.3. Diffusion of the selected tracers occurs across the interface between bentonite porewater and different low-pH cements manufactured by KIT-INE within WP1 (Ait Mouheb et al., 2017) or available as reference material in the project. The cylindrical low-pH cement paste has a diameter and thickness of 30 and 10 mm, respectively, and it is surrounded by 2 reservoirs of 50 ml and 4 ml: the upstream and downstream reservoirs, containing bentonite and low-pH cement porewater, respectively. The reactive transport simulations are compared to the mentioned through-diffusion experiments performed in WP1. Considerable effort has been made in both WP1 and WP2 to obtain the required

input parameters for the reactive transport model. Among others, the main input parameters that can be obtained from WP1 and WP2 are the pH cement mineralogy, porewater composition, porosity, diffusivity and the aqueous speciation and sorption properties of Be. A large part of the chemical and physical characterization of the cement paste is already documented in Ait Mouheb et al. (2017, 2018) and Gaona et al. (2017, 2019).

The conceptual and numerical model has been set up by using the iCP interface (Nardi et al. 2014). Kinetics and chemical equilibria reactions of the primary and secondary phases precipitating or dissolving in the system are simulated using parameters and data from the appropriate thermodynamic database (i.e. ThermoChimie v.9) and the literature (Giffaut et al., 2014, Gaona et al., 2019). Davies equation is used for the aqueous model and ion exchange reactions for Ca, Mg, Sr, Na and K and radionuclide and iron (III) inner-sphere sorption is considered using a non-electrostatic model. The simulations were carried out for different times of interaction (11 h, 6 months, and 1 year) predicting different processes that could affect differently the mobility of the studied radionuclides.

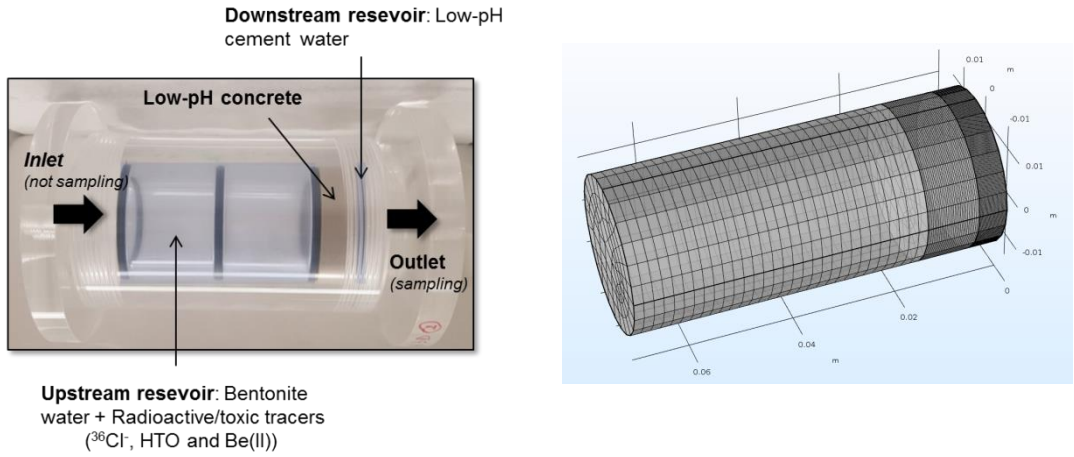

Figure 1.3. *Cell used in the laboratory through diffusion experiments (left) and the spatial discretization used in the model (right). Domain length 70. 13 / 10 / 5.37 mm in the flow direction.*

Figure 1.4. shows some of the processes occurring in the system. The alteration on the low-pH cement by the bentonite water is mainly due to the displacement of the Ca^{2+} in the interlayer of the C-(A)-S-H phases by the Na^+ present in the bentonite water. This process release calcium to the solution producing the formation of secondary phases like gypsum in the cement paste which can be observed after 1 year of interaction as reactive front of 1.75 mm. In our system, brucite is undersaturated and attempts to model the magnesium perturbation using available thermodynamic data suggested the formation of hydrotalcite. The partial dissolution of C-(A)-S-H phases results in an increase in porosity at the side of cement close to the outlet, which is produced by the continuous replacement by "fresh water" in the outlet reservoir. On the other hand, in the cement in contact with the bentonite water, no significant changes of porosity are observed, and the effective diffusion coefficient remains approximately constant, not affecting the transport of a non-reactive and uncharged tracer like tritiated water (HTO).

Finally, the diffusion of beryllium from the bentonite porewater to the low-pH cement is modelled observing that beryllium will remain close to the inlet even after 1 year of interaction, which is mainly due to the strong sorption of this toxic element in low-pH cements.

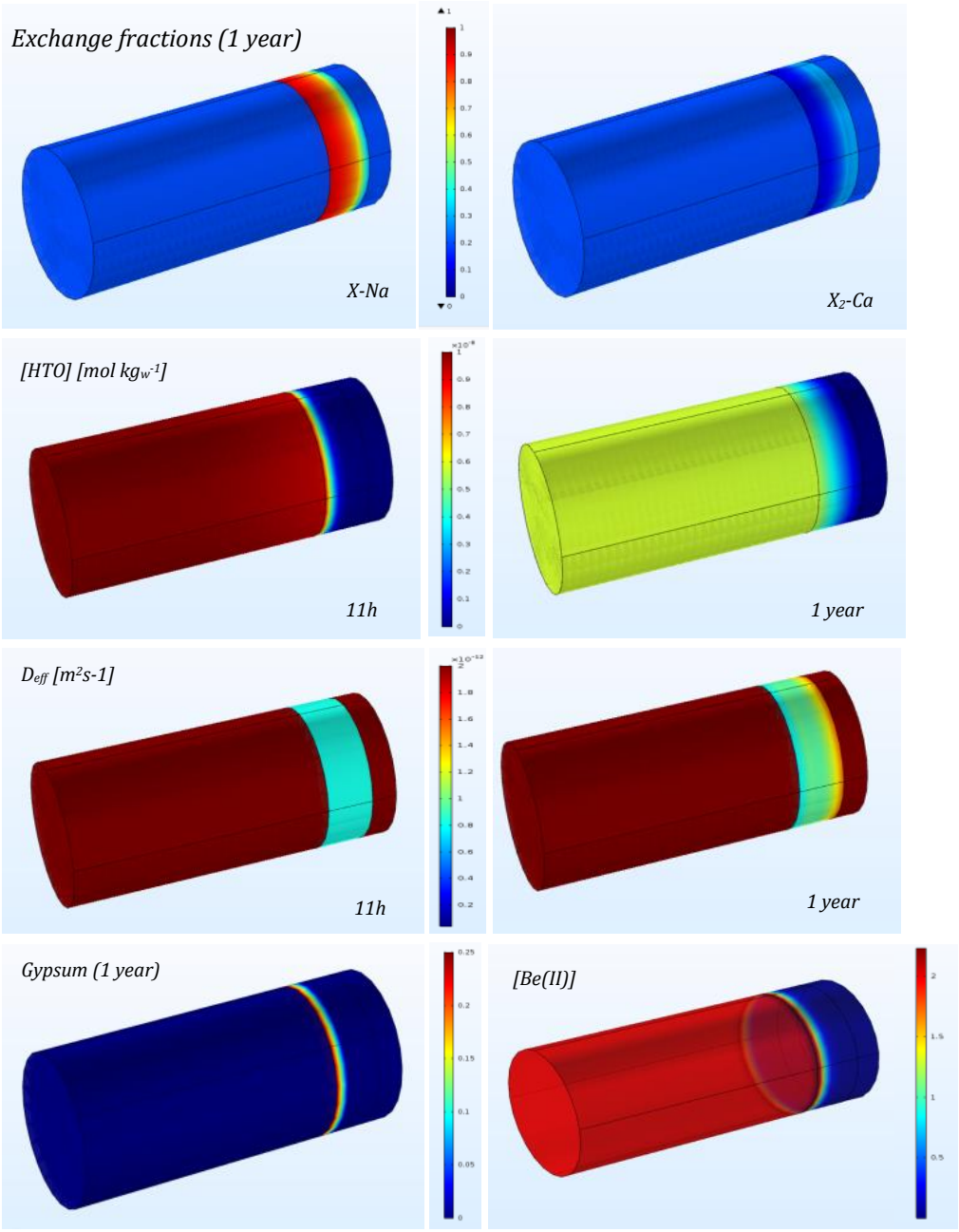

Figure 1.4: *Selected model results obtained using iCP 1.5 (interface COMSOL 5.3-PHREEQC 3.4).*

1.5 CONCLUSION AND MAIN OUTCOMES

The main conclusions from the work presented here are:

Hydration modelling: The choice of the appropriate C-S-H model which considers the Al uptake by C-S-H phases is essential to reproduce the hydration phases observed experimentally.

Migration of tritiated water (HTO) and $^{36}Cl^-$ through low-pH cements: To obtain a good fit of the through-diffusion experiments a very small (unrealistic) accessible porosity is needed in the model. These findings indicate that the porosity-effective diffusion correlation, which is generally described by empirical laws such as Archie´s law with m values expected for the studied materials is not applicable or other transport processes are happening in the system, probably due to the

heterogeneous small pore scale (< 10 nm) network. Future work focuses on the fitting of the experimental data with a more complex multiporosity approach model.

Reactive transport modelling of radionuclides migration in the low-pH cement/clay interface: The simulations predict that the boundaries (inlet, outlet) induce different chemical processes in both sides of the low-pH cement paste sample. For example, sodium present in the bentonite water induce the release of Ca2+ from the low-pH cement paste to the cementitious water. No significant changes of porosity are appreciated in the "inlet" compare to the cement close to the outlet. Beryllium migration in low-pH concretes is mainly dominated by its strong affinity to C-S-H phases and not by transport processes.

Acknowledgements

The research leading to these results has received funding from the European Union's Horizon 2020 Research and Training Programme of the European Atomic Energy Community (EURATOM) (H2020-NFRP-2014/2015) under grant agreement n° 662147 (CEBAMA).

1.6 REFERENCES

Ait Mouheb, N., Montoya, V., Borkel, C., Schäfer, T. (2017). Experimental studies on low pH cement / clay interface processes: Characterization of low pH cements. In 1st Annual proceedings of the Cebama project. KIT Scientific report 7734, Karlsruhe, Germany

Ait Mouheb, N., Montoya, V., Joseph, C., Schäfer, T., Geckeis H. (2019). 3rd Annual proceedings of the Cebama project. KIT Scientific Report (CEBAMA proceedings in print)

Ait Mouheb, N., Montoya, V., Schild, D., Soballa, E., Adam, C., Geyer, F. Schäfer, T. (2018). Characterization and sorption properties of low pH cements. 2nd Annual proceedings of the Cebama project. KIT Scientific report 7734

COMSOL 5.3. (2017). www.comsol.com.

Gaona, X., Böttle M., Rabung T., Altmaier M (2017). Solubility, hydrolysis and sorption of beryllium in cementitious systems. 1st Annual proceedings of the Cebama project KIT scientific report 7734.

Gaona, X., Cevirim-Papaioannou, N., Böttle, M., Altmaier, M. (2019). Solubility and hydrolysis of Be(II) in dilute to concentrated NaCl and KCl solutions. In: M. Altmaier, V. Montoya, L. Duro, A. Valls (Eds.) Proceedings of the 3rd Annual Workshop of the CEBAMA Project. In press

Giffaut, E., Grivé, M., Blanc, P., Vieillard, P., Colàs, E., Gailhanou, H., Gaboreauc, S., Marty, N., Madé, B., Duro, L. (2014). Andra thermodynamic database for performance assessment: ThermoChimie. Applied Geochemistry, 49, 225–236.

Kulik, D.A. (2011). Improving the structural consistency of C-S-H solid solution thermodynamic models. Cem. Concr. Res. 41, 477-495.

Kulik D.A, Wagner, T., Dmytrieva, S.V. Kosakowski, G., Hingerl, F. F., Chudnenko, K. V., Berner, U.R. (2013). GEM-Selektor geochemical modeling package: revised algorithm and GEMS3K numerical kernel for coupled simulation codes. Comput. Geosci. 17, 1-24.

Lothenbach, B., Kulik D.A, Matschei, T., Balonis M., Baquerizo, L, Dilnesa B., Miron, G.D., Myers, R.J. (2019). Cemdata18: A chemical thermodynamic database for hydrated Portland cements and alkali-activated materials. Cem. Concr. Res. 115, 472-506

Lothenbach, B., Le Saout G., Gallucci, E., Scrivener, K. (2008). Influence of limestone on the hydration of Portland cements. Cem. Concr. Res. 38 848-860

Lothenbach, B., Rentsch, D., Wieland, E. (2014). Hydration of a silica fume blended shotcrete cement. Phys. Chem. Earth, 70-71, 3-16

Myers, R.J.; Bernal, S.A.; Provis, J.L. (2014). A thermodynamic model for C-(N-)A-S-H gel: CNASH_ss. Derivation and validation, Cem. Concr. Res. 66,27–47.

Nardi, A., Idiart, A., Trinchero, P., de Vries, L. M., Molinero, J. (2014). Interface COMSOL-PHREEQC (iCP), an efficient numerical framework for the solution of coupled multiphysics and geochemistry. Computers & Geosciences 69, 10-21.

Parrot, L.J., Killoh, D.C. (1984). Prediction of cement hydration. Brit Ceram Proc., 35, 41–53.

Tits, J., Jakob, A., Wieland, E., and Spieler, P. (2003). Diffusion of tritiated water and $^{22}Na^{+}$ through non-degraded hardened cement pastes. J. Contam. Hydrol., 61, 45- 62.

Vehmas, T., Schindler, A., Löija, M., Leivo, M., Holt, E. (2017). Reference mix design and castings for low-pH concrete for nuclear waste repositories. In Altmaier et al. (eds). Proc. 1st Annual Workshop of Cebama –project, KIT Scientific report 7734, Karlsruhe, Germany.

Wagner, T., Kulik, D.A., Hingerl, F.F., Dmytrieva, S.V. (2012). GEMSelektor geochemical modeling package: TSolMod library and data interface for multicomponent phase models. Can. Mineral. 50, 1173–1195.

2 AMPHOS 21/ M. Laviña, A. Idiart, J. Olmeda

Abstract

This contribution deals with the modelling of hydration and leaching experiments conducted by University of Sheffield (USFD) within WP1 of the CEBAMA project on low-pH cement paste samples. Cement hydration is modelled using a set of kinetic reactions for dissolution of the main unhydrated minerals coupled to thermodynamic equilibrium calculations. The leaching process is modelled by coupling hydration with reactive transport, considering three different types of groundwater. The modelling approach and results of the degradation sequence expected in each case are presented. Comparison with experimental results and implications for their interpretation are discussed.

2.1 INTRODUCTION AND OBJECTIVES

In WP1 of the CEBAMA project, an experimental benchmark low-pH cementitious material has been proposed, referred to as CEBAMA reference mix (e.g. Vehmas et al., 2016). Cement paste and concrete specimens were cast and distributed to interested partners. In addition, the mix components have also been distributed to other partners so that samples can be mixed and cast directly at their own respective laboratories. As a result, a relatively large dataset of the reference mixes characterization is available both for the sound and degraded states.

In this contribution, the focus is on the cement paste samples cast at USFD. The goal of these experiments is to study the degradation of small samples when in contact with synthetic groundwaters of different composition (Vasconcelos et al., 2017). Modelling of these experiments using reactive transport simulations require the knowledge of the composition of the hydrated system at the beginning of the leaching tests. In this work, the hydrated composition of the cement paste is obtained by means of hydration modelling. This approach is based on coupling a set of kinetic reactions of dissolution of the mix components with thermodynamic calculations after the work by Lothenbach et al. (2008). Given the low water-to-solid ratio used in the mixes, it is expected that a significant time is needed to reach a high degree of hydration. Thus, the degradation model couples reactive transport with the hydration scheme. The results of the model are presented in this contribution and the implications of leaching while hydration proceeds are discussed.

2.2 USFD EXPERIMENTS ON CEMENT PASTE

USFD is performing characterization and leaching experiments using two different cementitious systems: the NRVB high-pH cement (Vasconcelos et al., 2017) and a low-pH cement paste mix based on the CEBAMA reference cement (e.g. Vehmas et al., 2016). In this contribution, focus is on the low-pH cement paste. Preliminary experimental results are available in Vasconcelos et al. (2018). The composition of the mix used by USFD to cast cylindrical specimens of 15 mm height and 15 mm diameter is given in Table 2.1. With a water-to-solid ratio of 0.25, it is identical to the CEBAMA reference mix, with the exception that quartz filler has not been added in USFD samples. Moreover, the curing conditions also differ. Samples were cured for 28 days in an oven at a temperature of 40 ºC and under a relative humidity (RH) of 95%.

The models consider as input 1 kg of water, while the rest of mix components are scaled accordingly following the data in Table 2.1. The oxide composition of the CEM I 42.5 MH/SR/LA produced by CEMENTA AB (Anläggningscement) considered in the calculations is from SKB (2014). For silica fume (SF), the used composition was measured by University of Surrey within CEBAMA; while that of Blast Furnace Slag (BFS) by VTT. Oxide compositions are summarized in Table 2.2.

Table 2.1. *Composition of low-pH cement paste mix used in experiments by USFD.*

Component	Amount ($g/100g_{solid}$)	Density (kg/m^3)	Volume fraction (-)	Surface area (m^2/g)
CEM I 42.5	37.5	3100	0.18	310
Silica fume	39.3	2300	0.25	26.09
Blast furnace slag	23.2	2900	0.12	0.40
Quartz filler	0	2650	0	-
Superplasticizer	6.0	1200	0.07	-
Water	25	1000	0.37	-
Total	131.0		1.00	1.00

Table 2.2. *Oxide composition of mix components used in the model.*

Oxide	CEM I (wt. %)	SF (wt. %)	BFS (wt. %)
CaO	64	1.46	41.5
SiO_2	21	93.1	32.8
Al_2O_3	3.5	1.44	10.6
SO_3	2.2	0.47	1.4
MgO	0.7	0.88	8.29
Fe_2O_3	4.6	0.91	0.81
K_2O	0.62	1.73	0.62
Na_2O	0.07	-	0.62
CO_2	2.2	-	-

The leaching experiments started immediately after the curing period. The ends of the cylinders were sealed with epoxy resin to allow only radial diffusion. Three different synthetic groundwaters were experimentally studied: granitic, saline and clayey (Table 2.3). Static dissolution experiments consider 60 ml vessels with 50 ml of each of the 3 types of groundwater. The experimental setup is placed in an oven at 40 ºC. The ends of the cylinders were sealed with epoxy to allow only radial diffusion. Samples were placed on a Teflon basket and duplicates of the samples are also tested along with duplicate blanks (with no cement sample). Replacement of the groundwater and sampling were planned to take place every 2 months over a period of 1 to 1.5 years.

Table 2.3. *Groundwater compositions used in leaching experiments: granitic and saline compositions from Gascoyne et al. (2002); clay composition from Vinsot et al. (2008).*

Concentrations	Granitic	Saline	Clayey
Na (mmol/L)	2.8	140	55
K (mmol/L)	0.1	2.1	1.1
Ca (mmol/L)	0.5	19.9	7.5
Mg (mmol/L)	0.2	0.4	5.7
Cl (mmol/L)	2.1	172.7	52.5
HCO_3 (mmol/L)	2.0	2.0	-
SO_4 (mmol/L)	0.1	4.0	15
pH	8.2	7.7	7

Available experimental data from these tests can be found in Vasconcelos et al. (2018). The mineralogical composition of the hydrated cement paste after 28 days has been characterized by XRD, TGA-MS, and SEM with a phase profile composed principally of alite, belite, hydrotalcite, portlandite, monosulfoaluminate, and monocarboaluminate. Porosity has been characterized by MIP and the value of total porosity obtained is 19 %, with a threshold pore entry radius below 0.2 µm. Micro-CT images of the hydrated cement paste have also been obtained on smaller samples. However, such samples (2 mm diameter) present a significant fraction of air bubbles and a poorly

dispersion of silica fume. Therefore, these measurements may not be fully representative of the samples used in the leaching experiments.

2.3 MODELLING THE HYDRATION OF LOW-pH CEMENT PASTE

The cement hydration-leaching model is implemented in iCP (Nardi et al., 2014). A two-dimensional axisymmetric model of the upper half samples is used (considering the mid-plane symmetry) with a simulation time of 2 years. The cement hydration model is based on the approach proposed by Lothenbach et al. (2008). A set of kinetic reactions for the dissolution of the mix components is coupled to chemical equilibrium calculations of precipitation / dissolution of cement hydrates using the thermodynamic database Thermochimie version 9b0 (Giffaut et al., 2014). Secondary phases expected to form during interaction with groundwater are considered in equilibrium. The model solves moisture transport processes based on the formulation presented in Idiart et al. (2011) and relates water content with moisture content through water desorption isotherms. Diffusive solute transport is also considered, coupled to moisture transport. Figure 2.1 presents a schematic overview of the implemented scheme. The result of the model includes the solid phase composition, the porewater mass and composition, the total porosity, and its approximate distribution between gel and capillary porosity.

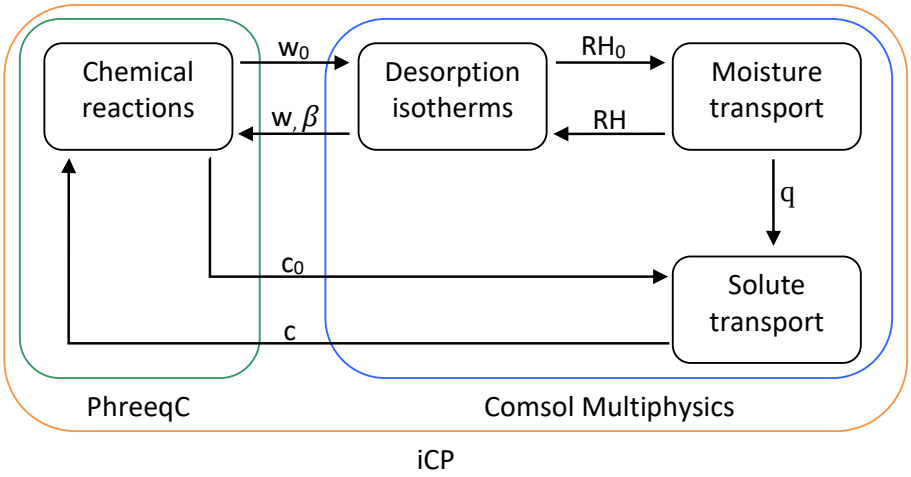

Figure 2.1: *Scheme of the implemented model. Variables with the subscript 0 represent values before the transport step.*

Traditionally, cement hydration has been modelled as a closed system using the exact amounts of the mix (Table 2.1) in a batch calculation. Leaching is then simulated in a separate model using the hydration results as input data. Therefore, two important effects are disregarded, (1) moisture transfer during the curing period and (2) groundwater interaction in late/delayed hydration (beyond the curing period). Moreover, the dependence of the dissolution rates on the availability of water has not been given enough attention. These are important simplifications, especially in the studied system, with a very low water/solid ratio (0.25) and a small sample size. In this case, water consumption during hydration (i.e. self-desiccation) is expected to be partly or even totally compensated by moisture transfer from the curing chamber. Due to the short curing period and considering the low water/solid ratio of the mix, hydration is expected to be on going during the leaching period. Thus, an open system computing moisture and solute transport must be considered to simulate hydration and leaching simultaneously.

The dissolution rates of the clinker phases (alite, belite, aluminate and ferrite) correspond to the empirical expressions proposed by Parrot and Killoh (1984). The (constant) dissolution rate of the blast furnace slag (BFS) is taken from Schöler et al. (2017), while that of silica fume corresponds to

the pH-dependent rate of quartz from Palandri and Kharaka (2004). Specific surface areas (Table 2.1) are either specified by the manufacturers or derived from particle size distribution data.

The rate of dissolution of each mix component is considered to be slowed down by a decrease in the internal RH of the sample to account for the effect of limited water content during hydration. The humidity-dependent factor proposed by Wyrzykowski and Lura (2016) is used here, applicable to low w/b mixes with high replacements of SF and BFS.

RH changes are related with water content using the sorption/desorption isotherms (Baroghel-Bouny, 2007). The desorption isotherm model proposed by Hedberg (1994) and presented in Norling (1994; 1997) is used here. The model was compared with the experimentally obtained data including low water/solid ratio cements with silica additions. In the current work, the model has been adapted to consider that the maximum water content is equal to total porosity (as obtained from the solid phase assemblage). Desorption isotherms for different degrees of hydration (α) are presented in Figure 2.2.

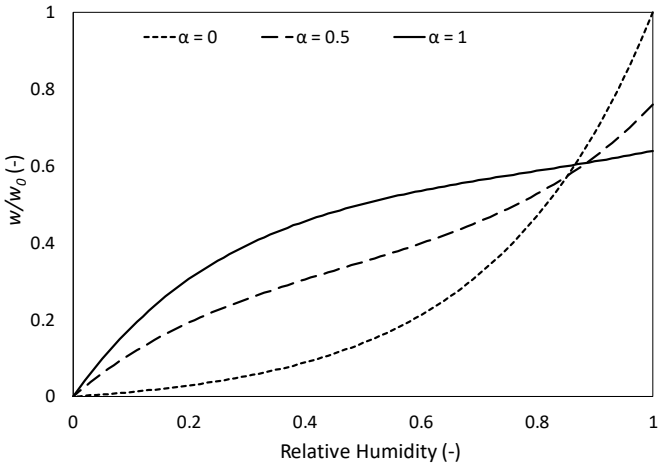

Figure 2.2. *Water desorption isotherms for different degrees of hydration, based on Norling (1997). Water maximum values are related to porosity.*

The evaporable water content is updated in the geochemical solver as a function of the consumption of water in the hydration process. Internal RH is then calculated dynamically using the desorption isotherms. Moisture diffusion is considered to account for interaction with the curing chamber during hydration (represented as RH boundary condition). For the leaching phase, as samples are immersed in groundwater, RH is fixed to 1 in the lateral contour. The diffusion coefficient for RH is strongly non-linear. In this work, this dependency is represented as shown in equation (2.1), adapted from Idiart et al. (2011), where D_0 and $D_1$are constants determining the value of the coefficient at RH=0 and RH=1, respectively, and $f(RH)$ is a hyperbolic function of RH.

$$D_{RH}(RH) = D_0 + (D_1 + D_0) \cdot f(RH) \tag{2.1}$$

The kinetic dissolution rates are updated with the humidity-dependent factor presented in equation (2.2). Furthermore, the updated mass of water after the moisture transport step is calculated with the desorption isotherms.

$$\beta_{RH} = min[1; 3.7 \cdot RH^{25}] \tag{2.2}$$

The simulation is performed at 40 ºC, correcting the kinetic rates of the clinker with activation energies from Lothenbach et al. (2008). The superplasticizer fraction is considered as chemically inert. The alkali (Na and K) and aluminium uptake in C-S-H phases is not considered in the simulations.

The secondary phases allowed to form during hydration and leaching are included in Table 2.4. In turn, different phases are included in each simulation depending on the groundwater in contact with the samples. Specific secondary minerals allowed to precipitate for granitic, saline and clayey conditions are also shown.

Table 2.4: *Secondary minerals allowed to precipitate/dissolve. Cement phases are included in all the simulations; granitic, saline and clayey minerals only in their corresponding cases.*

Cement phases		Granitic	Saline	Clayey
Portlandite	Hydrotalcite	Hnontronite - K	Friedel-salt	Illite – Al
$CSH_{1.6}$	Hydrotalcite - CO3	Hnontronite - Mg	Albite-low	Illite – FeII
$CSH_{1.2}$	Monocarboaluminate	Saponite - FeCa	Clinoptilolite - Na	Illite - FeIII
$CSH_{0.8}$	Hemicarboaluminate	Saponite - FeK	HBeidellite - Na	Illite – Mg
C_3AH_6	Stratlingite	Saponite - FeMg	Hnontronite - Na	Clinoptilolite - Ca
C_3FH_6	Brucite	Saponite - FeNa	Nontronite - Na	Clinoptilolite - K
C_4AH_{13}	Ettringite	Syngenite		Clinoptilolite - Na
C_4FH_{13}	Ettringite - Fe			Phillipsite - Ca
Calcite	Gypsum			Phillipsite - K
CaO (cr)	Monosulfoaluminate			Phillipsite - Na
Thernardite	Monosulfate - Fe			
Arcanite	Ferrihydrite (am)			

2.4 RESULTS

Model results of the hydration during the first 28 days are equivalent for the three simulation cases (same curing conditions). Once samples are contacted with different groundwaters, cement pastes present differences in mineralogical composition and porosity values.

Results from the three models are comparatively shown to illustrate the implications of considering groundwater interaction at early ages. Results are depicted as time evolution of the centre-point of the cylindrical samples as well as 3D plots (obtained by revolution of the axisymmetric 2D geometry). Firstly, the results are presented in terms of mineral volume fraction. The dissolution of the clinker and binder components as a function of time are shown in Figure 2.3. Results for the centre-point of three samples are superposed. Models show the same results during the first 28 days. Alite dissolves relatively fast (after 10 days of hydration almost 70% is dissolved), while dissolution of belite, aluminate, and ferrite occurs much more slowly. From that time onwards, dissolution of BFS and SF increases.

Differences between the 3 studied systems can be observed after interaction with groundwater. After 300 days, pH evolves differently because of specific secondary minerals precipitation. When in contact with clayey water, pH remains at a value close to 11 and SF continues dissolving at the same rate. For the granitic water, pH reaches a plateau at 10.4 resulting in a decrease in SF dissolution rate. For the sample in contact with saline water, pH values drop down to10.2 and SF stops dissolving (quartz dissolution is highly dependent on pH).

The evolution of the mineralogical phase assemblage is shown in Figure 2.4, Figure 2.5 and Figure 2.6. Portlandite, ettringite and C-S-H with C/S ratio of 1.6 rapidly form. As hydration proceeds and more Si is released from dissolution of the binder, portlandite consumes to give rise to C-S-H phases of lower C/S ratio until reaching a composition with C/S ratio of 0.8 (Table 2.5). In all cases, strätlingite forms once portlandite is depleted together with ferrihydrite.

Interaction with granitic groundwater (Figure 2.4) leads to ferrihydrite and strätlingite dissolution in favour of K and Mg nontronites precipitation. After 730 days of interaction with saline water (see

Figure 2.5), mineral phases in the system remain unaltered, except for the precipitation of a small amount of sodium beidellite (Table 2.5). For clayey groundwater interaction, the model predicts SF and strätlingite dissolution together with the formation of K and Ca phillipsites (Figure 2.6).

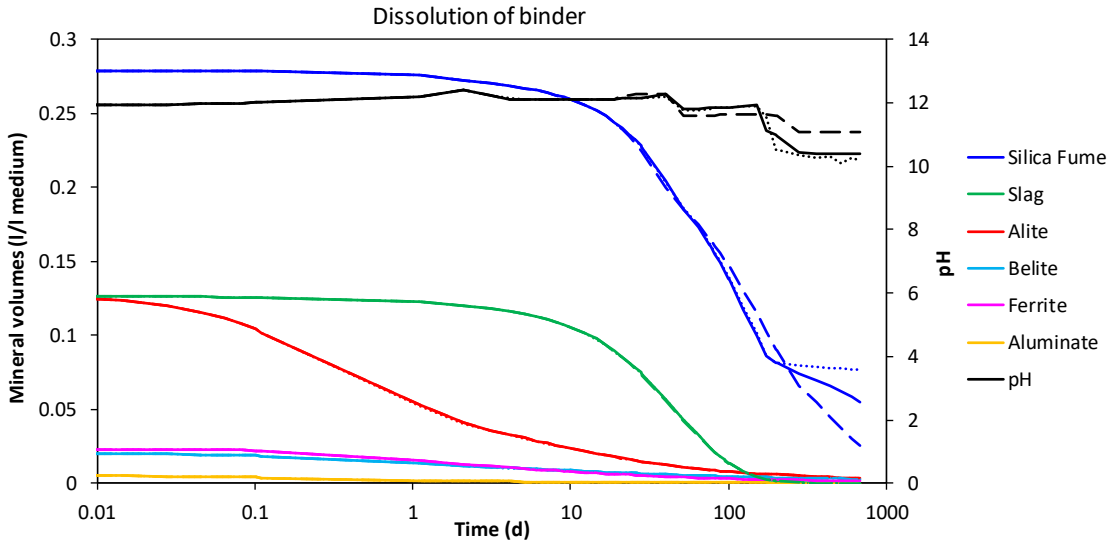

Figure 2.3: *Dissolution of the binder: evolution of unhydrated mineral volumes (liter/liter of medium) and pH as a function of hydration time (days) for granitic (solid lines), saline (dotted lines) and clayey (dashed lines) interaction models.*

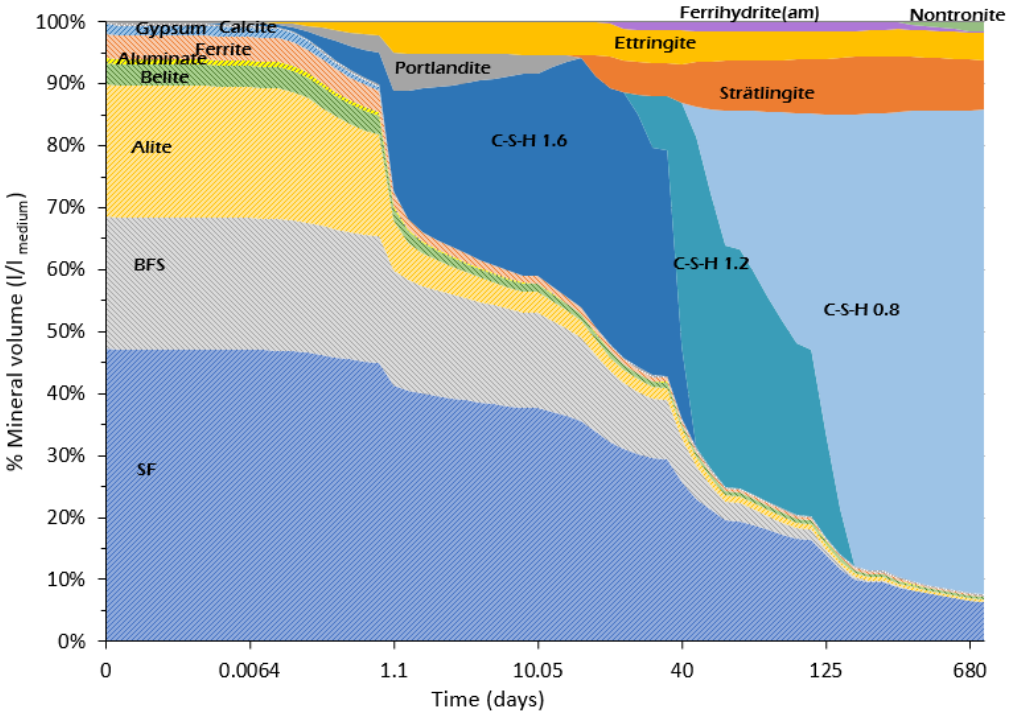

Figure 2.4: *Mineralogical composition evolution (volume fraction) as a function of hydration time (days) for granitic interaction model.*

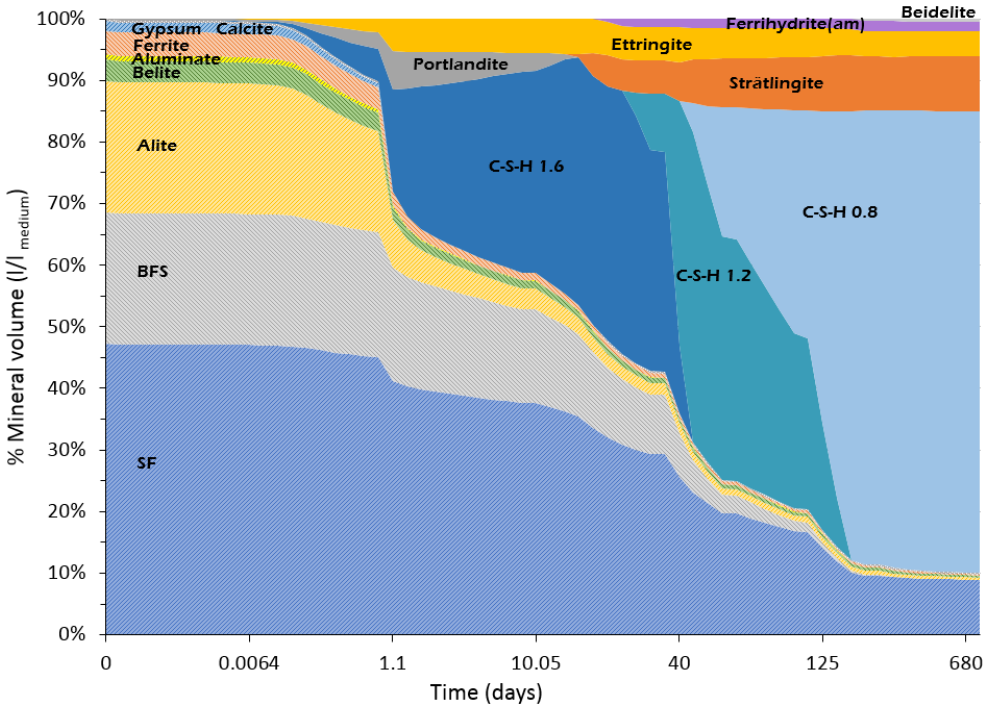

Figure 2.5: *Mineralogical composition evolution (volume fraction) as a function of hydration time (days) for saline interaction model.*

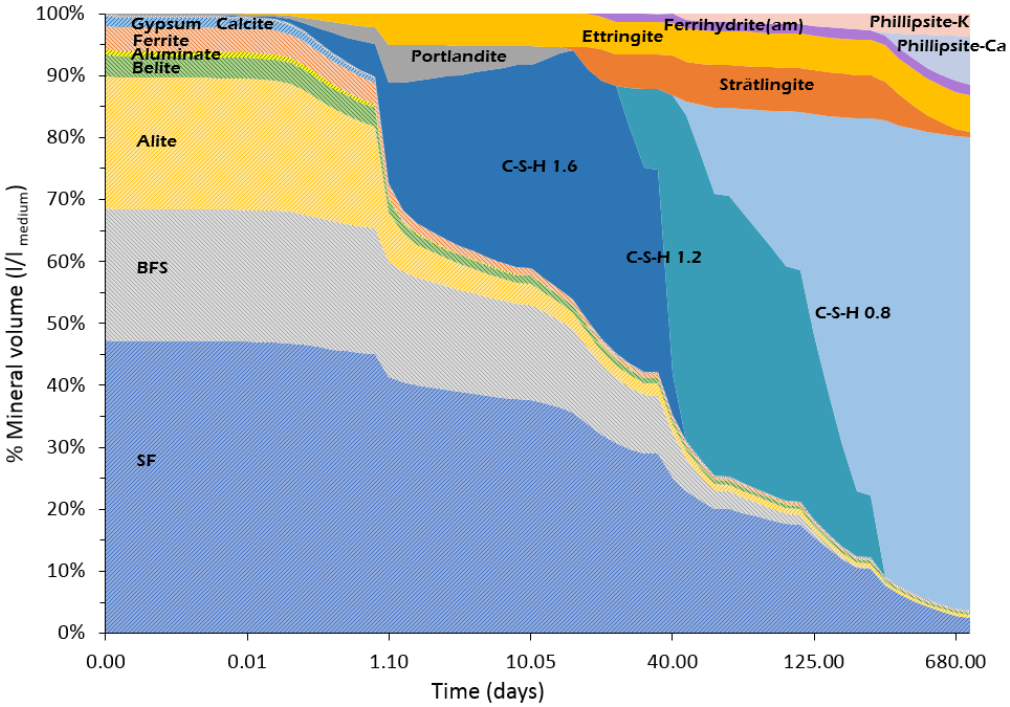

Figure 2.6: *Mineralogical composition evolution (volume fraction) as a function of hydration time (days) for clayey interaction model.*

The evolution of the pH is presented in Figure 2.3, showing a maximum value of 12.5 after ~2.1 days and then gradually decreasing upon portlandite dissolution. pH further decreases to a value of ~11.6 at 52 days due to C-S-H decalcification from C/S phases of ratio 1.6 to 0.8 (Figure 2.4). After ~1 year, a second plateau is reached, pH values are then different for the three models as a result of different secondary phases precipitation.

The mineralogical phase assemblage and porewater composition after 28, 365 and 730 days of hydration is shown in Tables 2.5 and 2.6. Results after 28 days are only presented once, as they are equivalent for the three simulations. It may be observed that portlandite formed at early ages has completely dissolved after 28 days. The results also illustrate how the cement hydration is still significantly evolving between 1 month and 2 years of interaction with groundwaters, mainly because an immersed open system is assumed. The main differences between the three studied models are again appreciable in the formation of specific secondary minerals after 2 years. As a consequence: hydration phases, SF content, pH values, water content and pore water composition differ from one sample to the other.

Table 2.5. *Model results of the mineralogical phase assemblage after 28 days 1 year and 2 years for the 3 models, to be noticed that result for 28 days are equal.*

Age (days)	**28**	**365** Granitic	**365** Saline	**365** Clayey	**730** Granitic	**730** Saline	**730** Clayey
Mineral	**Concentration (mol/l$_{medium}$)**						
Portlandite	0	0	0	0	0	0	0
C-S-H 1.6	3.348	0	0	0	0	0	0
C-S-H 1.2	0.893	0	0	0	0	0	0
C-S-H 0.8	0	10.742	10.740	10.873	10.936	10.842	11.200
Ettringite	0.057	0.051	0.049	0.071	0.052	0.048	0.073
Calcite	0.055	0.055	0.055	0.055	0.055	0.055	0.055
Hydrotalcite	0.108	0.245	0.245	0.248	0.244	0.245	0.252
Strätlingite	0.196	0.342	0.348	0.199	0.309	0.352	0.039
Ferrihydrite (am)	0.296	0.222	0.412	0.418	0.025	0.419	0.433
Alite	0.202	0.061	0.061	0.061	0.045	0.045	0.045
Aluminate	0.006	0.002	0.002	0.002	0.001	0.001	0.001
Belite	0.126	0.063	0.063	0.063	0.053	0.053	0.053
Ferrite	0.041	0.015	0.015	0.015	0.012	0.012	0.012
Silica Fume	8.129	2.487	2.804	1.941	1.895	2.723	0.790
Blast Furnace Slag	1.658	6.6E-4	7.1E-4	6.5E-4	1.0E-7	1.3E-7	1.0E-7
Nontronite - K	-	0.090	-	-	0.136	-	-
Nontronite - Mg	-	0.025	-	-	0.104	-	-
Beidelite - Na	-	-	2.7E-2	-	-	0.027	-
Phillipsite - Ca	-	-	-	0.139	-	-	0.447
Phillipsite - K	-	-	-	0.184	-	-	0.213
Phillipsite - Na	-	-	-	0.003	-	-	0.003

Table 2.6. *Model results of porewater composition after 28 days, 1 year and 2 years for the 3 models, to be noticed that result for 28 days are equal.*

Age (days)	**28**	**365**	**365**	**365**	**730**	**730**	**730**
Water		Granitic	Saline	Clayey	Granitic	Saline	Clayey
pH	12.16	10.41	10.27	11.08	10.38	10.18	11.08
Water (g)	0.192	0.093	0.089	0.076	0.097	0.087	0.072
Totals	**Concentration (M)**						
Al	2.92E-04	9.52E-05	1.65E-04	1.16E-04	8.83E-05	1.14E-04	1.16E-04
Ca	3.24E-05	8.40E-06	1.27E-05	1.05E-05	7.99E-06	9.25E-06	1.05E-05
Fe	1.18E-03	8.41E-03	1.05E-02	3.02E-03	9.11E-03	1.17E-02	3.02E-03
C	1.06E-10	1.04E-10	1.07E-10	1.11E-10	1.01E-10	1.02E-10	1.06E-10
Cl	2.08E-06	3.53E-08	1.25E-07	1.59E-07	3.28E-08	8.98E-08	1.59E-07
K	3.98E-02	7.76E-05	9.81E-02	4.55E-04	8.22E-05	2.38E-02	4.55E-04
Mg	1.95E-09	2.60E-07	7.05E-07	2.58E-08	2.82E-07	7.16E-07	2.58E-08
Na	1.77E-02	4.04E-03	1.73E-20	8.19E-03	2.43E-04	1.44E-19	8.19E-03
S	2.43E-03	9.53E-03	5.81E-02	4.86E-03	8.40E-03	2.26E-02	4.86E-03
Si	2.35E-04	9.09E-04	2.03E-03	6.45E-04	8.54E-04	1.43E-03	6.45E-04

The total porosity (ϕ_{tot}) can be calculated from the hydration simulation using equation (2.3) if autogenous shrinkage is not considered. In this equation, V stands for volumes (litre), ϕ for volume fractions (litre/litre medium) and M_v for molar volumes (litre/mol). And subscripts cem, water, hydrates, aggr, sp and inert stand for unhydrated binder, water, cement hydrates, aggregates (zero in this case), superplasticizer (considered inert), and any chemically inert fraction.

$$\phi_{tot} = \frac{V_{cem,0}+V_{water,0}-V_{cem,t}-V_{hydrates,t}}{V_{cem,0}+V_{water,0}+V_{aggr}+V_{sp}} \quad (2.3)$$

Total porosity evolution is shown in Figure 2.7 together with the evolution of the volume fraction of evaporable water (ϕ_w). When the latter is smaller than the total porosity, unsaturated conditions prevail, and moisture diffuses into the sample from the curing chamber or the water reservoir.

Total porosity value after 28 days of hydration is 0.20, which agrees relatively well with the value measured experimentally (0.19). The difference could be related to the defined moisture diffusion coefficient at early ages. Underestimating the effect of moisture transfer from the curing chamber can lead to a lower volume of cement hydrates and thus a higher porosity. After 2 years of groundwater interaction, porosity values are 0.10, 0.09 and 0.07 for the granitic, saline and clayey simulations, respectively. At this point, volume fraction of the specific secondary minerals precipitating in each interaction model makes the difference. The difference between total porosity and evaporable water content at 28 days is 0.01, reaching a maximum value of 0.046 after 5 days of hydration. Once the samples are immersed in groundwater (28 days), saturation occurs in only 2 days (at 30 days).

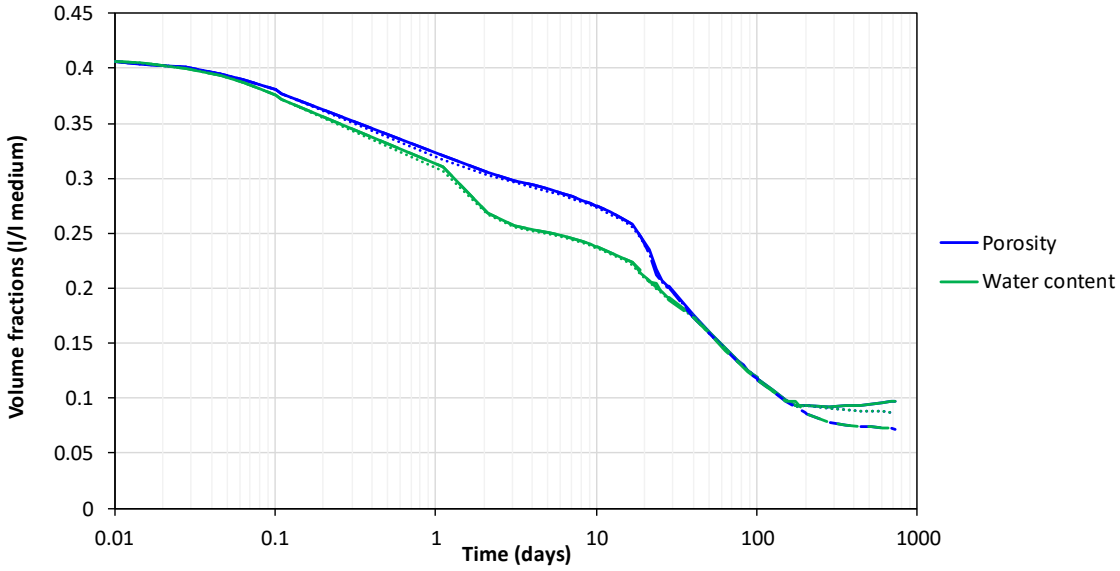

Figure 2.7: *Evolution of evaporable water content and total porosity as a function of hydration time (days) for granitic (solid lines), saline (dotted lines) and clayey (dashed lines) interaction models.*

The internal RH can be significantly reduced during hydration, reaching values down to 0.94 from 1 to 28 days (Figure 2.8). Consequently, β_{RH} (equation 2.2) decreases to a minimum of 0.67 after 4 days, resulting in a decrease of the dissolution rates. After 28 days, the sample is immersed in groundwater, leading to a rapid saturation and a value of β_{RH} of 1 (40 days).

Evolution of the degree of hydration, α, follows the shape of a sigmoid function (in a logarithmic time-scale), and after 1 year the degree of hydration approaches 0.95.

The effect of interaction with groundwater is clearly shown by the spatial distribution of key variables. Figure 2.9 presents the distribution at 2.8 days (when water uptake from the curing chamber is more noticeable) of several variables. RH values show a reduction in the inner region of the sample due to self-desiccation, values in the contour remain at 0.95 (curing chamber conditions). The larger availability of water results in a more advanced degree of hydration (α) in the boundaries. pH, binder minerals (alite) and hydration phases (portlandite and ettringite) show variations when comparing the centre of the sample and the contours due to the curing conditions.

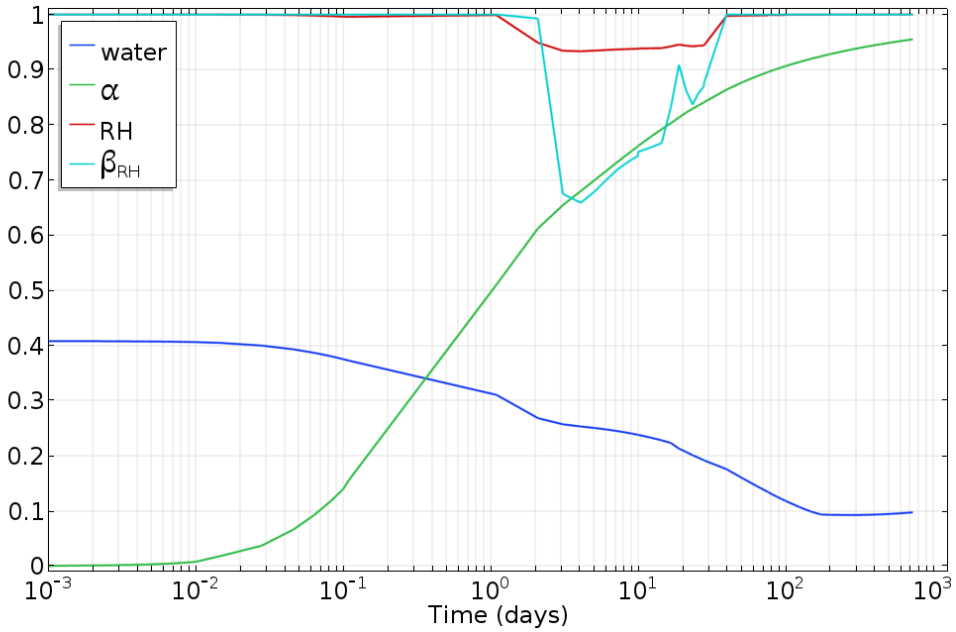

Figure 2.8: *Evolution of water content, hydration degree (α), internal RH and the factor (β_{RH}) for the centre-point of the sample interacting with clayey groundwater.*

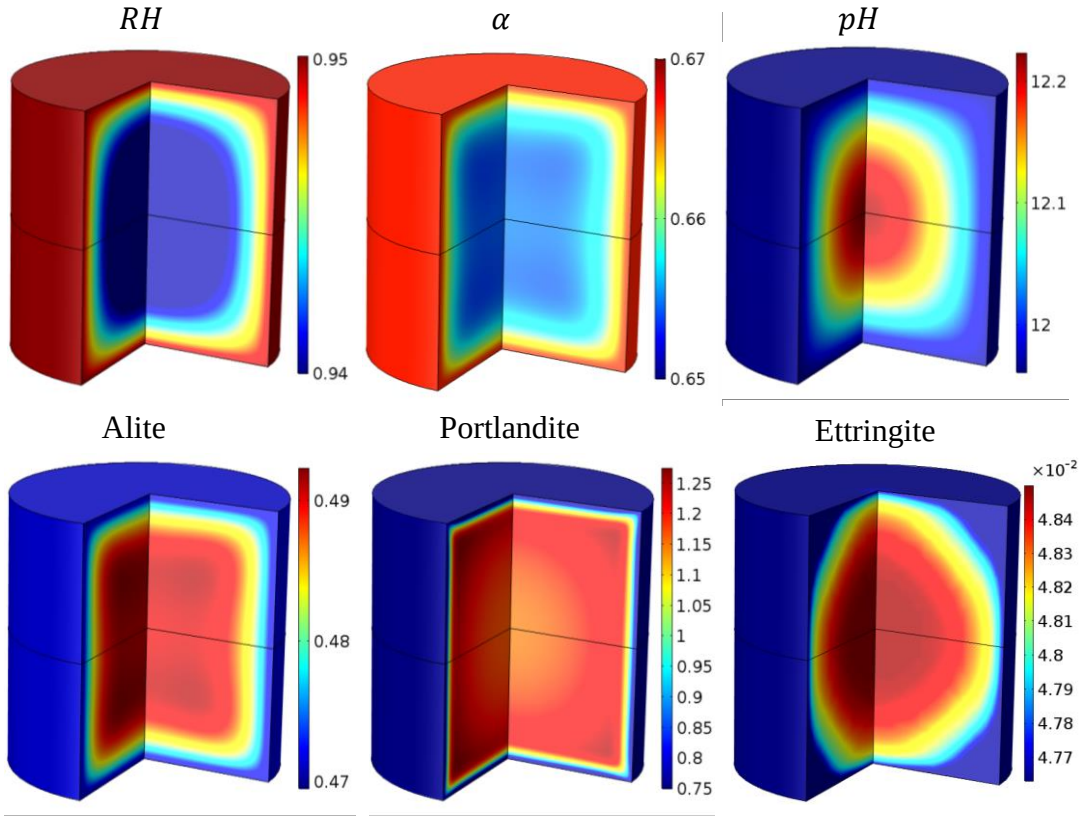

Figure 2.9: *Spatial distribution of RH (-), α, pH and cement phases (mol/ l medium) after 2.8 days of hydration in the curing chamber.*

2.5 CONCLUSIONS

The leaching experiments of the low-pH cement paste samples by USFD were modelled using a coupled hydration-degradation model. The cement hydration model includes thermodynamic calculations coupled to a set of kinetic equations for the dissolution of the cement mix components. Degradation is modelled using traditional reactive transport models. Given the mix design of the reference CEBAMA cement paste, it is expected that hydration will continue to a significant degree for a much longer period than 28 days, which has been considered as curing time in USFD experiments. As a result, modelling of the leaching experiments require to simultaneously consider hydration and reactive transport in the simulations. In addition, due to the low water-to-solid ratio and the small dimensions of the samples, it is expected that during the curing period, moisture transfer from the exterior can play a non-negligible role in maintaining an internal relative humidity close to saturation. Thus, moisture transport inside the samples has also been considered. The model developed in the present work couples the three processes (i.e., hydration, reactive transport, and moisture transport). The results show the impact of long-term hydration and the differences between the leaching experiments using diverse groundwater compositions. Further comparison to experimental data will be attempted once these become available.

Acknowledgements

The research leading to these results has received funding from the European Union's Horizon 2020 Research and Training Programme of the European Atomic Energy Community (EURATOM) (H2020-NFRP-2014/2015) under grant agreement n° 662147 (CEBAMA).

2.6 REFERENCES

Baroghel-Bouny, V. (2007). Water vapour sorption experiments on hardened cementitious materials. Part I: Essential tool for analysis of hygral behaviour and its relation to pore structure. Cem. Conc. Res., 37, 414–437.

Giffaut E., Grivé M., Blanc P., Vieillard P., Colàs E., Gailhanou H., Gaboreau S., Marty N., Madé B., Duro L. (2014). Andra thermodynamic database for performance assessment: ThermoChimie. Applied Geochemistry, 49, 225-236.

Hedberg, B. (1994). Application for Excel of the Model of self-desiccation in cement paste, computer software. Department of Building Materials, Chalmers U. of Tech., Sweden.

Idiart A., López C.M., Carol I. (2011). Modeling of drying shrinkage of concrete specimens at the meso-level. Materials and Structures, 44(2), 415–435.

Lothenbach B., Le Saout G., Gallucci E., Scrivener K. (2008). Influence of limestone on the hydration of Portland cements. Cem. Conc. Res., 38, 848-860.

Nardi A., Idiart A., Trinchero P., de Vries L.M., Molinero J. (2014). Interface COMSOL-PHREEQC (iCP), an efficient numerical framework for the solution of coupled multiphysics and geochemistry. Computers and Geosciences, 69, 10-21.

Norling Mjörnell, K. (1994). Self-desiccation in concrete. Licenciate-thesis, Department of Building Materials, Chalmers U. of Tech., Sweden.

Norling Mjörnell, K. (1997). Moisture conditions in high performance concrete: mathematical modelling and measurements. Doctor-thesis, Department of Building Materials, Chalmers U. of Tech., Sweden.

Palandri J.L., Kharaka Y.K. (2004). A compilation of rate parameters of water-mineral interactions kinetics for application to geochemical modeling. USGS-Report (2004-1068), Menlo Park, California, USA.

Parrot L.J., Killoh D.C. (1984). Prediction of cement hydration, Br. Cer. Proc. 35, 41-53.

Schöler A., Winnefeld F., Ben Haha M., Lothenbach B. (2017). The effect of glass composition on the reactivity of synthetic glasses. J. Am. Cer. Soc. 100, 2553–2567.

SKB (2014). Initial state report for the safety assessment SR-PSU. Report SKB TR-14-02.

Vasconcelos R. G. W., Idiart A. Hyatt N. C., Provis J. L., Corkhill C. L. (2017). Preliminary assessment of interaction between UK backfill cement material and groundwater. In Proc. 2nd Annual Workshop CEBAMA, Helsinki, Finland, May 2017.

Vasconcelos, R., Walkley, B., Hyatt, N., Provis, J., Corkhill, C. (2018). The physico-chemical evolution of a low-pH cement in contact with groundwater. In Proc. 3rd Annual Workshop CEBAMA project, Nantes (France), April 2018.

Vehmas T., Schnidler A., Löija M., Leivo M., Holt E. (2016). Reference mix design and castings for low-pH concrete for nuclear waste repositories. In Proc. 1st Annual Workshop CEBAMA, Barcelona, Spain, May 2016.

Wyrzykowski, M., Lura, P. (2016). Effect of relative humidity decrease due to self-desiccation on the hydration kinetics of cement. Cem. Conc. Res. 85, 75–81.

3 BRGM/ P. Leroy, S. Gaboreau, F. Claret (BRGM), A. Hördt, H Stebner (Braunschweig Univ., Germany), E. Zimmermann, J. A. Huisman (Forschungszentrum Jülich), M. Bücker (Tech. Univ. Wien)

Abstract

Concrete is the mostly used material for civil and industrial infrastructures. In the context of a geological disposal of nuclear waste, concrete performance might be degraded when in contact with the host formation. The ability to monitor the changes of the concrete properties using the spectral induced polarization (SIP) method is therefore of great interest. In our study, SIP laboratory measurements in the 100 mHz to 45 kHz frequency range were carried out on low-pH cement and concrete. Materials exhibit very high resistivities (mostly above 10 kΩ m) and phase shifts between measured voltage and injected sinusoidal current. Complex resistivity measurements were interpreted using membrane and Maxwell-Wagner polarization models that depend on the electrochemical and microstructural properties of cementitious materials. Relevant information on the mean pore size, pore size distribution, and connected porosity was obtained from SIP, opening up the possibility of using our approach to monitor concrete stability in-situ.

3.1 INTRODUCTION

The modelling work presented here briefly is in the process of being published in a paper entitled "Spectral induced polarization of low-pH cement and concrete", under submission to the journal Cement and Concrete Composites. In-situ monitoring methods that are fast, non-destructive, and can scan large material volumes are needed to control concrete stability. In the last two decades, the spectral induced polarization (SIP) method has gained popularity in hydro-geophysics to monitor hydraulic properties and biogeochemical changes of soils and rocks for environmental purposes. SIP is an impedance spectroscopy (IS) technique where the complex resistivity of the medium is measured with a four-electrode set-up: two electrodes to inject a sinusoidal current in the mHz to kHz frequency range and two electrodes to measure the resulting voltage in the medium. Resistivity magnitude and phase shift between measured voltage and injected sinusoidal current are very sensitive to conduction and polarization currents occurring in the bulk aqueous electrolyte and on the wetted surfaces of the pores, hence to the microstructure of the material. Compared to impedance spectroscopy with a two-electrode set-up, separation of potential from current electrodes in SIP reduces polarization of potential electrodes, which improves measurement accuracy for frequencies below 1 kHz.

To the best of our knowledge, there are no impedance spectroscopy measurements on low-pH cement and concrete interpreted by a membrane polarization model. In our study, the ZEL SIP system developed by Zimmerman et al. (2008) was used to measure the impedance of these materials in the low-frequency range (100 mHz-45 kHz) with a phase shift accuracy of 1 mrad for frequencies below 1 kHz. Our SIP measurements were interpreted using the extended membrane polarization models of Bairlein et al. (2016) and Stebner et al. (2017) to consider Maxwell-Wagner polarization and the interlayer spaces of C-S-H.

The details of the work carried out within WP3 are described in the paper submitted to Cement and Concrete Composites (Leroy et al., 2019).

3.2 DESCRIPTION OF THE MODELLING WORK

The modelling work is presented in the paper entitled "Spectral induced polarization of low-pH cement and concrete" under submission for Cement and Concrete Composites. Basically, it used the

analytical solution of the Poisson-Nernst-Planck equations for describing ion electromigration and diffusion in electrostatically charged wide and narrow bi-tubes when concrete is submitted to a weak low-frequency electrical field (Bücker, 2017, Figure 3.1). Pore network models are used for the upscaling to laboratory measurements. Input parameters are the chemical composition of the pore water and the zeta potential. Outputs are the geometrical properties including the porosity and the pore size distribution.

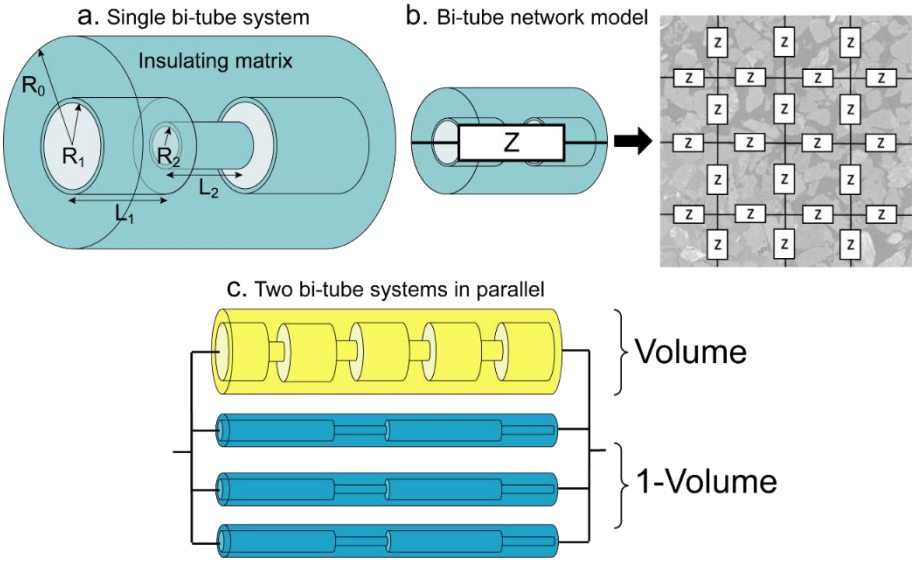

Figure 3.1. *Impedance models to interpret HCP and concrete SIP spectra.*

3.3 MAIN OUTCOMES

We have carried out complex impedance measurements on low-pH cement paste and concrete in the low-frequency range (100 mHz-45 kHz) using a four-electrode set-up for spectral induced polarization (SIP) measurements (Figure 3.2). Resistivity magnitude and phase shift spectra between measured voltage and injected current have been obtained for these materials. We have also developed combined membrane and Maxwell-Wagner polarization models based on the models of Bairlein et al. (2016), Stebner et al. (2017), and Bücker (2017) to describe these measurements. These models consider the electrochemical and microstructural properties, namely, the zeta potential and the pore size, length, and the connected porosity of cement-based materials.

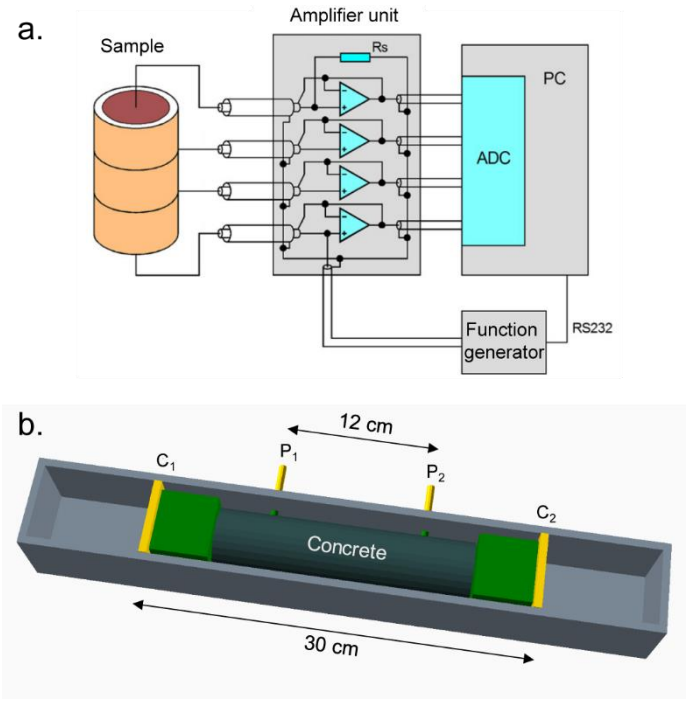

Figure 3.2. *a. Sketch of the ZEL-SIP-04 system (modified, from Zimmermann et al., 2008). b. Sketch of the sample holder for SIP measurements on concrete (the synthetic wet sponges to establish contact between the current (C_1, C_2) and potential (P_1, P_2) electrodes and the sample are the green materials).*

The measured resistivity magnitude and phase shift spectra are very high (Figure 3.3). The resistivity magnitude is mostly above 10 kΩ m and the phase shift magnitude ranges from ~40 mrad at 100 mHz to ~625 mrad at 10 kHz. These observations were respectively attributed to (1) the presence of the insulating interlayer spaces in calcium-silicate-hydrate (C-S-H) particles, (2) membrane polarization between the negatively surface charged micropores with high ion selectivity (calcium cation adsorption and sulphate anion repulsion) and the meso- and macropores with low ion selectivity, and (3) Maxwell-Wagner polarization between the solid and liquid phases. Our resistivity models were able to match the SIP measurements by considering pore sizes in relative agreement with and smaller than the values determined by mercury intrusion porosimetry (MIP) (Figure 3.4). However, MIP only probes pore radii above 3.5 nm and 25-30% of the sample porosity. Therefore, in reality, pore radii may be smaller than those inferred from MIP and thus closer to the values inferred from our computations. It was also necessary to include in our models, pores representing C-S-H interlayer spaces to match the SIP measurements with connected porosities corresponding to the measured porosity values (Table 3.1).

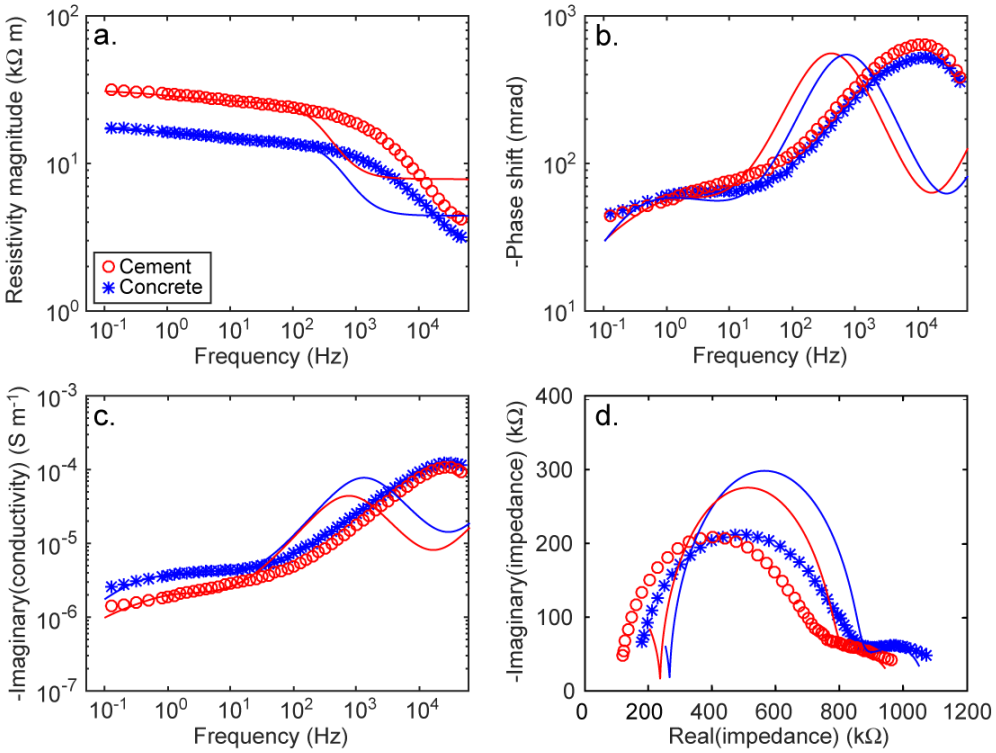

Figure 3.3. *Measured HCP and concrete SIP spectra (symbols) and simulation results using network bi-tube models (red line for HCP and blue line for concrete).*

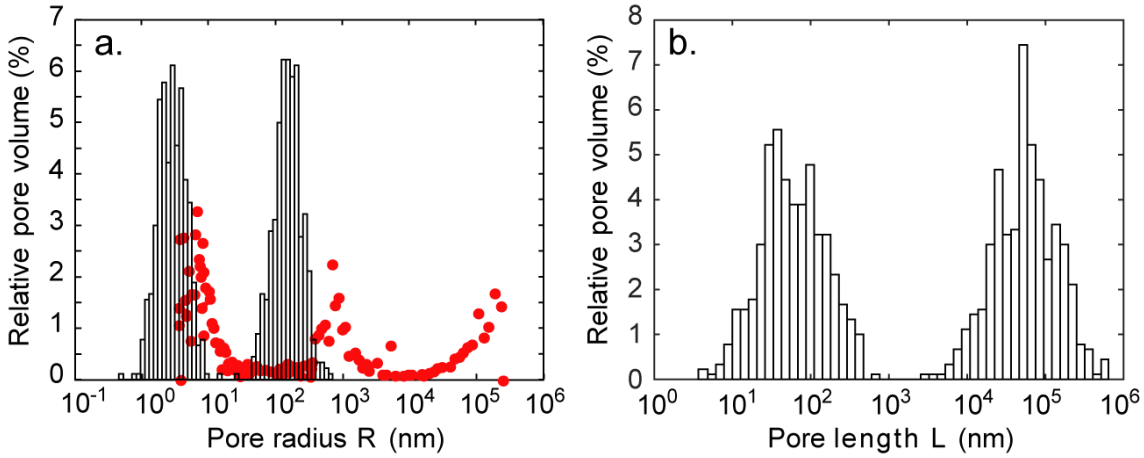

Figure 3.4. *a. Pore radius distribution and b. pore length distribution used in the network model to match the SIP measurements on HCP. Filled red circles are the pore radii measurements from MIP. The distributions used in the network model to match the SIP measurements on concrete look similar and are not shown for brevity.*

Table 3.1. *Measured densities (g cm^{-3}) and estimated porosities (%) of the two materials.*

	Dry density ρ		Grain density ρ_g	Porosity ϕ		
Methods	MIP	KP	HP	MIP	KP	Calculated[a]
HCP	1.878	1.830	2.48	6.07	26.21	24.3
Concrete	2.275	2.284	2.61	3.8	12.47	12.8

[a] According to density measurements.

3.4 CONCLUSIONS AND PERSPECTIVES

The present study shows that the pore structure and connected porosity of cementitious materials can be inferred from SIP. Our approach can therefore be used to monitor concrete stability in-situ. This is particularly interesting in the light of recent developments in spectral electrical impedance tomography using borehole and surface electrodes to obtain the complex electrical resistivity distribution in the mHz to kHz frequency range (Zhao et al., 2013; Zhao et al., 2015). Such distribution could be inverted to obtain the spatial and temporal dynamics of the pore structure, connected porosity, and permeability. In the future, it would be very interesting to numerically solve the Poisson-Nernst-Planck equations to improve the accuracy of the resistivity models and consider polarization of steel reinforcement in concrete structures.

Acknowledgements

The research leading to these results has received funding from the European Union's Horizon 2020 Research and Training Programme of the European Atomic Energy Community (EURATOM) (H2020-NFRP-2014/2015) under grant agreement n° 662147 (CEBAMA).

3.5 REFERENCES

Bairlein, K. et al. (2016). Temperature dependence of spectral induced polarization data: experimental results and membrane polarization theory. Geophys. J. Int., 205, 1, 440–453.

Stebner, H et al. (2017). Simulation of membrane polarization of porous media with impedance networks. Near Surf. Geophys., 15, 563–578.

Bücker, M. (2017). Pore-scale modelling of induced-polarization mechanisms in geologic materials. PhD thesis, Department of Geophysics, University of Bonn, Bonn, Germany.

Leroy, P., Hördt, A., Gaboreau, S., Zimmermann, E., Claret, F., Bücker, M., Stebner, H., Huisman, J. A. (2019). Spectral induced polarization of low-pH cement and concrete. Submitted to Cement and Concrete Composites.

Zhao, Y. et al. (2013). Broadband EIT borehole measurements with high phase accuracy using numerical corrections of electromagnetic coupling effects. Meas. Sci. Technol., 24, 8.

Zhao, Y. et al. (2015). Phase correction of electromagnetic coupling effects in cross-borehole EIT measurements. Meas. Sci. Technol., 26, 1.

Zimmermann, E. et al. (2008). A high-accuracy impedance spectrometer for measuring sediments with low polarizability. Meas. Sci. Technol., 19, 10.

7 JUELICH/ S. Rohmen, G. Deissmann, D. Bosbach (JUELICH), A. Idiart (AMPHOS 21)

Abstract

In cementitious materials, chemical and microstructural heterogeneities exist on a wide range of length scales, from the nano- to the macro-scale. Pore-scale models represent an appealing approach to include a more accurate and mechanistic description of physical and chemical processes occurring in such materials. In the framework of CEBAMA, a reactive transport simulator based on the Lattice-Boltzmann-Method (iPP) was developed. This simulator allows determination of effective diffusion coefficients and simulating physico-chemical alteration processes of cement-based materials at the micro-scale. Here we describe the latest developments implemented and the application on microstructures derived from µXCT measurements of hardened low-pH cement paste. This microstructural data was combined with information on the phase assemblage from a simulation of cement hydration and used as input for iPP. Subsequently, the effective diffusion coefficient for the material was derived and a leaching experiment was simulated.

7.1 INTRODUCTION

It is known that microscopic heterogeneities may have significant effects on macroscopic transport properties such as permeability and effective diffusion coefficients. Pore-scale reactive transport models can be used to mechanistically describe the microscopic evolution of the pore structure and the heterogeneous distribution of hydrated phases and unhydrated binder components in cementitious materials. This approach can be used to address chemical degradation processes due to calcium leaching or carbonation of cementitious materials and their impact on physical and transport properties, such as porosity, pore-size distribution, permeability or diffusivity (e.g. Taylor, 1997).

In the frame of the CEBAMA project, a coupled code named *iPP* (interface Palabos PhreeqC) was developed. *iPP* is able to calculate reactive transport processes in porous media on the pore scale using the Lattice-Boltzmann method (Palabos; Flowkit, 2011) and utilizing a geochemical solver based on the law of mass action (PhreeqcRM; Parkhurst and Wissmeier, 2015). iPP exploits MPI parallelization and C++ template meta-programming techniques allowing usage of high-performance computing (HPC) facilities and optimizations by modern compiler features (Rohmen et al., 2018). For improving scalability, in terms of parallel computational performance, optimizations in the PhreeqcRM code were implemented in order to allow fully coupled reactive transport simulations of larger models. The Lattice-Boltzmann schemes used for diffusive solute transport are D2Q5 in 2D and D3Q7 in 3D (Mohamad, 2011, Succi, 2001).

For benchmarking and validation of *iPP*, leaching experiments performed at the University of Sheffield (USFD) within CEBAMA WP1 were used (Vasconcelos et al., 2018). In this paper, we outline the latest development status of *iPP*, its application to determine effective diffusion coefficients of hardened cement pastes, and the results of simulations addressing the leaching of the CEBAMA low-pH reference cement paste when exposed to different groundwaters, using input geometries derived from microstructural analysis.

7.2 EXPERIMENTS PERFORMED AT USFD

Within CEBAMA WP1, USFD is conducting experiments which are dedicated to quantifying compositional and microstructural changes in low-pH cement pastes due to leaching with different types of groundwaters (Vasconcelos et al., 2018). The mixture of the cement paste is similar to the one provided by VTT within the CEBAMA project (Vehmas et al., 2016), with the exception that quartz filler is not added to the mix. For the leaching experiments, cylindrical cement monoliths

were cast with a diameter of 15 mm and a height of 15 mm and cured for 28 days in an oven at 40 ºC and 95 % RH. After curing, the top and bottom ends of the cylinders were sealed with resin in order to force radial diffusion between the monoliths and the surrounding groundwater. Prior to the experiments, the hardened cement pastes were characterized inter alia by XRD, SEM, and TGA. For selected samples, additionally micro-X-ray computer tomography (µXCT) imaging data were obtained. The samples were placed into 60 mL vessels and submerged in 50 mL leaching solution in oxygen and CO_2 free atmosphere at 40 ºC, while allowing equilibration for several months. The experiments were performed with different synthetic solutions, namely granitic groundwater, clay water, and saline (sea) water. Every two months the solution was replaced by fresh leaching solution. The sampled solution was analysed with respect to Ca, Si, Al, K, S and Mg concentrations, pH, etc. The experiments addressing the leaching of the CEBAMA reference paste in granitic water were chosen as benchmark for our simulation work dealing with pore-scale effects resulting from cement paste degradation and alteration.

7.3 MODEL DEVELOPMENTS AND SETUP OF SIMULATIONS

The features of *iPP* have been described in detail in Rohmen et al. (2018). More recently, a number of improvements and additional features were implemented and used for the simulations described here, e.g. regarding the Lattice-Boltzmann transport scheme, the conceptual and mathematical description of diffusion in C-S-H, and the performance enhancement of the chemical solver.

Updated Lattice-Boltzmann transport scheme

The collision operation used in all simulations was an implementation of a Two-Relaxation-Time (TRT) scheme into the Palabos framework. The stability of the TRT scheme is a major enhancement compared to Single-Relaxation-Time (SRT) types of techniques which were replaced in the whole modelling setup. This allows stable simulation of heterogeneous systems with a larger contrast of diffusion coefficients. The particular TRT scheme was extensively described and analysed by Ginzburg et. al (2008) and Vikhansky and Ginzburg (2014). This special TRT collision operator allows simulating the diffusion equation respecting transient porosity changes during dissolution and precipitation processes without the need of another artificial source term. Other common collision operators, as for example in the SRT *diffusion velocity* scheme (Perko and Patel, 2014), cannot take into account the transient term by its own and an additional correction is mandatory.

Updated homogenization scheme for diffusion in C-S-H and hydration products

The pore-scale model of hardened cement paste considers explicitly different phases: (1) water saturated pores, (2) clinker phases, (3) binder phases and additives (i.e. blast furnace slag and silica fume), and (4) a homogeneous continuum of hydration products. Clinker and binder phases are considered as non-diffusive. The effective diffusion coefficient and porosity of the hydration products in the hardened cement paste depend on the volume fraction of C-S-H and other hydration products. To estimate the diffusion coefficient of the hydration products phase, a multiscale homogenization model (effective medium approach) was applied (Stora et al., 2009, Patel et al., 2018). This model includes multiple steps for spatial levels of homogenization. A free water diffusion coefficient of 2.2E-9 m^2/s was used as basis which corresponds to the value of Ca, which is a major solute in cement pore water.

At the lowest-scale homogenization level, low-density (LD) and high-density (HD) C-S-H is distinguished and only nitrogen accessibly porosity is assumed contributing to diffusion. The nitrogen accessible porosity has to be distinguished of the gel porosity, which is about 37 % and 24 % for LD and HD C-S-H, respectively (Ulm et al., 2004). Nitrogen accessible porosity was determined to 17.8 % and 0 % for LD and HD C-S-H, respectively, rendering HD C-S-H a non-

diffusive phase (Tennis and Jennings, 2000). While some researchers have assumed that HD C-S-H has no nitrogen accessible porosity for modelling purposes (e.g. Patel et al., 2018) other researchers have stated that the accessible porosity is increased upon degradation of the C-S-H phase by 6.5 % (Stora et al., 2009). Therefore, we assumed a linear relationship for both, LD and HD C-S-H, in dependency of Ca/Si solid ratio, introducing additional porosity of maximum 6.5 % when reaching a Ca/Si ratio of 0.8 and no additional degradation porosity at Ca/Si ratio of 1.67. With this porosity information and assuming spherical building blocks the diffusion coefficient of both C-S-H types can be estimated using the differential effective media technique (Phan-Thien and Pham, 2000). The gel water diffusion coefficient in C-S-H was reduced by a factor of 10 to 2.2E-10 m^2/s due to constrictivity effects (Phung et al., 2018).

At the next homogenization level, non-diffusive hydration products different from C-S-H and capillary porosity fractions are introduced in each C-S-H type separately. In order to separate the LD and HD C-S-H volume fractions, the model of Tennis and Jennings (2000) is applied. This model needs the water-to-cement (w/c) ratio and the degree of hydration as input data. The values used were 0.25 for w/c (from the mix design) and 0.85 for degree of hydration, which was estimated by segmentation of µXCT data by a cement hydration model with PhreeqC. Another assumption made was that capillary porosity is only introduced into LD C-S-H (i.e. it is absent in HD C-S-H), while all non-diffusive phases are dispersed homogeneously into LD and HD C-S-H, relative to their volume fractions. The model used for estimating the diffusion coefficients at this level was based on the Mori-Tanaka homogenization scheme (e.g. Bary et al., 2014, Stora et al., 2009).

In the last homogenization level, both types of C-S-H, including the non-diffusive hydration products and capillary porosity, are upscaled. To this end, the Mori-Tanaka scheme is again used by respecting the new volume fractions including all other phases. The initial diffusion coefficient of the hydration products continuum was determined by this way as 8.26E-12 m^2/s.

Performance enhancement of the chemical solver

Although PhreeqcRM supports MPI parallelization during the *PhreeqcRM::runCells()* function call, concentration update/requesting and retrieving of auxiliary information (e.g. solid phase compositions, pH values, etc.) are implemented with a global MPI reduction and collecting step. The implication of the reduction step is that all concentration couplings to transport codes are forced to be done via the main process and cannot perform on a local process basis. This reduction procedure causes high communication overhead and a major performance drawback when utilizing parallelization on a high amount of CPU nodes, leading eventually to negative scalability. In order to reduce this communication overhead, the PhreeqcRM code was optimized, which led to a custom PhreeqcRM version allowing local coupling to the Lattice-Boltzmann transport code. This optimization significantly improved the performance scalability behaviour. This was tested on JURECA cluster (Intel Haswell Xeon compute nodes; 24 CPU cores / 48 threads each) (Jülich Supercomputing Centre, 2018). As tested model, a cement paste 3D model including chemistry simulation for Ca and Si phases (i.e. discrete C-S-H solid solution and portlandite as solid phases) and a size of 67 x 66 x 66 = 291,852 lattice nodes was used. This simulation shows still scalability at utilized 16 compute nodes (i.e. 384 CPU cores / 768 threads), i.e. computational performance is still gained with applying more compute nodes. Even better scalability behaviour is expected with for larger models encompassing more lattice nodes.

Geometrical and chemical setup of the simulations

The microstructure of the hardened cement paste was derived from the experimental data on the characterization of the CEBAMA low-pH reference cement paste provided by USFD (cf. Vasconcelos et al., 2018). These data encompassed in particular imaging data from µXCT, performed on samples of the CEBAMA reference paste cast at USFD, which were used as input for reconstructing the microstructure of the hardened cement paste for the simulations.

Cylindrical samples with dimensions of 2 mm in diameter and 5 mm in height were used for µXCT measurements. The data were provided in a raw volume image data format from which microstructural geometrical descriptions of the low-pH cement paste were derived. The sample was cured for 28 days and then measured by µXCT with a resolution of 3 µm per voxel, resulting into a grey value data set of 671 *x* 742 *x* 1449 = 721 431 018 voxels. These image data resolve the grey values of unhydrated clinker (C_2S/C_3S and C_3A/C_4AF), blast furnace slag (BFS), silica fume, voids (air) and hydration products (mainly C-S-H). Different hydration products could not be further distinguished and separated due to the similar X-ray attenuation effects (see Figure 7.1, left). For further information, see also Rohmen et al. (2017).

An artefact which is commonly known from CT measurements is the so-called partial volume effect, also referred to as volume averaging artefact. It occurs when a single voxel contains more than one phase, leading to an intermediate X-ray attenuation value between all material fractions present in the voxel's volume (Ketcham and Carlson, 2001). As a consequence, separating the different phases by a simple grey value thresholding algorithm would eventually lead into false positive assignments for voxels corresponding to phase mixtures. In this work, a more sophisticated segmentation algorithm was developed to mitigate the partial volume effect (Rohmen et al., 2017). Using this algorithm, a three-dimensional (3D) phase distribution of the cement paste specimen could be derived, in which air, silica fume, calcium silicate clinker, blast furnace slag, ferrite clinker and hydration products could be distinguished. Unfortunately, further separating of different phases in the subset of hydrates was not possible. The relative volume fractions determined by this way are depicted in Table 7.1. In order to assign chemical properties to the hydration products homogeneous phase, results of a PhreeqC hydration model were used (Idiart et al., 2018), as detailed in Table 7.2). For all *iPP* simulations, the same database as in the cement hydration modelling performed by Idiart et al. (2018) was used, i.e. ThermoChimie_eDH_v9b0 (Giffaut et al., 2014).

Determination of effective diffusion coefficients

According to Fick's first law, at steady state the diffusion coefficient is calculated as the quotient of the diffusive flux and the concentration gradient in a through diffusion setup. To simulate this at the microscopic scale, the microstructure and transport properties of the different components are needed. The 3D modelled geometry of the microstructure is used to determine the effective diffusion coefficient in the x, y, and z directions to determine possible anisotropic diffusivity. To this end, closed (slip) boundary conditions are imposed on all boundaries, except the two faces perpendicular to the direction for which diffusivity is obtained.

A constant concentration (Dirichlet) boundary condition of an inert tracer is imposed at one boundary (1 mol/L) and at the opposite boundary (0 mol/L). The initial concentration profile is initialized linearly in order to speed-up convergence of the simulation. Subsequently, the diffusive flux is tracked, and the effective diffusion coefficient can be calculated as described above, when steady state is reached. In order to determine the effective diffusion coefficient of the cement paste sample, a representative cube with dimensions of 750 x 750 x 750 µm (250 x 250 x 250 voxels with a resolution of 3 µm per voxel) was extracted from the segmented µXCT data (Figure 7.1, right).

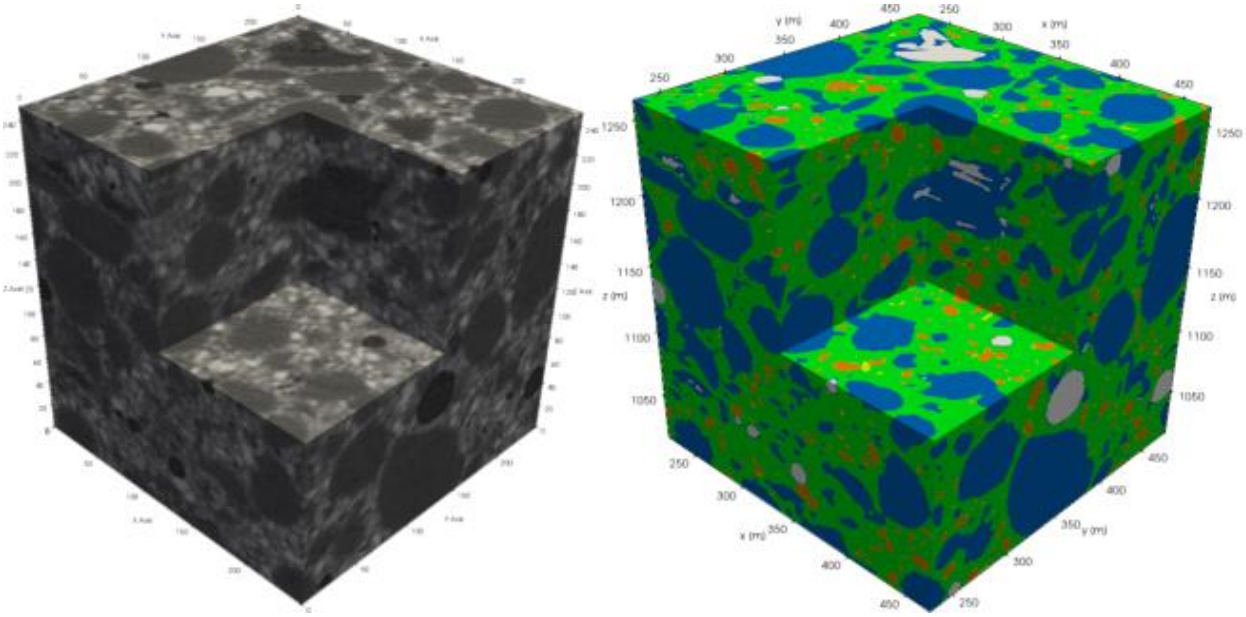

Figure 7.1. *Original µXCT raw grey image data corresponding to the extracted cube (left) and microstructure of CEBAMA reference paste from segmented µXCT data used as input geometry for the calculation of effective diffusion coefficients (right). A box was clipped from the cube for illustrative purposes. Phases: Air (white), silica fume (blue), alite/belite (yellow), blast furnace slag (orange), ferrite (red) and hydration products (green). Total model size is 750x750x750 µm with a resolution of 3 µm.*

Table 7.1. *Voxel count and volume fractions of segmented µXCT data. Air is interpreted as void and all non-hydration products except of air is interpreted as solid/non-diffusive*

Phase	count voxel	volume fraction
void / porosity	482,755	0.031
solid / non- diffusive	7,117,164	0.455
hydration products	8,025,081	0.514

Table 7.2. *Calculated amounts per unit volume and volume fractions of hydration product phases in the USFD cement paste after 28 days of hydration. Volume fractions of C-S-H correspond to volumes with gel porosity excluded. The amounts were estimated by a cement hydration model using PhreeqC (Idiart et al., 2018).*

Phase	c [mol/L]	volume fraction
CSH 0.8	2.723	0.091
CSH 1.2	11.994	0.488
Ettringite	0.083	0.033
Calcite	0.136	0.003
Hydrotalcite	0.315	0.039
Straetlingite	0.606	0.074
Inert	-	0.028
Hydrates capillary porosity (ϕ_c)	-	0.059
Hydrates gel porosity (ϕ_g)	-	0.185
Hydrates total porosity ($\phi_c + \phi_g$)	-	0.244

Simulation of leaching experiments

The leaching of the CEBAMA low-pH reference paste by granite water (Table 7.3, from Vasconcelos et al., 2018) was simulated with *iPP*. The initial composition of the granitic water provided by USFD (Table 7.3, column c_{init}) was oversaturated with respect to calcite using ThermoChimie. In the model, the water was equilibrated with calcite and the resulting pH change was compensated by charge balancing with chloride (Table 7.3, column c_{sim}). Regarding the phase composition and microstructure, a rectangular 2D cross-section of the microstructure of the USFD cement paste derived from the µXCT was extracted to generate a 2D input geometry. The 2D cross-section was setup as a closed system except for the left boundary, where a 1-voxel pure water reservoir and a granite water boundary condition were imposed. All other phases except of the hydration products were regarded as inert. In particular, for the unhydrated clinker phase this is an over-simplification since the hydration reaction would proceed further at the same time as leaching occurs. However, to our knowledge, no kinetic rate equations are yet available from experiments describing the rate of the hydration reaction at the microscopic scale. The simulations were performed at a temperature of 40°C in accordance with the experimental setup. Since the pore size in the gel porosity of the C-S-H phase is in the nanoscale, mineral precipitation in the gel porosity was restricted (Elakneswaran and Ishida, 2014).

Table 7.3. *Composition of the reported and used granitic water (Vasconcelos et al., 2018).*

Element	c_{init} [mmol/L]	c_{sim} [mmol/L]
C	2.02	0.86
Ca	0.5	0.5
Cl	2.18	3.227
K	0.1	0.1
Mg	0.2	0.2
Na	2.8	2.8
S	0.1	0.1
Si	0.2	0.2
pH	8.2	8.2

7.4 RESULTS

Effective diffusion coefficients of the hardened cement paste

After steady-state was reached, the diffusion coefficient was calculated based on Fick's law. The resulting concentration profile and flux streamlines for the z-direction are presented in Figure 7.2. From the outlet fluxes, the effective diffusion coefficients for each direction were estimated, as shown in Table 7.4. The values for all directions are quite similar ($3.47 \cdot 10^{-12} \pm 0.28 \cdot 10^{-12}$ m^2/s), suggesting that the diffusivity is quasi-isotropic for the depicted sub-geometry of the hardened cement paste. It should be noted here that these effective diffusion coefficient values correspond to a microstructure that was obtained after 28 days of hydration. In the model, no further hydration is considered and thus the model results correspond to the 28-day diffusion coefficient. It is expected that further hydration after 28 days will have the effect of reducing significantly the diffusivity. Thus, long-term degradation processes should be assessed with diffusion coefficients obtained from well-hydrated systems, which in low w/c ratio mixes may take substantially longer than 28 days.

For comparison, the cement paste effective diffusion coefficient was estimated by homogenizing the pore-scale modelled geometry using the Mori-Tanaka (MT) scheme. To this end, the volume fractions of hydration phases, inert solids and voids given in Table 7.1 were used, together with a

diffusion coefficient of the hydrates of 8.26E-12 m^2/s (see paragraph about homogenization scheme for hydrates above). The result is also depicted in Table 7.4 and shows that the MT technique yields a 20 % higher diffusion coefficient compared to the average value derived from the pore-scale model for this geometrical setup. This may suggest that some inaccessible porosity and geometrical effects can play a non-negligible role here. In this line, it is important to evaluate the accuracy needed for an upscaled model, i.e. whether the MT technique is sufficient for providing reliable values of diffusivities, or if complex numerical simulations are needed instead.

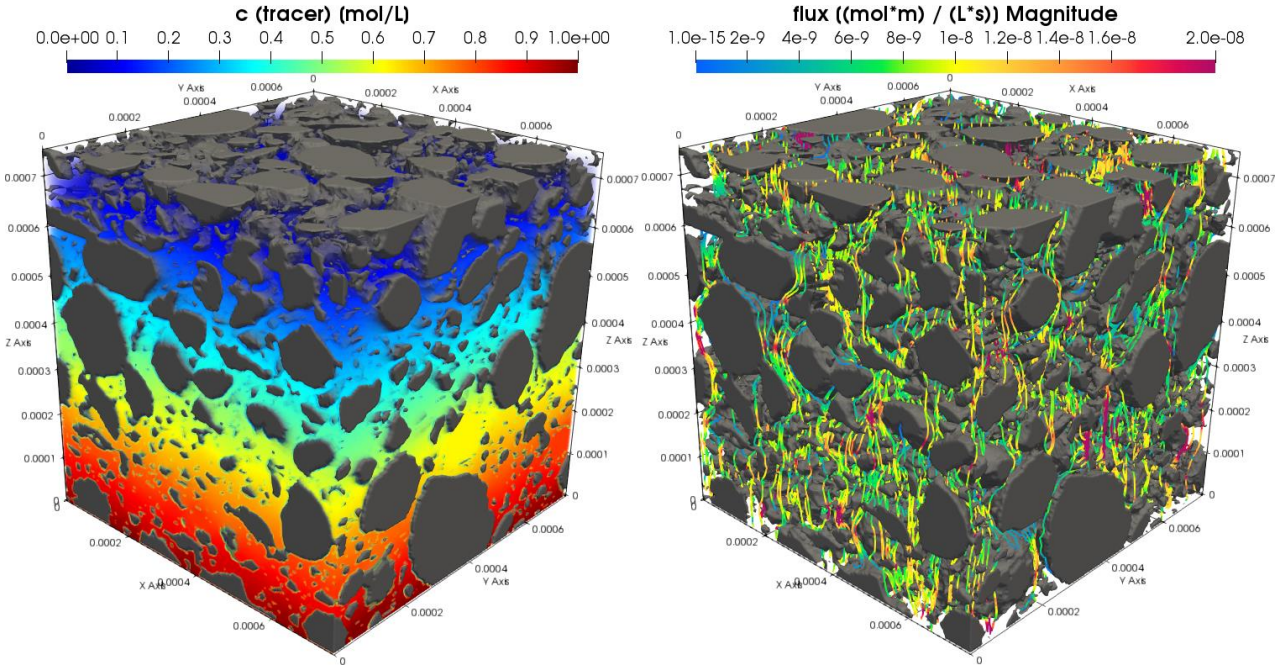

Figure 7.2. *Tracer concentration profile (left) and diffusive flux streamlines (right) of inert tracer after convergence of diffusion coefficient simulation in z-direction. Non-diffusive phases are indicated in grey while hydration products and voids are transparent.*

Table 7.4. *Results for the effective diffusion coefficient calculations for each spatial axis, average value and estimation by Mori-Tanaka homogenization scheme.*

Direction	D_e [m^2/s]
x	3.55E-12
y	3.69E-12
z	3.19E-12
Average	3.47E-12
Mori-Tanaka	4.18E-12

Leaching of cement paste with granite water

The 2D model was run for 5.4 million iterations, equivalent to a physical time of 40 seconds. Some of the results are shown in Figures 7.3 to 7.6. It can clearly be seen that calcite is already precipitating as a clogging and passivating crust on the paste surface on the left-hand side (Figure 7.3). Figure 7.4 shows the average phase assemblage perpendicular to the leaching front. As indication for the depth addressed in Figure 7.4 (100 µm), a vertical green line is shown in Figure 7.3 (left) at this depth. One can observe that C-S-H is only degraded in the first 30 µm of the sample in the simulation. At the same time, the C-S-H is mainly replaced by calcite and hydrotalcite. Supporting information is shown in Figure 7.5, indicating a significantly decreased Ca/Si ratio of

the C-S-H in the leached zone, while the porosity shows a down-up-down shape. The latter effect has also been reported from imaging data of carbonation experiments of cement paste and termed as carbonated and dissolution zone (Šavija and Luković, 2016). Due to lack of knowledge about the transport properties of the calcite layer in the simulation, no special treatment is assigned to calcite formation and its impact on diffusivity. Thus, the dissolution rate of the hydrates is rather limited after some equilibration time of about 10 minutes, which can be observed in Figure 7.6. Therefore, clogging is likely to occur more rapidly in the simulation than in the experiments (Vasconcelos et al., 2018). A more detailed investigation of the impact of calcite precipitation on transport properties of the carbonated zone is on-going.

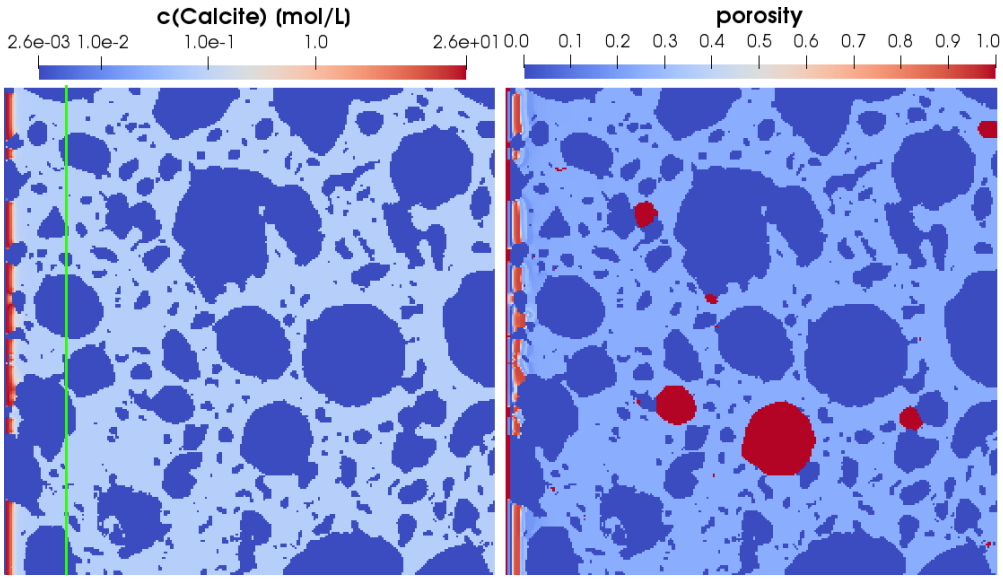

Figure 7.3. *Calcite concentration in mol/L (left) and porosity (right) after leaching of the cement paste with granite water for 40 minutes. The size of the plot is 750 x 750 µm.*

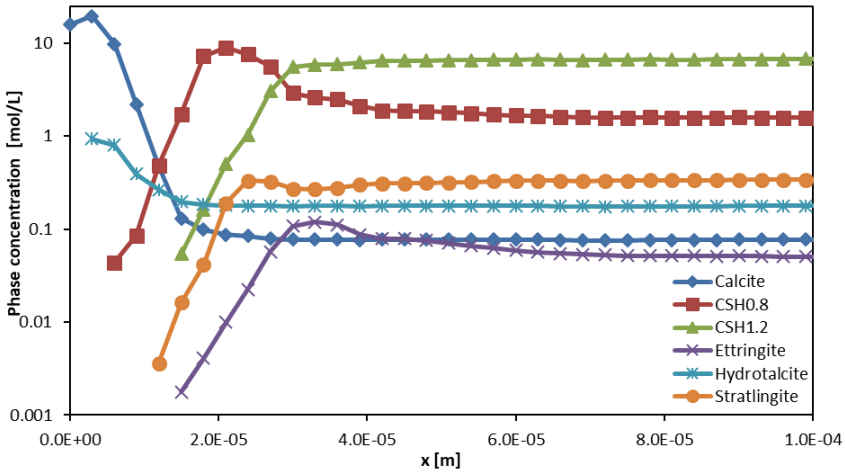

Figure 7.4. *Average solid phase concentrations at the interface after leaching with granite water for 40 minutes.*

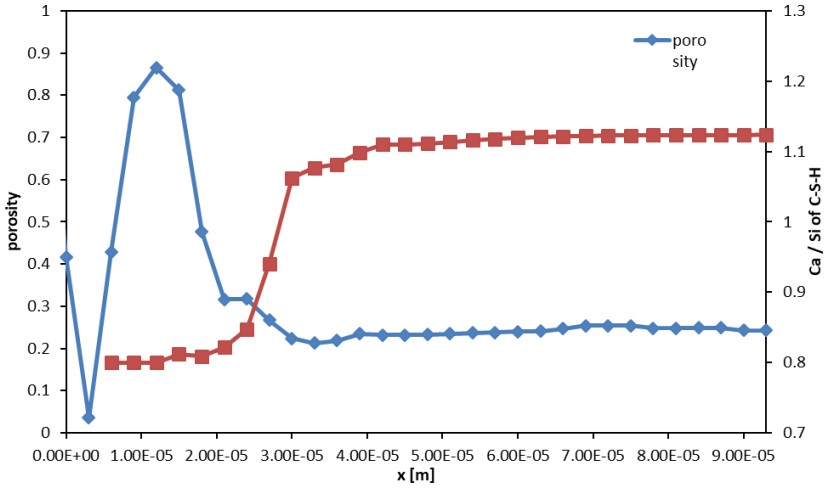

Figure 7.5. *Average porosity (blue, left axis) and Ca/Si ratio of C-S-H phase (red, right axis) at the cement paste interface after leaching with granite water for 40 minutes.*

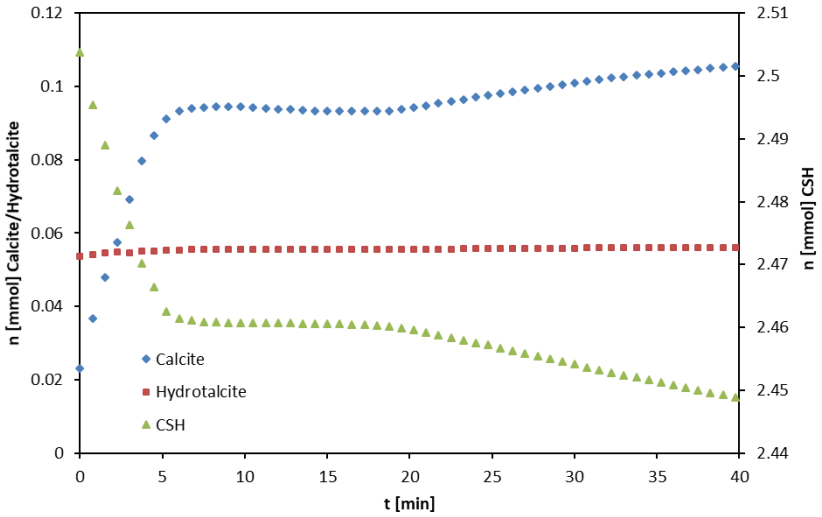

Figure 7.6. *Total amounts of calcite (blue, left axis), hydrotalcite (red, left axis) and C-S-H (green, right axis) in the complete 2D model against time in contact with granitic leaching water.*

7.5 CONCLUSIONS AND OUTLOOK

The *iPP* simulator developed within the CEBAMA project for the modelling of reactive transport processes at the pore-scale was applied to simulate leaching experiments on low-pH cement pastes (Vasconcelos et al., 2018). Several algorithms and approaches were developed and implemented to derive microstructural information in appropriate format from µXCT volume images for subsequent usage in *iPP*. It has been shown that the developed framework is capable of simulating solute transport in experimentally-derived data to predict effective diffusion coefficients and microstructural changes due to dissolution/precipitation reactions involving hydration products. Moreover, refinements of the multiscale homogenization model for diffusive phases in the cement paste (i.e. C-S-H gel) were developed.

Using the latest development status of *iPP*, a directionally averaged effective diffusion coefficient of the VTT reference paste of 3.47E-12 m^2/s was determined in a 3D setup. However, it should be noted that this value refers to the USFD mixture (i.e. without quartz filler) for a curing time of only 28 days, i.e. this value is probably not representative of the long-term properties of the VTT reference paste. Furthermore, the leaching of the cement monoliths with granitic water was

simulated in 2D, indicating precipitation of calcite at the surface of the cement monolith and a distinctive lowering of the Ca/Si ratio of C-S-H in the leached zone, accompanied by significant porosity changes. To further enhance the realism of the simulations, a diffusivity model for the calcite layer precipitating as passivating crust at the cement paste/solution interface should be envisaged. Additionally, improved upscaling models have to be derived in order to extrapolate the simulation results and mass fluxes obtained on the pore scale to the time scales of the experiments, which are in the range of several months to years.

In addition, further optimizations were tested to improve the numerical performance constraints of Pore-scale reactive transport simulations, which are very computationally demanding, even with high performance cluster computing, using the HPC facilities at the Jülich Supercomputing Centre (JSC, 2018). Relaxing the performance limitations would enable reactive transport simulations using 3D microstructures.

Acknowledgements

The research leading to these results has received funding from the European Union's Horizon 2020 Research and Training Programme of the European Atomic Energy Community (EURATOM) (H2020-NFRP-2014/2015) under grant agreement n° 662147 (CEBAMA). The authors gratefully acknowledge the computing time granted through JARA-HPC on the supercomputer JURECA at Forschungszentrum Jülich, Germany.

7.6 REFERENCES

Bary, B., Leterrier, N., Deville, E., Le Bescop, P. (2014). Coupled chemo-transport-mechanical modelling and numerical simulation of external sulfate attack in mortar. Cement and Concrete Composites, 49, 70–83.

Elakneswaran, Y. and Ishida, T. (2014). Development and verification of an integrated physicochemical and geochemical modelling framework for performance assessment of cement-based materials. Journal of Advanced Concrete Technology, 12(4), 111–126.

FlowKit. (2011). Palabos user guide.

Giffaut, E., Grivé, M., Blanc, P., Vieillard, P., Colàs, E., Gailhanou, H., Gaboreauc, S., Marty, N., Madé, B., Duro, L. (2014). Andra thermodynamic database for performance assessment: ThermoChimie. Applied Geochemistry, 49, 225–236.

Ginzburg, I., Verhaeghe, F., D'Humieres, D. (2008). Two-relaxation-time Lattice Boltzmann scheme: about parametrization, velocity, pressure and mixed boundary conditions. Communications in Computational Physics, 3(2), 427–478.

Idiart, A., Laviña, M., Olmeda, J. (2018). Influence of internal relative humidity on the hydration of a low-pH cement. A modelling study. In Proc. 3rd Annual Workshop CEBAMA project, Nantes (France), April 2018, (in press).

Jülich Supercomputing Centre. (2018). JURECA: Modular supercomputer at Jülich Supercomputing Centre. Journal of large-scale research facilities, 4, A132.

Ketcham, R. A. and Carlson, W. D. (2001). Acquisition, optimization and interpretation of x-ray computed tomographic imagery: Applications to the geosciences. Computers and Geosciences, 27(4), 381–400.

Mohamad, A. A. (2011). Lattice Boltzmann Method. London: Springer London.

Parkhurst, D. L. and Wissmeier, L. (2015). PhreeqcRM: A reaction module for transport simulators based on the geochemical model PHREEQC. Advances in Water Resources, 83, 176–189.

Patel, R. A., Perko, J., Jacques, D., Schutter, G. De, Ye, G., Bruegel, K. Van. (2018). Effective diffusivity of cement pastes from virtual microstructures: Role of gel porosity and capillary pore percolation. Construction and Building Materials, 165, 833–845.

Perko, J., and Patel, R. A. (2014). Single-relaxation-time lattice Boltzmann scheme for advection-diffusion problems with large diffusion-coefficient heterogeneities and high-advection transport. Physical Review E - Statistical, Nonlinear, and Soft Matter Physics, 89(5), 1–9.

Phan-Thien, N., and Pham, D. C. (2000). Differential multiphase models for polydispersed spheroidal inclusions: Thermal conductivity and effective viscosity. International Journal of Engineering Science, 38(1), 73–88.

Phung, Q. T., Maes, N., Jacops, E., Jacques, D., De Schutter, G., Ye, G. (2019). Insights and issues on the correlation between diffusion and microstructure of saturated cement pastes. Cement and Concrete Composites, 96, 106–117.

Rohmen, S., Idiart, A., Deissmann, G., Bosbach, D. (2017). In Ed. Idiart A. (2017). D3.05: Preliminary results and interpretation of the modelling of WP1 & WP2 experiments. 22–30.

Rohmen, S., Idiart, A., Deissmann, G., Bosbach, D. (2018) Pore-scale reactive transport modelling of transport and leaching processes in cementitious materials, Proc. 3rd Annual Workshop CEBAMA project, Nantes (France), April 2018.

Stora, E., Bary, B., He, Q.-C., Deville, E., Montarnal, P. (2009). Modelling and simulations of the chemo-mechanical behaviour of leached cement-based materials: Interactions between damage and leaching. Cement and Concrete Research, 40(8), 1226–1236.

Succi, S. (2001). The Lattice Boltzmann Equation for fluid dynamics and beyond. Oxford.

Šavija, Branko, and Mladena Luković (2016). Carbonation of Cement Paste: Understanding, Challenges, and Opportunities. Construction and Building Materials, 117, 285–301.

Taylor, H. F. W. (1997). Cement chemistry. Thomas Telford.

Tennis, P. D., and Jennings, H. M. (2000). A model for two types of calcium silicate hydrate in the microstructure of Portland cement pastes. Cement and Concrete Research, 30(6), 855–863.

Ulm, F. J., Constantinides, G., Heukamp, F. H. (2004). Is concrete a poromechanics materials? - A multiscale investigation of poroelastic properties. Materials and Structures, 37(1), 43–58.

Vasconcelos, R., Walkley, B., Hyatt, N., Provis, J., Corkhill, C. (2018). The physico-chemical evolution of a low-pH cement in contact with groundwater, Proc. 3rd Annual Workshop CEBAMA, Nantes (France), April 2018.

Vehmas, T., Schnidler, A., Löija, M., Leivo, M., Holt, E. (2016). Reference mix design and castings for low-pH concrete for nuclear waste repositories. Proc. 1st Annual Workshop CEBAMA, Barcelona, Spain, May 2016.

Vikhansky, A., and Ginzburg, I. (2014). Taylor dispersion in heterogeneous porous media: Extended method of moments, theory, and modelling with two-relaxation-times lattice Boltzmann scheme. Physics of Fluids, 26(2).

9 NRG/ J.C.L. Meeussen

9.1 DESCRIPTION OF THE MODELLING WORK

This deliverable describes the work carried out by each of the participants of Work Package 3 (WP3) related to Modelling and Interpretation of the Experiments to be carried out within Work Package 1 (WP1). The Working Plan is based on Appendix B of the Proposal of the CEBAMA (Cement-based materials, properties, evolution, barrier functions) project. A detailed description of the work to be carried out can be found in that appendix and will therefore not be repeated here.
In our earlier progress reports we have described the work on the numerical implementation of electromigration within the ORCHESTRA reactive transport framework (Meeussen, 2003). The new model was evaluated by reproducing the 1D diffusion calculation benchmarks described by Rasouli et al. (2015). The calculated results of two benchmarks agree very well with the reported results, which indicates that the implementation in ORCHESTRA is correct.

The final part of this work was carried out during 2018 and early 2019 and consisted of testing the new software module. To this end, model calculations were compared with experimental work carried out within CEBAMA at the TU-Delft. Furthermore, NRG participated in the WP3 Modelling Task benchmark exercise in which different model codes were compared to each other (Idiart et al., 2019).

During the final reporting period this work has focused on the following subjects:

1) Testing the implementation of electromigration within the ORCHESTRA framework by performing calculations for the cement/clay diffusion experiments carried out at the TU-Delft (Meeussen et al., 2018).
2) Testing the implementation of the electromigration module within ORCHESTRA for more complex systems by participating in the WP3 Modelling Task benchmark exercise.

At the April 2018 CEBAMA meeting in Nantes, an oral presentation was given (Meeussen et al., 2018) in which the structure of the electromigration implementation in ORCHESTRA was explained.

9.2 SET-UP OF DIFFUSION EXPERIMENTS BY TU-DELFT

A diffusion model was used for solute migration in a Boom Clay - Concrete system that aimed to assist with the set-up of the experimental work by TU-Delft. The cement model includes the latest CEMDATA14 thermodynamic database with chemical reactions specific of cementitious systems (EMPA, Lothenbach). This model was used to design the Cement-Clay interaction experiment and to estimate the time and spatial scales over which alterations are to be expected.

The design of the electromigration cell used in the experiments by TU-Delft within WP1 (Bykov et al., 2016) was manufactured from a single Plexiglas piece and has in the centre a cylindrically shaped sample compartment with the dimension of 10 × 3 cm, and two electrolyte compartments on both sides of the cell with a total volume of 100 cm^3 each. Two hollow Teflon tubes with the outer dimension of 30 mm × 50 mm were used as clay sample holders inside the sample compartment. These were necessary for the preparation of homogeneous clay cores. During the experiments, the sample was sealed off from the electrolyte compartments by two glass filters with a pore size of 10 μm to 16 μm. These filters allow the electrolyte solutions to flow into the sample and prevent clay particles from entering the electrode compartments. The electrical field in the cores was continuously monitored during experiments.

Example calculations (Figure 9.1) showed that good agreement between experimental and calculated migration rates could be obtained at different external potential gradients and migration times.

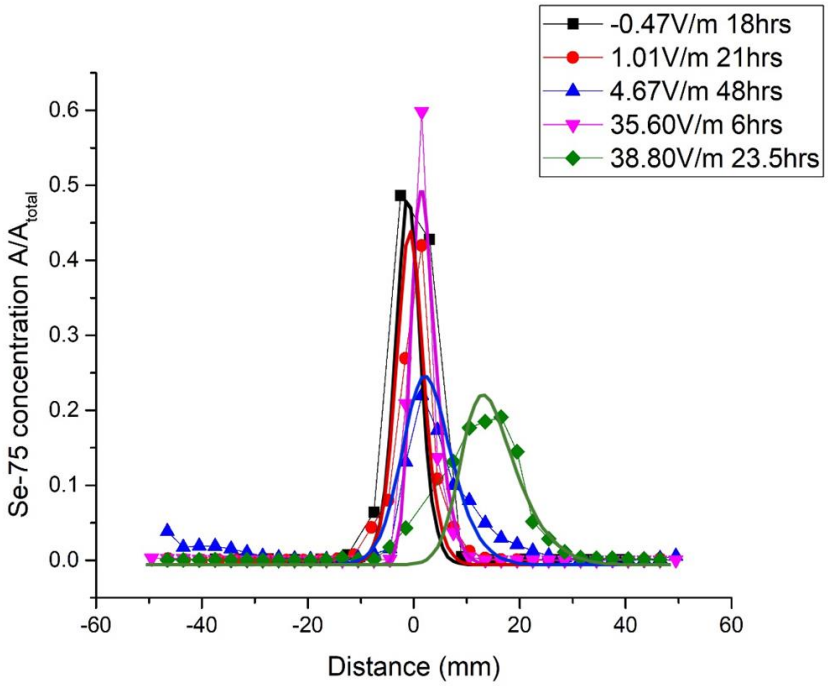

Figure 9.1. *Comparison of calculated (NRG) and measured (TU-Delft) electromigration of selenate in Boom Clay.*

The structure of the implementation of electromigration calculations in ORCHESTRA is quite different from existing approaches (e.g. Rasouli et al., 2015; Steefel et al., 2015). A paper on this subject is in preparation. In contrast with the generally used approach to exchange individual species concentrations between the chemical and transport modules, the new ORCHESTRA approach summarizes the detailed species information to that at component level. Part of the calculations necessary for solving the transport equations are carried out by the chemical equilibrium module.

This results in:

- significantly less information exchange between transport and chemical equilibrium modules,
- less information that needs to be stored in between timesteps (no species data, only component data)
- a greater part of the calculations can take place in parallel because the chemical calculations are already parallelized
- the required code is much simpler and more efficient,
- the implementation is compatible with existing code (easy to switch multicomponent diffusion on or off).

The approach requires solving one extra equation within the transport expressions (solve potential gradient that results in given charge flux). However, this can be done using the standard ORCHESTRA feature to solve equations.

The implementation was evaluated by simulating several proposed cases of the Modelling Task benchmark exercise in WP3 (Idiart et al., 2019) with the electromigration / multicomponent diffusion option switched on. The only other code that was used to evaluate the option of

multicomponent diffusion was the MP3 code, as operated by ANDRA (B. Cochepin), which yielded comparable results.

The calculation time for taking into account charge potential effects on diffusion within ORCHESTRA was only about 10-30% longer than the Fickian diffusion case.

9.3 CONCLUSIONS AND OUTCOMES

- Within the Cebama project NRG has implemented an electromigration module within the ORCHESTRA framework.
- This module allows to take into account charge and potential effects during reactive transport simulations.
- The correctness of the implementation was first tested against a number of simple published benchmark problems with a small number of chemical components (Meeussen, 2017).
- Subsequently the module was used to design transport experiments that were carried out by the TU Delft.
- Comparing simulated and measured results showed good agreement.
- The module was used to simulate a much more complex reactive transport system as defined withing the context of the Cebama Modelling Task benchmark exercise.
- Calculated results were compared between different codes, showing in general good agreement.
- The ORCHESTRA implementation only takes 10-30% more calculation time than a version without potential/charge effects switched on.

Acknowledgements

The research leading to these results has received funding from the European Union's Horizon 2020 Research and Training Programme of the European Atomic Energy Community (EURATOM) (H2020-NFRP-2014/2015) under grant agreement n° 662147 (CEBAMA).

9.4 REFERENCES

Bykov, D., Sabau, A., Yigittop, Y., Kloosterman, J-L., Konings, R., Meeussen, J. C. L. (2016). Experiments on a cement-clay interface and the impact on physical properties: The Dutch context. In Mechanisms and Modelling of Waste/Cement Interactions - Morat, Switzerland, May 2016.

Idiart, A., et al. (2019). Final Report on the Modelling Task. CEBAMA Deliverable D3.07, Brussels, Belgium.

Meeussen, J.C.L., Bykov, D., Sabau, A. (2018). Electromigration of Se in Bentonite and Boom Clay: comparing model and experiment. CEBAMA 3rd Annual Workshop, Nantes, France, April.

Meeussen J.C.L. (2016). Contribution to CEBAMA deliverable: D3.04 Description of and results from the modelling of external lab and/or field experiments.

Meeussen J.C.L. (2017). Contribution to CEBAMA deliverable: D3.05 Preliminary results and interpretation of the modelling by incorporating results from WP1 and WP2 experiments.

Meeussen, J.C.L. (2003). ORCHESTRA: An object-oriented framework for implementing chemical equilibrium models, Environmental science & technology 37 (6), 1175-1182.

Rasouli, P., Steefel, C. I., Mayer, K. U., & Rolle, M. (2015). Benchmarks for multicomponent diffusion and electrochemical migration. Computational Geosciences, 19(3), 523-533.

Steefel, C.I., Appelo C.A.J., Arora B., Jacques D., Kalbacher T., Kolditz O., Lagneau V., Lichtner P.C., Mayer K.U., Meeussen J.C.L., Molins S., Moulton D., Shao H., Šimůnek J., Spycher N., Yabusaki S.B., Yeh G.T. (2015). Reactive transport codes for subsurface environmental simulation, Computational Geosciences, 19, 445-478.

11 SCK·CEN/ L. Yu, L. Lemmens, Q.T. Phung, J. Perko, D. Jacques (Waste & Disposal Expert Group, Belgian Nuclear Research Centre)

11.1 TOOL DEVELOPMENT – AN APPROACH FOR MODELLING LEACHING AND PRECIPITATION WITH A PORE-SCALE MODEL

A flow chart of the developed approach to simulate leaching and precipitation accounting for the microstructure of hardened cement paste is presented in Figure 11.1. Transport of multiple components and geochemical processes (dissolution and precipitation of multiple solid phases) are considered in the model by coupling sequentially two modules: a lattice Boltzmann solver for transport (LB) and Phreeqc for geochemical processes. The microstructure representative for the hardened cement paste is digitized based on SEM images. Only portlandite, clinker phases, the C-S-H phase and capillary pores are explicitly represented for simplicity. Clinker phases are non-diffusive, while portlandite and C-S-H, as well as the subsequently precipitated calcite, are treated as porous media (because initial porosities for these phases are required when using multilevel LB method, they are assumed to have a negligible porosity), with effective diffusivities calculated for each cell based on the porosity of the cell. The diffusivity of ions in capillary pores is equal to the molecular diffusion in water (D_0 = 1E-9 m^2/s). The non-diffusive and diffusive phases in cement microstructure determine the coexistence of both continuum and pore scales in the modeling, which is termed as multilevel porous media. The following governing equation of diffusion in multilevel porous media can be solved by Lattice Boltzmann multilevel scheme which was already coded into an in-house package —Yantra (Patel, 2016):

$$\frac{\partial(\theta c^j)}{\partial t} = \nabla \cdot \left(\theta D_0 \xi(\theta) \nabla c^j\right) + ss^j \qquad (11.1)$$

where c^j is concentration of the jth species, D_0 is the free liquid diffusion coefficient, θ is porosity, $\xi(\theta)$ is tortuosity, ss^j is the source or sink term of the jth species. The following key points are considered in the modeling of dissolution and precipitation:

- The initial composition of hardened cement paste consists of four phases: unhydrated clinker, portlandite, C-S-H matrix and capillary pores, with each type cell assigned with a distinct node-type:
  - capillary pores with node-type of -1, considered to be non-reactive and diffusive
  - capillary pores with node-type of 0 when adjacent to at least one cell where solid mass occupies more than 80% cell volume, considered to be reactive and permeable
  - portlandite with node-type of -10, considered to be reactive and permeable
  - C-S-H with node-type of -5, considered to be reactive and permeable
- The geochemical model considers equilibrium dissolution and precipitation processes (as a consequence of the slow diffusive transport). C-S-H is modelled using the CSHQ solid solution model proposed by Kulik (2011). The porosity of each cell is calculated based on the solid volume and will evolve in time by the process of dissolution (portlandite, C-S-H) and precipitation (calcite).
- The transport of solution species is calculated for each component, at each time step, using LB multilevel method.
- The concept of pore size-controlled solubility (PCS) is used to limit mineral precipitation in narrow pores. This theory is based on the assumption that fine pores are able to maintain higher concentrations of species in comparison to larger pores. A target saturation index could be higher than 0 in cells with smaller pore radius, which implies that precipitation is prohibited within cells with fine pores.

The pore radius within each cell can be determined by the cell porosity, number of pores and the length of pores. In the current study, except that porosity keeps changing during leaching and precipitation, the other two parameters remain constant in the PCS model: 5E7 for number of pores and 0.01 μm for the length of pores. Sensitivity analysis will be done in the future to test their impact on the precipitation behavior.

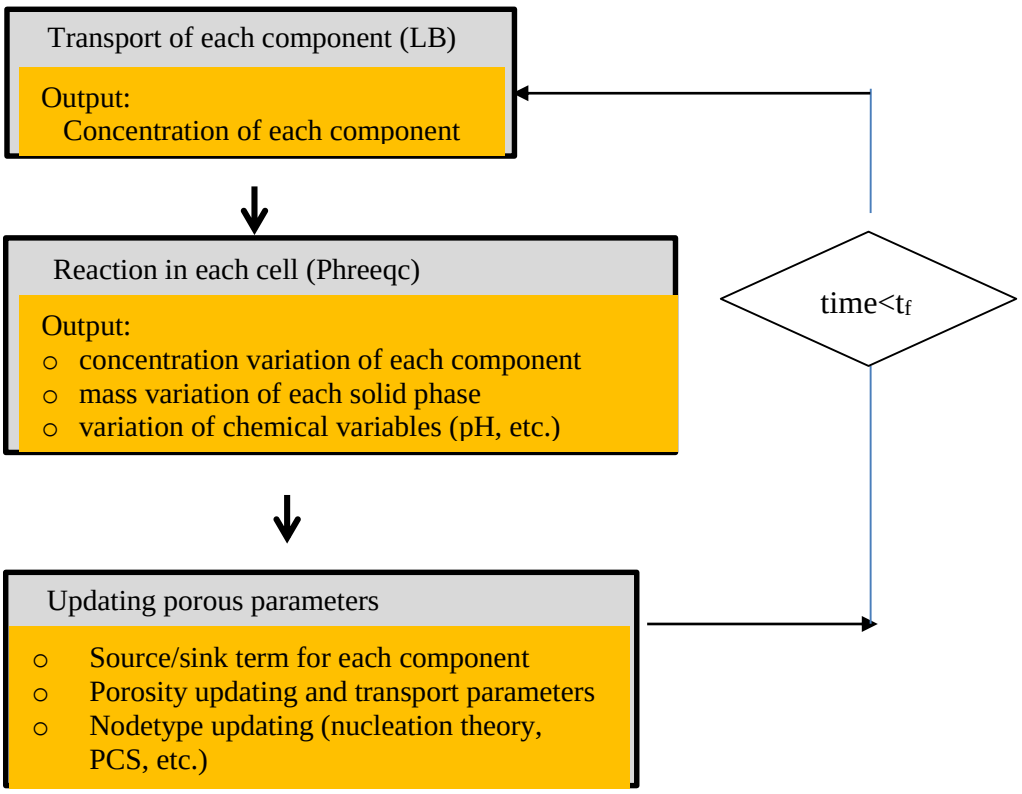

Figure 11.1. *Flow chart of the reactive transport model.*

11.2 TOOL DEVELOPMENT – ACCELERATED PROCEDURE FOR MODELLING DISSOLUTION AT THE PORE SCALE

Introduction

When modelling complex problems such as leaching of cement systems, numerical models face practical limitations linked to computational resources. In recent years, pore-scale approaches became an attractive method to simulate durability (Patel et al., 2018). However, in order to capture the critical features at that scale, such as the presence of capillary pores or heterogeneity in mineral phases, geometric information with high resolution is needed in a sufficiently large volume to ensure a representative elementary volume (REV). This leads to a very high number of unknowns with substantial memory and computational costs, especially in three-dimensional simulations. Moreover, in diffusion-controlled systems any numerical method should obey Von Neumann criteria to correctly assess the chemical degradation. This inevitably leads to a huge amount of time steps and cannot be treated with parallelization of computational processes. In this work, we present a new approach, which allows for considerable accelerations of the simulation of the chemical evolution of cementitious systems. The idea is that the number of iterations can be reduced if the chemical buffering is sufficient to bring transport to a steady state. If this condition is satisfied, then it is possible to reduce physical (and thus also computational) time by adjusting the chemical system appropriately. The analysis shows that the pore structure resulting from the dissolution process remains invariant with respect to certain ratio between solid and equilibrium concentration.

Theoretical background

Consider a chemical system which involves a dissolution of solid. For the purpose of presentation, we define the concentration in solid C_{solid} and the equilibrium concentration C_{eq} in solute. We further assume that diffusive transport defines the rate of dissolution. When solid mass at the solid surface decreases below the equilibrium concentration, this solid becomes liquid and solid geometry changes. Every time the geometry changes, there is some time required to establish new equilibrium. We can distinguish between two different situations depicted in Figure 11.2. The situation (a) represents the system when the geometry changes before the transport equilibrium is established (i.e. when the diffusion process is in steady state). This means that fluxes at time t_1 and time t_2 ($t_2 > t_1$) are not the same. In other words, this system is not buffered enough to be accelerated. On the other hand, Figure 11.2b represents the situation where there is a steady state at t_3 achieved without the change of geometry. After certain time (denoted as time t_3 in Figure 11.2 (right)) the concentration field (and hence flux) remains constant until the geometry changes (t_4). The time between t_4 and t_3 is the time which could be accelerated.

In order to determine whether the buffering is sufficient or not, we define the reference distance between the boundaries between two solids (or between a solid and the boundary as shown in Figure 11.2. The time during which the aqueous solution is close to a steady state can be determined from the amount of mass which is distributed within the length L, the so-called length patch or root-mean-square displacement [L]. For pure diffusion processes, the amount of mass that is distributed within the interval L at time t can be expressed in terms of the standard deviation of mass in the domain $\sigma = 2\,D\,t$. The length of mass patch at time t is then defined by the confidence interval $\psi \times \sigma$ or

$$L = \psi\sqrt{2Dt} \tag{11.2}$$

where ψ is an arbitrary constant defining how many σ of mass is in the patch of length L and D is the diffusion coefficient.

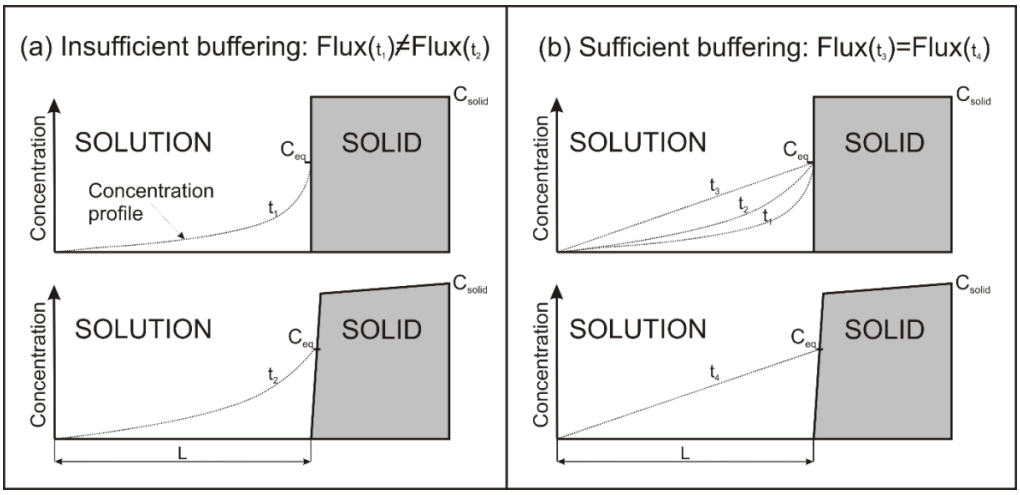

Figure 11.2. *Graphical representation of insufficiently and sufficiently buffered systems.*

At time *t* the concentration is distributed as a function of the distance from the solid as

$$C(x,t) = C_{eq}\left[1 - erf\,\frac{x}{\sqrt{4Dt}}\right] \tag{11.3}$$

From these two relations we can define the minimal time until the steady state is achieved. Further derivation (Perko and Jacques, 2019) leads to a final dimensionless number, which we call *Buffering number*, denoted as *Bu* number. *Bu* number is obtained in a simple form in eq. (11.4)

$$Bu = \frac{V_{total} \times C_{eq}}{V_{solid} \times C_{solid}} \tag{11.4}$$

where V_{total} and V_{solid} are a total volume and volume of solid, respectively. The volumes represent initial volumes in this case. The ratio between V_{total} and V_{solid} does not change considerably with time as long as REV is large enough (e.g. that the volume is large enough) because V_{total} also reduces with time in a completely leached domain. Hence, we assume that *Bu* number remains constant during calculations.

We demonstrated that the physical time, and thus the number of iterations, required to dissolve the solid can be scaled by *Bu*. For example, if time t_1 is required to fully dissolve a solid phase in a system with Bu_1 number, the time can be, according to equation (11.4), reduced by reducing either V_{solid}, C_{solid} or increasing C_{eq}. In a real chemical system, only V_{solid} can be changed. However, the intention of this numerical analysis is to leave the pore geometry (V_{solid}) intact and change either C_{solid} (concentration in solid) or C_{eq} in order to numerically accelerate dissolution. The time t_2 to dissolve the same volume of solid with other C_{solid} or C_{eq} (i.e. with other *Bu* number – Bu_2) would be

$$t_2 = t_1 \frac{Bu_1}{Bu_2} \tag{11.5}$$

Expanding this relation with equation (11.5) we get

$$t_2 = t_1 \frac{C_{eq,1} \times C_{solid,2}}{C_{eq,2} \times C_{solid,1}} \tag{11.6}$$

This means that in order to reduce the final time t_2 at given original solid concentration $C_{solid,1}$ and given equilibrium concentration $C_{eq,1}$, we can either decrease solid concentration $C_{solid,2}$ or increase the equilibrium concentration $C_{eq,1}$. The latter is typically done in accelerated experiments where the solubility is increased in order to accelerate the dissolution (Phung et al., 2015).

A cementitious system is a typical example of a system for which a significant numerical acceleration can be obtained; the ratios V_{solid}/V_{total} and C_{solid}/C_{eq} are high. Ca-leaching is a slow process which requires a lot of time steps to simulate. To illustrate the gain in a numerical application, we take an example from Seetharam et al. (2018), which describes leaching of a mortar. The model consists of random spherical particles (i.e. cement clinker particles) between two hypothetical aggregate surfaces, respecting initial water-to-cement (W/C) ratio of mortar as well as particle size distribution of the cement type. Particle size distribution represents CEM I 42.5 N cement with Blaine fineness of 430 m^2/kg with W/C=0.35. The size of the domain is 2.5×5×5 mm^3. Volume fraction of aggregates in the presented case is V_{agg}=0.2. Volume fraction of portlandite (CH) is V_{CH}=0.154 and of C-S-H V_{CSH}=0.476. The effective diffusion coefficient in cement paste is 2.22×10^{-12} m^2/s.

The initial *Bu* numbers for CH, Ca in C-S-H and Si in C-S-H are 1.05×10^{-2}, 6.63×10^{-3} and 1.73×10^{-5}, respectively. According to our previous discussion the acceleration of dissolution process can be at least 20-50 times without any visible difference in a dissolution front. The limiting phase is portlandite (CH) because *Bu* number is the highest. Other phases and species are even less limited and could be accelerated more than that.

With the acceleration method, the simulation was solved in a few hours, which is significantly faster than without acceleration. This enables analysis of larger systems or to perform a parameter sensitivity or uncertainty analysis in the same time. The figure below shows that the dissolution front (white represents portlandite) obtained with the proposed approach is virtually the same as a simulation without the acceleration and at 50 times accelerated system (right). To achieve this, we increased C_{eq} for 50 times (see Figure 11.3 (right)) with respect to the real equilibrium

concentration. For this particular example, we shortened the real calculation time from one month to less than half day on a desktop workstation.

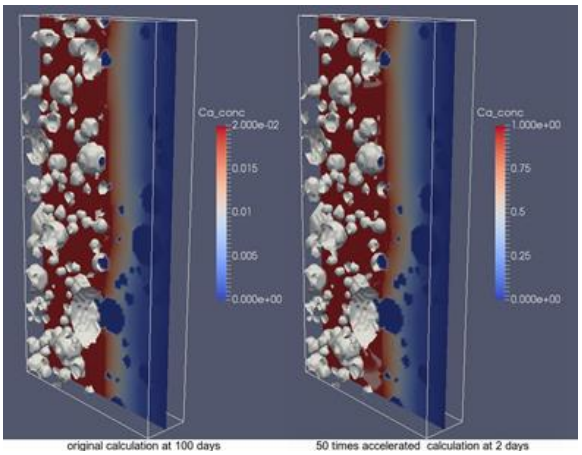

Figure 11.3. *Dissolution front in mortar at 100 days for the original system (left) and at 2 days for system with 50 times higher Bu number (right). Dissolved Ca concentration is given in mol/dm^3. Dark blue spots are aggregates (zero concentration).*

11.3 APPLICATION: 2D LEACHING OF CEMENT STRUCTURE IN CONTACT WITH $NaHCO_3$ WATER

The pore-scale model and the framework for coupled precipitation-dissolution reactions is applied on a 2D setup in which hardened cement paste is leached with $NaHCO_3$ water (a proxy for Boom Clay pore water). The discretization is chosen to be 1 μm, which is typical resolution of microstructure obtained from hydration models (e.g. CEMHYD3D or HYMOSTRUC). The computation of such a model is rather expensive not only because of the small discretization, but also due to the contrasting porosity among various cells, which determines a much smaller time step based on the minimum porosity in the domain in order not to violate the continuity of mass transfer. Therefore, simulation is currently carried on a relatively small 2D domain for the purpose of model testing—a square with a side length of 40 μm.

The initial microstructure is established from a SEM image of a real cement paste (W/C ratio of 0.425) (left of Figure 11.4), from which a random 2D section of 40 μm and 40 μm is taken out for carrying out the simulation (right of Figure 11.4). Volumetric fraction of clinker, portlandite, C-S-H and capillary pores are 0.3%, 14.8%, 66% and 18.9%, respectively. Because initial porosities for C-S-H and portlandite cells are required when using multilevel LB method, portlandite is assumed to have a negligible porosity of 4% at the beginning which corresponds to a solid mass of 29 mol/L. The initial solid mass of CSHQ_TobH, CSHQ_TobD, CSHQ_JenH, CSHQ_Jen are considered 0.1041, 2.5050, 2.1555, 3.2623 mol/L, resulting in an initial porosity of 44.8% in C-S-H cells.

The $NaHCO_3$ water diffused into the cement from the left, imposing a constant concentration boundary ($[Na^+]$ =15 mM, $[Ca^{2+}]$ =1 mM, $[Si^+]$ = 0.001 mM and a CO_2 partial pressure of $10^{-2.62}$ atm). The rest boundaries are no flux boundaries. Initially, the solution in the capillary pores and C-S-H cells are equilibrated with C-S-H, and the solution in portlandite cells are equilibrated with portlandite. The other parameters used in the simulation include the free liquid diffusion coefficient D_0: 1E-9 m^2/s and tortuosity: 1.0.

Several observation cells are selected along the mid horizontal line (at Y=20 μm in Figure 11.4) from left boundary towards the inside, where cells (Y μm, X μm) = [20,1], [20,2], [20,3] and [20,4] are initial C-S-H cells and cell [20,5] is an initial portlandite cell. Precipitation of calcite happens

progressively inwards, as shown in Figure 11.5. With dissolution and precipitation coexisting within these cells, the evolution of porosity shows up- and down-trend in Figure 11.5.

Ion concentrations and pH fields at 10 seconds are shown in Figure 11.6. The average porosity over the whole domain increases with time and its evolution is presented in Figure 11.7. Evolution of the mass of various solids averaged in the whole domain are presented in Figure 11.8.

The portlandite, calcite and total C-S-H in the domain after 10s are shown in Figure 11.9. By then, calcite has precipitated in one third of the whole domain and 40% of the initial portlandite cells are completely dissolved.

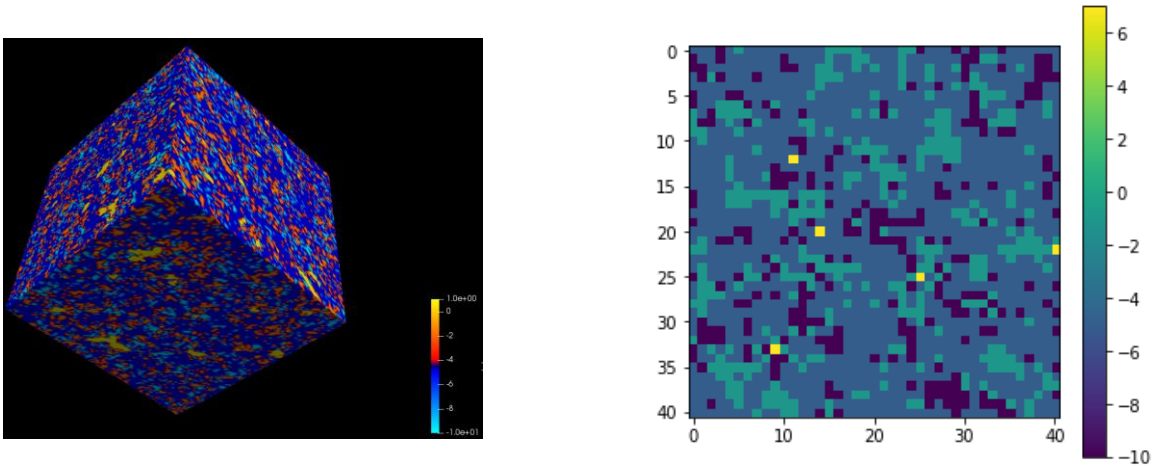

Figure 11.4. *(left) microstructure from SEM image of the cement paste (right) a random 2D section taken from the microstructure – color scale represents nodetype (dark blue: portlandite; navy blue: CSH; green: capillary pores; yellow: non-diffusive solid particles). X and Y distances are in µm.*

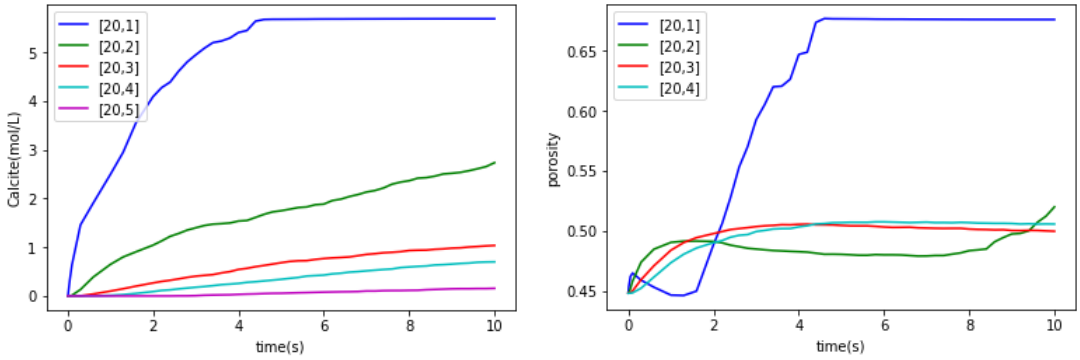

Figure 11.5. *(left) Evolution of precipitated calcite; (right) evolution of porosity of a C-S-H cell.*

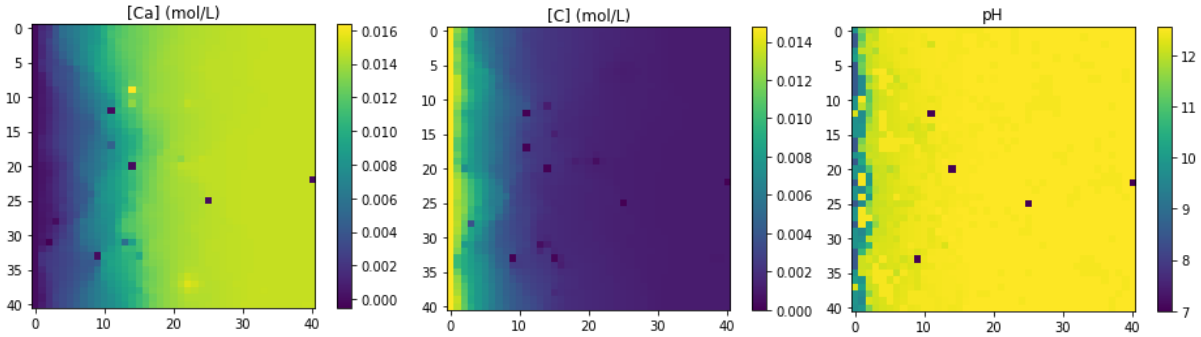

Figure 11.6. *Concentration field of Ca and Na and pH field after 10s.*

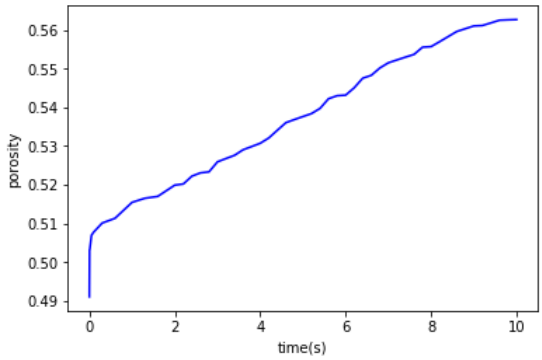

Figure 11.7. *Evolution of porosity averaged in the whole domain.*

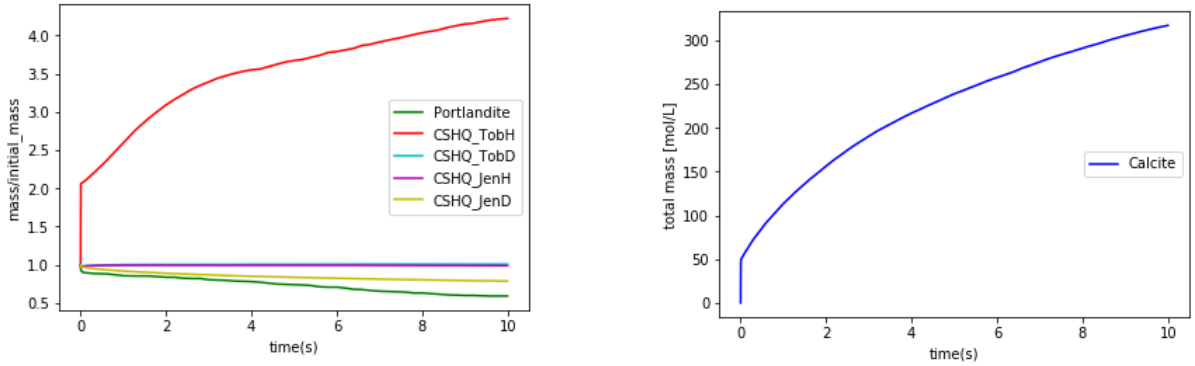

Figure 11.8. *Evolution of total solid mass in the whole domain.*

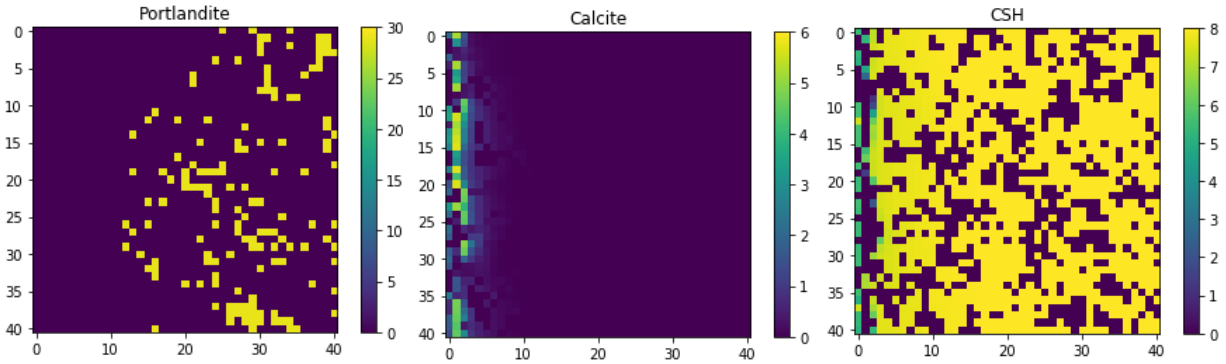

Figure 11.9. *Portlandite, calcite and total C-S-H in the domain after 10s (unit: mol/L).*

11.4 OBTAINING EFFECTIVE DIFFUSIVITY FOR CONCRETE AND CLAY FROM MICROSTRUCTURES

Diffusivity is an important parameter in practical applications. Unlike macroscopic analyses, where tortuosity of a porous media is considered using empirical functions, simulations at micro scale consider the real morphology of the material and therefore is believed to have great potential for estimation of transport parameters.

The first step for obtaining effective diffusivity at micro scale is to establish the microstructure of the material. In this work, the microstructures for two types material: concrete and the Boom Clay, are established on FIB-SEM image with length of 5 μm and resolution of 5 nm. The sample is taken at the URF HADES (Belgium, Boom Clay, WP1, Phung et al. 2017) after a contact time of about 14 years. A smaller cube with a length of L=1 μm (200 cells per side), is randomly selected from the microstructure and used for computing effective diffusivity. Considering that the objective in

this work focus on the demonstration of the capability of the method to estimate the effective diffusivity, and in order to ease the calculation, the selected cube is relatively small and does is not a representative element of the actual material. In the future, sufficient simulations over a larger domain abstracted at more random positions should be carried out to fulfill the upscaling requirements.

The effective diffusivity is obtained subsequently by solving the diffusion problem using the LB scheme with D3Q7 lattice and linear equilibrium distribution function (EDF). Effective diffusivity along a certain direction can be obtained by applying a fixed concentration gradient over the domain. Taking x direction for instance:

$$D_e/D_0 = F_x/\nabla c \tag{11.7}$$

where F_x is the average flux in x direction at steady state; ∇c is the concentration gradient applied at left and right boundaries and equal to 1/L; D_0 is the molecular diffusion coefficient in pure water.

For the concrete, C-S-H, capillary pores and non-diffusive solid particles are explicitly resolved, while in the Boom Clay only pores and solid particles are explicitly resolved. No matter what type of material, the methodology used to estimate the diffusivity is similar. Pores are pure liquid phase and solid particles are impermeable which serve as bouncing back boundaries in the LB method. The only difference between these two materials in the simulation is the extra treatment of C-S-H in concrete, which is porous and with a diffusivity predetermined based on two-phase theory (Patel, 2016). Assuming water cement ratio of 0.425 and degree of hydration of 0.83, the porosity of C-S-H is calculated to be around 0.34 and the effective diffusivity of C-S-H is $0.002D_0$ (D_0 is the molecular diffusion coefficient in pure water with unit of m^2/s).

Microstructural profiles of concrete in three directions through the centroid of cube are shown in Figure 11.10, among them, 8.3% are capillary pores, 3.4% impermeable particles and the rest 88.2% C-S-H phases.

The cubic microstructure of the Boom Clay under consideration reveals a porosity 0.108. Profiles of the Boom Clay in three directions through the centroid of cube are shown in Figure 11.11.

A relative effective diffusivity of 0.0040 is obtained for the Boom Clay in x direction and 0.0035 for concrete. Compared to measured diffusion values on the sample, the predictions are lower for Boom Clay (measured 0.0066 D_0 = 4.76E-11 m^2/s) and close for cement/concrete (measured $0.0032D_0$ = 2.30E-11 m^2/s) (measured with dissolved He gas, WP1, Gaboreau et al. in press).

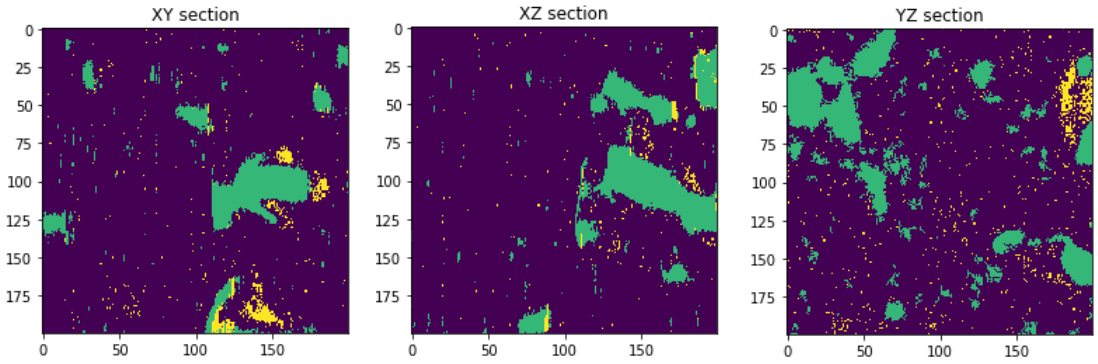

Yellow: non-diffusive particles; blue: C-S-H; green: capillary pores

Figure 11.10. *Profiles of concrete in three directions through the centroid of cube.*

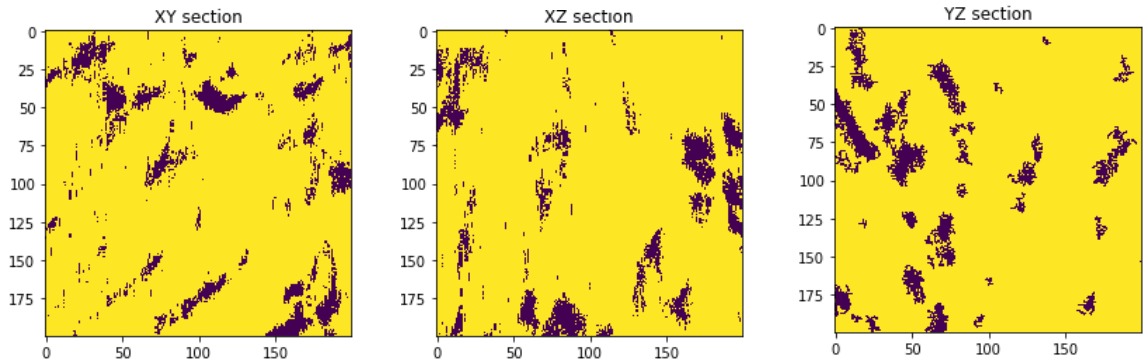

Yellow: Non-diffusive particles; blue: pores

Figure 11.11. *Profiles of the Boom Clay in three directions the centroid of cube.*

11.5 TRACING VARIATION OF CONCRETE DIFFUSIVITY DURING DISSOLUTION-PRECIPITATION

At regular time steps during the simulation, the complete microstructure of the evolved cement paste is saved, which will be used for estimation of effective diffusivity. Variation of diffusivity with time can be used to investigate how the dissolution and precipitation processes influence the macroscopic properties of the cement. We use the Yantra multilevel module for this purpose.

Applying a fixed concentration gradient over the domain along a certain direction, effective diffusivity can therefore be obtained when the flux reaches steady state. Solid particles such as clinker serve as internal bounce back boundaries. Leached portlandite and C-S-H as well as precipitated calcite are viewed as porous media with lowered diffusivity determined by porosity and tortuosity. The trickiest part is how to determine the effective diffusivity of a composite cell, such as a cell with calcite and C-S-H coexisting. Currently, accurate estimation of the effective diffusion is not possible, but qualitative variation of effective diffusion with leaching and precipitation process can be obtained.

With time, dissolution of C-S-H and portlandite as well as precipitation of calcite start from the left boundary. Variation of the effective diffusivity of the cement paste with time is presented in Figure 11.12. The dramatic variations of De at the beginning should be improved in the future by including chemical reactions occurring in pure liquid cells even there is no potential occurrence of precipitation.

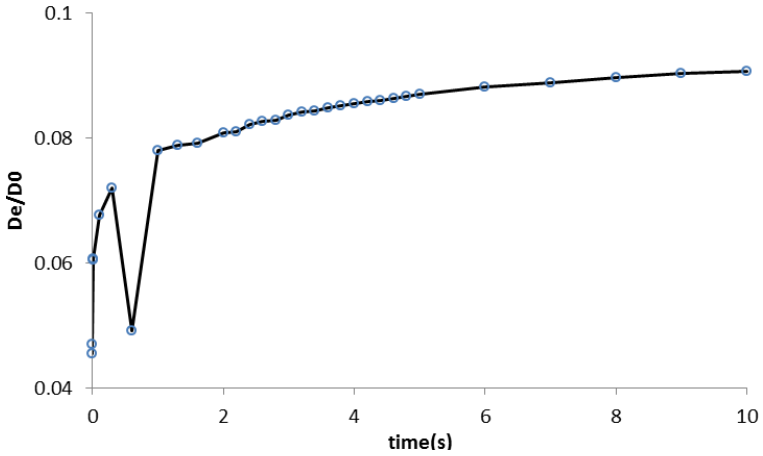

Figure 11.12. *Variation of the effective diffusivity of the cement paste with time.*

11.6 CONCLUSIONS AND MAIN OUTCOMES

The modelling approach introduced in this report exhibits its capability to qualitatively investigate the dissolution-precipitation processes within hardened cement paste through a pore-scale and multilevel system. Schemes including the transport through multilevel scale and pore size-controlled solubility can effectively avoid the precipitation blocking transport. Furthermore, it allows for estimating the change in effective diffusivity when a hardened cement paste undergoes degradation. As such, it can provide macroscopic transport parameters to continuum modelling. However, the computation for LB multilevel method coupling with external geochemical reaction tool (Phreeqc) is quite expensive. Acceleration methods which can significantly enhance the simulation speed need to be found in future research. Furthermore, more appropriate conceptual model regarding nucleation theory and determination of effective diffusion coefficient in composite cells (various solid phases co-existing) need to be worked out.

Acknowledgements

The research leading to these results has received funding from the European Union's Horizon 2020 Research and Training Programme of the European Atomic Energy Community (EURATOM) (H2020-NFRP-2014/2015) under grant agreement n° 662147 (CEBAMA).

11.7 REFERENCES

Kulik, D.A. (2011). Improving the structured consistency of C-S-H solid solution thermodynamic models. Cement and concrete Research, 47, 477-495.

Patel, R.A. (2016). Lattice Boltzmann Method Based Framework for Simulating Physico-chemical Processes in Heterogeneous Porous Media and Its Application to Cement Paste. PhD thesis, Belgium, Ghent University.

Patel, R.A., Perko, J., Jacques, D., Schutter, G.D., Ye, G., Breugel, K.V. (2018). A three-dimensional lattice Boltzmann method based reactive transport model to simulate changes in cement paste microstructure due to calcium leaching. Constr. & Building Mat., 166, 158–170.

Perko, J., Jacques, D. (2019). Numerically accelerated pore-scale equilibrium dissolution. Journal of Contaminant Hydrology, 220, 119-127.

Phung QT, Maes N, Jacques D, De Schutter G, Ye G. (2015). Investigation of the changes in microstructure and transport properties of leached cement pastes accounting for mix composition. Cement and Concrete Research, 79, 217-234.

Phung QT, Maes N, Claret F, Gaboreau S, Leysen J. (2017). Methodology to study the changes in microstructure and transport properties of the Boom Clay - concrete interface. 1st Annual CEBAMA Workshop Proc. Barcelona, Spain: KIT Scientific Publishing; p. 37-48.

Gaboreau S, Phung QT, Maes N, Claret F. Experimental study of the chemical degradation of cementitious materials in Boom Clay environment. 3rd Annual CEBAMA Workshop Proc. KIT Scientific Publishing; in press.

Seetharam, S., Patel, R.A., Perko, J., Jacques, D. (2018). Quantification of leaching kinetics in OPC mortars via a mesoscale model. Construction & Building Materials, 180, 614-628.

14 UDC/ J. Samper, A. Mon, L. Montenegro, A. Naves, J. Fernández (UDC), J. Cuevas, R. Fernández (UAM), M.J. Turrero, E. Torres (CIEMAT)

Abstract

We present coupled thermo-hydro-chemical-mechanical (THCM) models of a set of heating and hydration tests (HB1 to HB6) performed by Ciemat and UAM within the CEBAMA project on columns containing OPC concrete samples in contact with compacted FEBEX bentonite. The tests lasted from 0.5 (HB1) to 11 (HB6) years. These tests provide unique data on the interactions of concrete and bentonite under deep geological repository conditions of high-level radioactive waste (HLW) and potential changes in bentonite and concrete properties. These tests were performed on columns heated at 100ºC at the bottom and hydrated at the top. The numerical models reproduce the general trends of the measured water content, porosity and temperature data and the experimental observations of mineral dissolution/precipitation. A sensitivity analysis of the model results of one of these column tests (HB4) has been performed to evaluate the relevance of the temperature gradient, the uncertainties in the mineral kinetic parameters, and the finite element grid size.

14.1 INTRODUCTION

The main objectives of UDC contribution to the CEBAMA project were: 1) improving THCM codes and models for the interactions of concrete and bentonite; 2) performing THCM models of the heating and hydration HB column tests (Turrero et al., 2011; Torres et al., 2013); 3) performing long-term predictions of the interactions of bentonite, concrete and clay rock; and 4) contributing to the analysis of time scaling issues. The geochemical evolution of the bentonite barrier during the initial stages of the hydration and heating of the repository depends on the thermal, hydrodynamic and mechanical processes. Thus, numerical models coupling THCM processes are required. Here we present the coupled THCM models of the entire set of tests including HB1, HB2, HB3, HB4, HB5, and HB6 tests (Turrero et al., 2011; Torres et al., 2013). In addition, we also report a detailed sensitivity analysis of the model results of the HB4 column test. The sensitivity runs include: 1) isothermal versus non-isothermal conditions; 2) the relevance of changes in the specific surfaces of kinetically-controlled minerals; and 3) the relevance of the finite element grid size. The models were solved with the UDC code INVERSE-FADES-CORE. The first version of INVERSE-FADES-CORE was developed within the FEBEX I project and was later improved within the FEBEX II, NFPRO, and PEBS projects (Zheng et al., 2010; Samper et al., 2013; Mon, 2017).

14.2 DESCRIPTION OF THE MODELLING WORK

Several tests were performed to study the interactions of concrete and bentonite pore water at the conditions prevailing in the EBS during the early hydration stage (Turrero et al., 2011; Torres et al., 2013). The tests, denoted as HB ("*Hormigón-Bentonita*"), were performed on medium-size cells containing a 7.15 cm thick bentonite sample in contact with a 3 cm thick concrete sample. The concrete was made of sulphate-resistant ordinary Portland cement (CEM I-SR) following the mix by CSIC-IETcc (Consejo Superior de Investigaciones Científicas- Instituto de Ciencias de la Construcción Eduardo Torroja): 400 kg of CEM I-SR cement, 911 kg of sand (0-5 mm), and 946 kg of aggregates (6-16 mm) with a w/c ratio of 0.45. The cells were hydrated at a constant pressure and at a temperature of 25ºC at the top of the cell through the concrete, while the temperature was maintained constant at 100ºC at the bottom of the cell (Figure 14.1).

The HB column tests provide data on the concrete and bentonite interface at several times. They were dismantled after 6, 12, 18, 54, and 80 months for the HB1 to the HB5 tests and 104 months for the HB6 test, which was dismantled within the CEBAMA project. However, the experimental data from HB5 and HB6 tests were not available for model testing. The initial porosity of the bentonite

is 0.4 and the initial water content is 13.3%, which corresponds to a saturation of 57% and a suction of $1.27 \cdot 10^8$ Pa (Samper et al., 2018). The cells were hydrated with a synthetic Spanish Reference Clay porewater (Turrero et al., 2011; Torres et al., 2013).

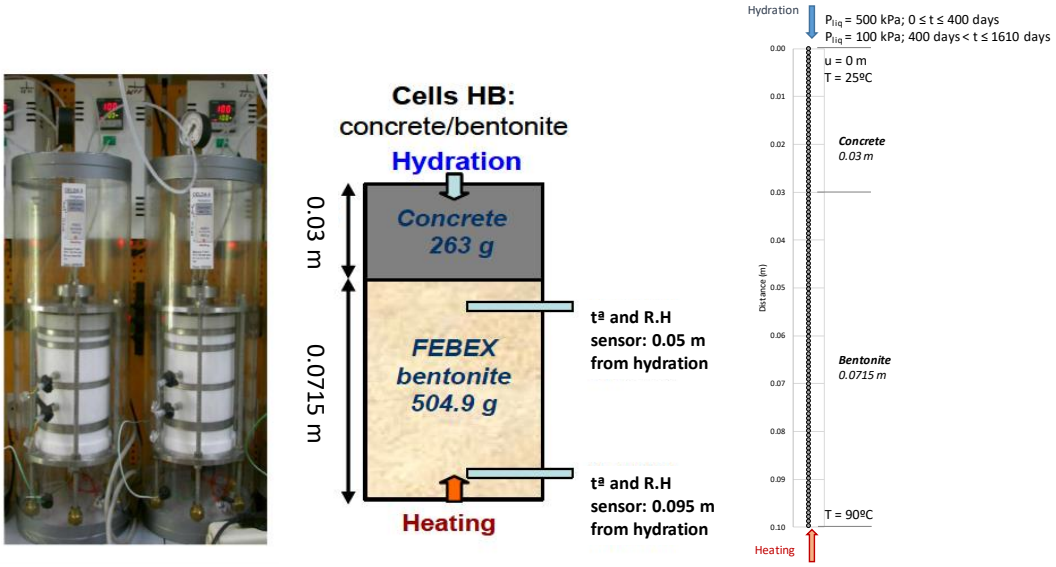

Figure 14.1: *Setup of the concrete-bentonite HB column tests (Turrero et al., 2011) (left) and finite element mesh and boundary conditions for the numerical model (Samper et al., 2018) (right).*

HB1 to HB6 tests were modelled with a 1D grid (see Figure 14.1) by assuming that the main direction of the water flow, heat transfer and solute transport is parallel to the axis of the column. Grid size is uniform and equal to 0.9 mm. The model domain includes the concrete ($0 < x < 3$ cm) and the compacted bentonite (3 cm $< x < 10.15$ cm). Bentonite and concrete parameters were taken from the model of the HB4 test in Samper et al. (2013; 2018). The concrete has a porosity of 0.125 and a gravimetric water content of 2.2%. The initial temperature is 22ºC along the cell. The prescribed temperature at the bottom of the column, where the heater is located, is 90 °C. This temperature is lower than the heater temperature due to lateral heat losses. Similar to previous THCM models of the FEBEX bentonite (Zheng et al., 2010; 2011), the initial total stress was assumed uniform, isotropic and equal to 250 kPa. The liquid pressure in the injection tank was initially equal to 500 kPa. It decreased after 400 days due to problems in the water injection system. The liquid pressure at the injection boundary was assumed equal to 500 kPa for $t < 400$ days and 100 kPa afterwards.

The initial composition of the OPC concrete porewater was calculated from speciation runs performed with EQ3/6 (Wolery, 1992) by assuming that the concentration of dissolved Ca^{2+} is controlled by local chemical equilibrium with respect to portlandite, HCO_3^- concentration is at equilibrium with respect to calcite, Mg^{2+} concentration is derived from the equilibration with brucite, Al^{3+} is at equilibrium with ettringite and SiO_2(aq) is controlled by equilibrium with respect to C1.8SH. The initial mineral volume fractions in the concrete are: 7.4% for portlandite, 2.2% for ettringite, 14.6% for C1.8SH, 1% for brucite, 0.1% for calcite and 62.2% for quartz. Quartz is assumed to be nonreactive. The initial pore water composition of the FEBEX bentonite was taken from Fernández et al. (2004). The initial mineral volume fractions of reactive minerals in the bentonite are: 0.36% for calcite, 0.08% for gypsum and 1.192% for cristobalite. The smectite was assumed to be not reactive. The model allows for the precipitation of the following secondary minerals: sepiolite, C0.8SH, anorthite and anhydrite. The dissolution/precipitation of portlandite, ettringite, C1.8SH, C0.8SH, quartz and cristobalite was simulated with the kinetic rate laws of Fernández et al. (2009). The specific surfaces of portlandite, ettringite, C1.8SH and C0.8SH were calibrated to reproduce the experimental mineralogical observations. The injection water is a

synthetic Spanish Reference Clay porewater (Turrero et al., 2011). Cation exchange and proton surface complexation reactions are assumed to take place only in the bentonite. The current model accounts for the changes in porosity caused by solid deformation and swelling but disregards the changes in porosity due to mineral dissolution/precipitation because the mechanical changes in porosity for bentonite are generally larger than the chemical changes in porosity. More details can be found in Mon (2017) and Samper et al. (2018).

14.3 MODEL RESULTS

Thermal and hydrodynamic results

The concrete is fully saturated after 7 days of heating and hydration and then, the bentonite hydrates at a very low rate through the concrete. Water content increases near the concrete and decreases near the heater due to the evaporation. Porosity increases in the bentonite near the concrete interface due to bentonite swelling. The results of the HB1 to HB6 column tests are similar because the water intake is fast in the first months and slows down after 10 months. The computed water content and porosity reproduce the general trends of the measured data at the end of the HB1 to HB6 tests (Figure 14.2).

Chemical results

Figure 14.3 shows the computed pH and the mineral volume fractions for the HB1 to HB6 tests. The penetration of the pH front into the bentonite increases with time. The high pH plume (pH > 8.5) penetrates 0.23, 0.32, 1.04, 5.8 and 6.7 cm into the bentonite at the end of the HB1, HB2, HB3, HB4, HB5 and HB6 tests, respectively. The diffusion of the alkaline plume is retarded by the precipitation of brucite in the concrete and calcite and sepiolite in the bentonite. The final pH in the concrete near the hydration boundary (x=0) is around 12.5 and in the bentonite near concrete/bentonite interface (x=0.03 m) is around 9.5 for the HB1, HB2 and HB3 and around 11 for the HB4, HB5 and HB6.

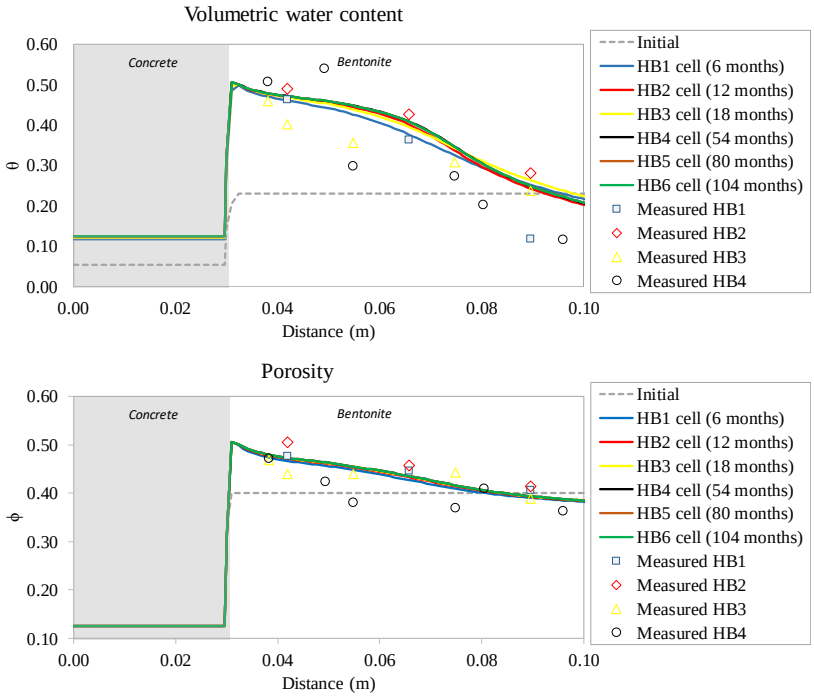

Figure 14.2: *Computed (lines) volumetric water content (up) and porosity (down) and measured data (symbols) for the HB1, HB2, HB3, HB4, HB5 and HB6 tests.*

Calcite is initially present in the concrete and in the bentonite. Calcite precipitates slightly in the concrete near the hydration zone because the concentration of dissolved Ca^{2+} in the hydration water is larger than that of the initial concrete porewater. Calcite precipitates at both sides of the concrete/bentonite interface, being larger in the concrete near the interface. The precipitation front of calcite penetrates 0.95 cm into the bentonite and 0.4 cm into the concrete after 104 months (Figure 14.4). The precipitation and dissolution front of calcite in the bentonite advances with time, the front in the HB6 test is the largest. Portlandite partially dissolves in the entire concrete domain, and especially near the concrete/bentonite interface (Figure 14.5). C1.8SH dissolves in the concrete, except near the hydration boundary where it precipitates because the SiO_2(aq) and Ca^{2+} concentrations in the boundary water are larger than those of the concrete porewater.

Brucite is initially present in the concrete. Brucite precipitates near the hydration boundary because the concentration of dissolved Mg^{2+} in the hydration water is larger than that of the initial concrete porewater. Brucite precipitates also in the concrete and bentonite near the interface. The maximum peaks of precipitation are located in the concrete. The front of brucite precipitation spreads 0.21 cm into the concrete and 0.8 cm into the bentonite after 104 months (Figure 14.4). Sepiolite precipitates in narrow bands at both sides of the concrete/bentonite interface for the HB1, HB2, HB3 and HB4. Later, sepiolite dissolves in the concrete and extends 0.48 and 0.8 cm in the bentonite for the HB5 and HB6 tests, respectively (Figure 14.5).

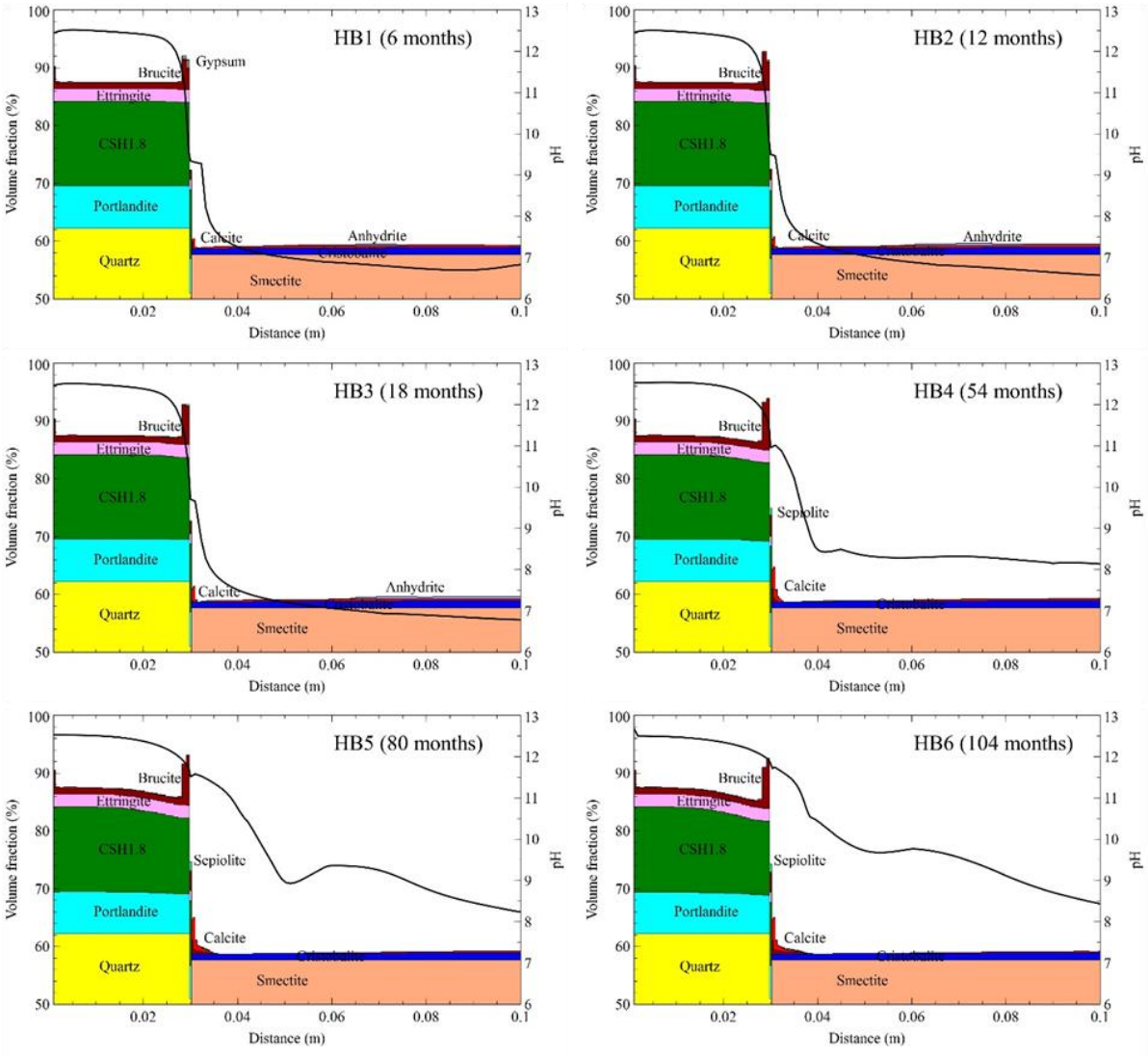

Figure 14.3: *Computed pH and mineral volume fractions for the HB1 to HB6 tests.*

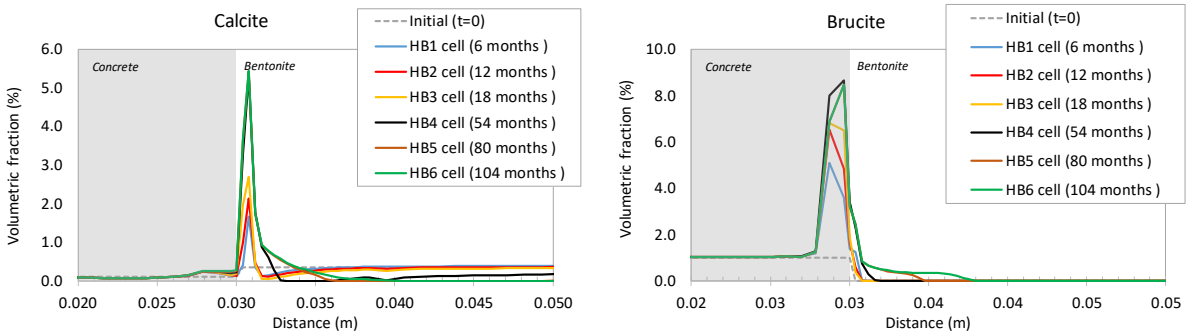

Figure 14.4: *Computed volume fraction of calcite (left) and brucite (right) for the HB1, HB2, HB3, HB4, HB5 and HB6 tests.*

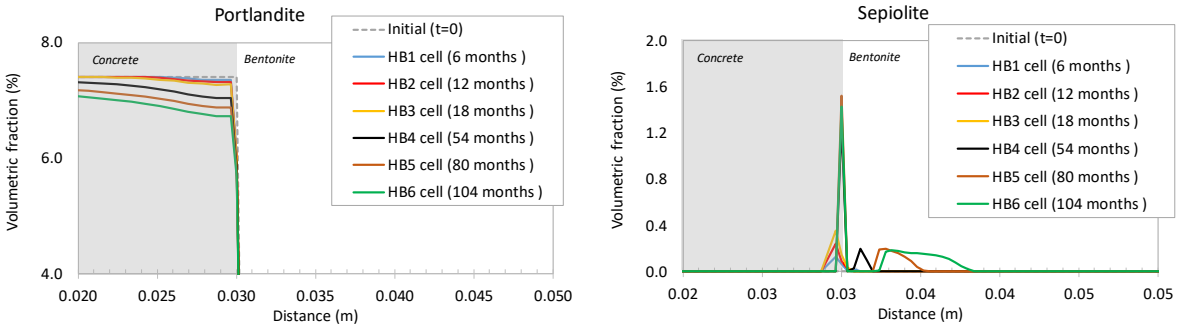

Figure 14.5: *Computed volume fraction of portlandite (left) and sepiolite (right) for the HB1, HB2, HB3, HB4, HB5 and HB6 tests.*

Gypsum dissolves initially because the initial bentonite water is not in equilibrium with gypsum. It precipitates in the bentonite near the concrete/bentonite interface in HB1 test and near the heater in the HB4 test. A precipitation front of anhydrite moving in the bentonite to the heater side is shown in the HB1, HB2 and HB3. Gypsum and anhydrite are not present at the end of the HB5 and HB6 tests. Cristobalite, quartz, CSH0.8, ettringite precipitation or dissolution are not relevant.

The main experimental observations on mineral phases at the end of the HB1, HB2, HB3 and HB4 tests (Turrero et al., 2011; Torres et al., 2013) are listed in Table 14.1. This table includes also a summary of the main trends of the computed mineral dissolution/precipitation for the HB1 to the HB6 tests.

A qualitative comparison of the computed values and the experimental mineral observations reveals that the numerical model captures the main trends of the experimental mineralogical observations including: 1) calcite and brucite precipitation in the concrete near the hydration boundary; 2) portlandite dissolution and calcite precipitation in the central zone of the concrete sample; 3) calcite and brucite precipitation in the concrete near the bentonite interface; 4) calcite and sepiolite precipitation in the bentonite near the concrete interface; and 5) calcite dissolution in the bentonite far from the concrete/bentonite interface. However, there are some discrepancies for ettringite and C-S-H precipitation. The numerical model predicts ettringite dissolution and a very small precipitation of C-S-H. Model discrepancies could be caused by uncertainties in: 1) the selection of the appropriate C-S-H, M-S-H and C-A-S-H phases; 2) the kinetic parameters (rate laws and specific surfaces); and 3) the selection of the appropriate secondary clay minerals.

The numerical model accounts for the changes in porosity caused by mechanical processes. The changes in porosity due to mineral dissolution/precipitation are not considered. The changes in porosity due to mineral dissolution/precipitation have been evaluated from the computed mineral volume fractions. Figure 14.6 shows the spatial distribution of the porosity at the end of the HB1, HB2, HB3, HB4, HB5 and HB6 tests. In general, the porosity decreases in the concrete/bentonite

interface and at the hydration boundary mainly due to brucite and calcite precipitation. The porosity at end of the longest HB6 test decreases 24% near the hydration zone due to brucite precipitation, increases about 10% in the interval 0.02 m < x < 0.029 m due to the simultaneous dissolution of C1.8SH, portlandite and ettringite dissolution and reduces about 40% in the concrete near the concrete/bentonite interface (in a 0.04 cm zone) due to brucite and calcite precipitation.

Table 14.1: *Qualitative comparison of the laboratory observations and model results for mineral dissolution/ precipitation.*

	HB1		HB2		HB3		HB4		HB5	HB6
	Laboratory observations	**Model results**	**Laboratory observations**	**Model results**	**Laboratory observations**	**Model results**	**Laboratory observations**	**Model results**	**Model results**	**Model results**
CONCRETE (hydration side)	**Portlandite** dissolution	√	**Portlandite** dissolution	√	**Portlandite** dissolution	√			**Portlandite** dissolution	**Portlandite** dissolution
	Calcite precipitation	√	**Calcite** precipitation	√	**Calcite** precipitation	√	**Calcite** precipitation	√	**Calcite** precipitation	**Calcite** precipitation
	Brucite precipitation	√	**Brucite** precipitation	√	**Brucite** precipitation	√	**Brucite** precipitation	√	**Brucite** precipitation	**Brucite** precipitation
CONCRETE (30 mm)	**Portlandite** precipitation	√	**Portlandite** precipitation	√	**Portlandite** precipitation	√	**Portlandite** dissolution	√	**Portlandite** dissolution	**Portlandite** dissolution
		√	**Calcite** precipitation in concrete	√	**Calcite** precipitation in concrete	√	**Calcite** precipitation in concrete	√	**Calcite** precipitation in concrete	**Calcite** precipitation in concrete
	CSH gels precipitation	~	**CSH gels** precipitation	~	**CSH gels** precipitation	~	**CSH gels** precipitation	~	**Some CSH** precipitation	**Some CSH** precipitation
	Quartz precipitation	*N*	**Quartz** precipitation	*N*	**Quartz** precipitation	*N*				
	MSH precipitation	√	**MSH** precipitation	√	**MSH** precipitation	√				
							Ettringite precipitation	*N*	**No Ettringite** precipitation	**No Ettringite** precipitation
					Gypsum and **thaumasite** precipitation	√				
	Zeolites precipitation	Not considered	**Halite and K-feldspar** precipitation	Not considered	**Vaterite** and **aragonite** precipitation	Not considered				
CONCRETE/ BENTONITE INTERFACE (some mm)	**Brucite** precipitation	√	**Brucite** precipitation	√	**Brucite** precipitation	√	**MSH** precipitation	√	**MSH** precipitation	**MSH** precipitation
	Portlandite precipitation	*N*	**Portlandite** precipitation	*N*	**Portlandite** precipitation	*N*				
	Calcite precipitation	√	**Calcite** precipitation	√	**Calcite** precipitation	√	**Calcite** precipitation	√	**Calcite** precipitation	**Calcite** precipitation
	CSH gels (tobermorite and jennite type) precipitation	*N*	**CSH gels (tobermorite and jennite type)** precipitation	*N*	**CSH gels (tobermorite and jennite type)** precipitation	*N*	**CSH gels (0.8)** precipitation	*N*	**No CSH** precipitation	**No CSH** precipitation
			Ettringite precipitation	*N*	**Ettringite** precipitation	*N*	**No Ettringite** precipitation	√	**No Ettringite** precipitation	**No Ettringite** precipitation
			Gypsum precipitation	√	**Gypsum** precipitation	√				
					Quartz dissolution	√				
	Smectite alteration not observed	Not considered	**Smectite alteration** (brucite saponite-smectite mixed phase")	Not considered	**Smectite alteration** (brucite saponite-smectite mixed phase")	Not considered Not considered				
					Saponite formation				**Brucite** precipitation	**Brucite** precipitation
BENTONITE	Unaltered bentonite mineralogy	~	Unaltered bentonite mineralogy	~	Unaltered bentonite mineralogy	~	**Calcite** dissolution	√		
							Gypsum and **chloride** precipitation	√		

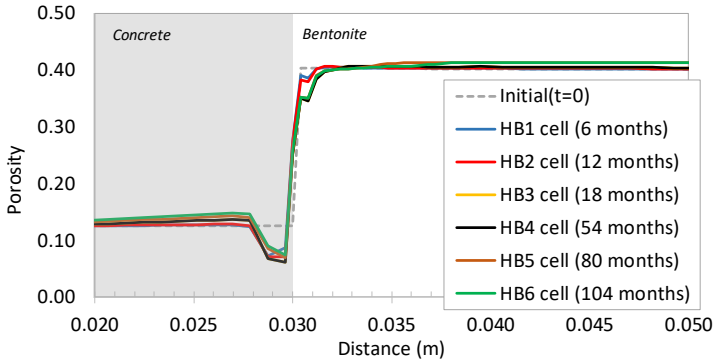

Figure 14.6: *Porosity for the HB1 to HB6 tests. Changes in porosity are computed from mineral volume fractions.*

14.4 SENSITIVITY ANALYSIS OF THE MODEL OF THE HB4 TEST

Sensitivity analysis to the thermal field

The base run of the HB4 column test is non-isothermal. The temperature of the hydration water is 25ºC. The prescribed temperature at the bottom of the column, where the heater is located, is 90 °C. This temperature is lower than the heater temperature due to lateral heat losses. A sensitivity run was performed at a constant and uniform temperature of 25ºC. Figure 14.7 shows the computed cumulative precipitation of calcite and brucite for the base and sensitivity runs. The model results for constant temperature show significant differences in the precipitation of calcite and brucite. The peaks of brucite and calcite precipitation for constant temperature are smaller than those of the base run. Moreover, the thickness of the bentonite zone where calcite and brucite precipitate in the constant temperature run is larger than that of the base run. Brucite precipitates in the concrete and in the bentonite in the base run, while it only precipitates in the bentonite in the constant temperature run.

The reduction in porosity in the concrete near the bentonite interface and in the bentonite in the constant temperature run is smaller than that of the base run (Figure 14.8). The differences in the computed mineral precipitation and porosity reduction between the isothermal and non-isothermal runs are mainly related to changes in the equilibrium constants which depend on temperature and water evaporation near the heater which is occurs only in the non-isothermal model run.

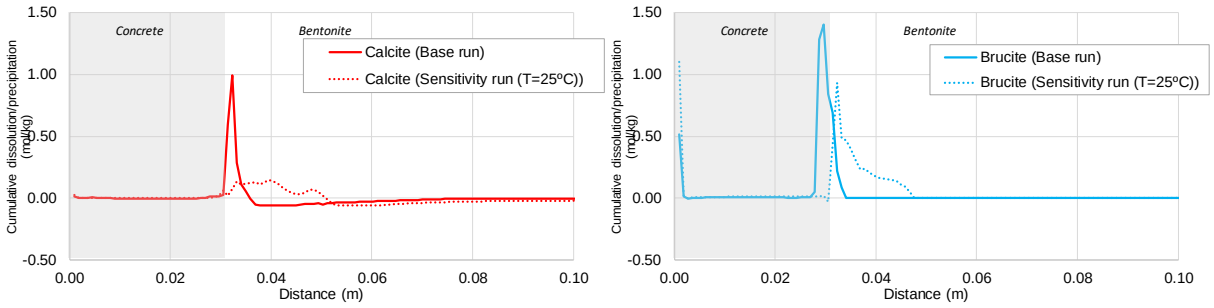

Figure 14.7: *Computed calcite (left) and brucite (right) precipitation/dissolution for the base and sensitivity runs with a uniform temperature (25ºC) for the model of the HB4 test.*

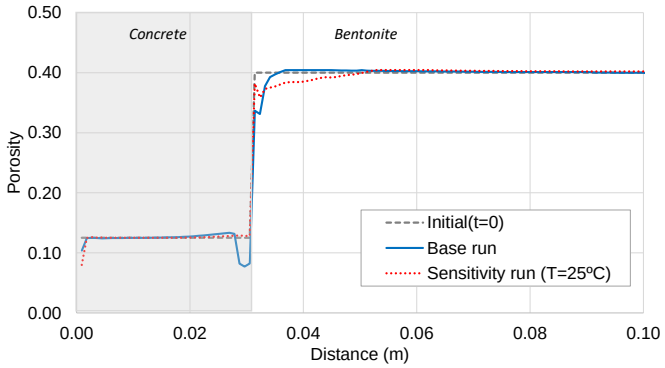

Figure 14.8: *Computed porosity for the base and sensitivity runs with uniform 25ºC temperature for the model of the HB4 test.*

Sensitivity analysis to the kinetic parameters and mineral phases

Sensitivity runs were performed to investigate the sensitivity of model results to changes in the specific surfaces of kinetically-controlled portlandite and ettringite. Model results are sensitive to an increase of the specific surface of portlandite by a factor of 2 and an increase of the specific surface of ettringite by a factor of 10 (Figure 14.9). The increase in the specific surface of portlandite leads to larger portlandite dissolution rates, larger calcite precipitation and larger pH in the bentonite. The increase of the specific surface of ettringite leads to more precipitation of ettringite in the mid upstream part of the concrete, more ettringite dissolution in the concrete near the bentonite interface and larger pH in the bentonite. On the other hand, the model lacks sensitivity to the kinetic Mg-saponite precipitation (Figure 14.9) which was simulated with the kinetic law reported by Mon et al. (2017).

Sensitivity analysis to grid size

Grid size in the reference model is uniform and equal to 0.9 mm. Several sensitivity runs were performed in which the grid was refined in a 3 cm wide band around the concrete/bentonite interface. Grid sizes of 0.45 mm, 0.18 mm and 0.1 mm were considered in three simulation runs while the size of the rest of the elements was equal to 0.45 mm. Mineral precipitation increases at both sides of the concrete/bentonite interface when the grid size is reduced (Figure 14.9). The calculated porosity in the concrete near the bentonite interface decreases drastically, reaching pore clogging for grid sizes smaller than 0.18 mm.

The numerical solution improves by decreasing the grid size because the discretization errors decrease when the grid size is decreased. Model results for the run with the smallest grid size should be considered the most realistic.

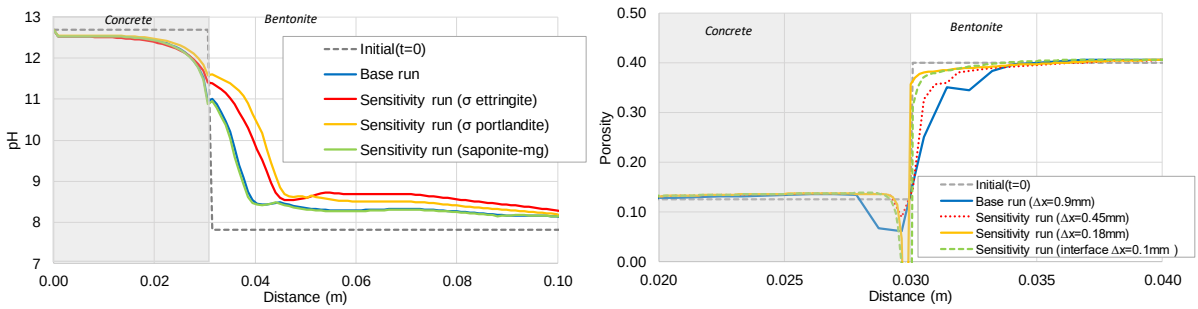

Figure 14.9: *Model of the HB4 test: Sensitivity of the computed pH to changes in the mineral parameters (left) and sensitivity of the computed porosity to changes in the grid size (right).*

14.5 CONCLUSIONS AND FUTURE WORK

Coupled THCM models of the HB1, HB2, HB3, HB4, HB5 and HB6 tests have been presented. Model results reproduce the general trends of the measured water content, porosity, and temperature (not shown here) and the observed patterns of mineral phases for the HB1 to HB4 tests. The predictions of the HB5 and HB6 tests show similar trends to those of the rest of the tests. These predictions will be compared to measured data when they become available.

The thickness of the bentonite zone where calcite and brucite precipitate in the constant temperature run is larger than that of the base run. While brucite precipitates in the concrete and in the bentonite in the base run, it precipitates only in the bentonite in the constant temperature run. The reduction in porosity in the concrete near the bentonite interface and in the bentonite in the constant temperature run is smaller than that of the base run. The results of the isothermal sensitivity run confirm the conclusions of Lalan et al. (2016) who concluded that the temperature plays an important role in the degradation of C-S-H and the precipitation of mineral phases. The intricate interplays of thermal and chemical processes in this complex chemical system prevent a simple explanation for the results of the sensitivity run to temperature.

Model results are sensitive to the increase of the specific surfaces of portlandite and ettringite. On the other hand, model results are not sensitive to kinetic Mg-saponite precipitation. Mineral precipitation increases at both sides of the concrete/bentonite interface when the grid size is reduced. The calculated porosity in the concrete near the bentonite interface decreases drastically, reaching pore clogging for grid sizes smaller than 0.18 mm.

It is planned to improve the THCM models of the HB column tests by: 1) considering additional C-S-H and M-S-H phases; 2) adjusting the kinetic parameters and 3) accounting for the feedback effect of the changes in porosity caused by mineral dissolution/precipitation.

Acknowledgements

The research leading to these results has received funding from the European Union's Horizon 2020 Research and Training Programme of the European Atomic Energy Community (EURATOM) (H2020-NFRP-2014/2015) under grant agreement n° 662147 (CEBAMA).

14.6 REFERENCES

Fernández A.M., Baeyens B., Bradbury M., Rivas P. (2004). Analysis of pore water chemical composition of a Spanish compacted bentonite used in an engineered barrier. Physics Chemistry of the Earth 29, 105-118.

Fernández R., Cuevas J., Mäder U. K., (2009). Modelling concrete interaction with a bentonite barrier. European Journal of Mineralogy 21, 177-191.

Lalan P., A. Dauzères, L. DeWindt, D. Bartier, J. Sammaljärvi, J.D. Barnichon, I. Techer, V. Detilleux (2016). Impact of a 70 °C temperature on an ordinary Portland cement paste/claystone interface: An in situ experiment. Cement and Concrete Research 83, 164-178.Mon A. (2017). Coupled thermo-hydro-chemical-mechanical models for the bentonite barrier in a radioactive waste repository. Ph.D. Dissertation. Universidad de A Coruña, Spain.

Mon, A., 2017. Coupled Thermo-hydro-chemical-mechanical Models for the Bentonite Barrier in a Radioactive Waste Repository. Ph. D. Dissertation. Universidad de A Coruña, Spain.

Mon A., Samper J., Montenegro L., Naves A., Fernández J. (2017). Long-term non-isothermal reactive transport model of compacted bentonite, concrete and corrosion products in a HLW repository in clay. Journal of Contaminant Hydrology, 197, 1-16.

Samper J., Mon A., Montenegro L., Pisani B. and Naves A. (2013). Report on testing multiple-continua THCM models with laboratory and large-scale tests. Deliverable 3.4-1 of the PEBS Project.

Samper, J., A. Mon, L. Montenegro, A. Naves, J Fernández, J. Cuevas, R. Fernández, M.J. Turrero, E. Torres (2017) Coupled THCm numerical models of heating and hydration tests to study the interactions of compacted FEBEX bentonite with OPC concrete. Proceedings of the First Annual Workshop of the HORIZON 2020 CEBAMA Project, M. Altmaier, V. Montoya, L. Duro, A.

Samper, J, A. Mon, L. Montenegro, J. Cuevas, M. J. Turrero, A. Naves, R. Fernández & E. Torres (2018). Coupled THCM model of a heating and hydration concrete-bentonite column test. Applied Geochemistry 94, 67-81. doi.org/10.1016/j.apgeochem.2018.05.007.

Torres E., Turrero M.J., Escribano A., Martín P.L. (2013). Geochemical interactions at the concrete-bentonite interface of column experiments. Deliverable 2.3-6-1 of PEBS Project.

Turrero M. J., Villar M. V., Torres E., Escribano A., Cuevas J., Fernández R., Ruiz A. I., Vigil de la Villa R., del Soto I. (2011). Laboratory tests at the interfaces. Final results of the dismantling of the tests FB3 and HB4. Deliverable 2.3-3-1 of PEBS Project.

Wollery T.J. (1992). EQ3/3. A software package for geochemical modeling of aqueous system: package overview and installation guide version 7.0. UCRL-MA-110662-PT-I, Lawrence Livermore National Laboratory, Livermore, California.

Zheng L., Samper J., Montenegro L., Fernández A.M. (2010). A coupled model of heating and hydration laboratory experiment in unsaturated compacted FEBEX bentonite. Journal of hydrology 386, 80-94.

Zheng, L., Samper, J., Montenegro, L. (2011). A coupled THC model of the FEBEX in situ test with bentonite swelling and chemical and thermal osmosis. J. Contam. Hydrol. 126, 45–60.

16 CTU/ D. Vopálka, T. Rosendorf, K. Štamberg, J. Kittnerová, L. Baborová

Abstract

The modeling carried out at CTU within WP3 was devoted to the support of evaluation of diffusion experiments performed in Czech laboratories (UJV and CTU-CEG) with tritium and chloride within WP1 and of batch and diffusion experiments with strontium and radium performed in our laboratory (CTU-DNC) within WP2. Several versions of diffusion models in the GoldSim environment were developed and applied, and some attempts were made to formulate a model description of the strontium and radium uptake on various cementitious materials studied. Selected results in both directions of study, with emphasis on the work done during the last two years of the CEBAMA project, are summarized in this contribution. One of the main goals of Czech laboratory program within WP1 was the determination of changes in tritium diffusivities on samples of hardened cement paste HCP-CEM_II and RPM (CEBAMA reference mix paste design) that interacted with groundwater 9, 18, and 27 months at two different temperatures (10 ºC and 95 ºC). The through diffusion experiment dataset was offered by UJV-partner, some R_d (K_d in equilibrium) values for modeling were selected from the findings reported by KIT on similar cementitious materials to model diffusion of radionuclides with low K_d values. Results of radium uptake and diffusion performed within WP2 were evaluated and modeled with the models developed. An attempt was done to describe sorption kinetics by kinetic models devoted to the two-phase systems and a model of diffusion experiments was successfully applied to the description and interpretation of through-diffusion experiments of Ra through the layer of crushed hydrated cement paste.

16.1 MODEL OF DIFFUSION EXPERIMENTS

For the evaluation and modeling of various types of diffusion experiments, a module being developed in the GoldSim environment (e.g. Vopálka, 2016 and Vopálka et al. 2017) has been used. The current version of this tool enables to describe through-diffusion experiments conducted in a static diffusion cell with variable concentration of studied species in the inlet and outlet containers. This is an advantageous laboratory method, since it is not necessary to keep constant concentrations in working containers by renewing inlet and outlet solutions, which might bring a systematic error into the system. The model enables further to determine the effective diffusion coefficient, D_e, and the apparent diffusion coefficient, D_a, without the need of having to wait until steady-state is reached. The evaluation method mentioned requires the determination of the total concentration profile in the studied layer after the experiment termination. In this way, one diffusion experiment provides three experimental curves, i.e. break-through (downstream) and depletion (upstream) curves, and tracer concentration profile in the studied layer, which might be then fitted with the model. A simplified reactive transport model is considered by the implementation of either linear or non-linear empirical (Freundlich or Langmuir) sorption/desorption isotherms, describing reversible uptake/release of observed species. The fitting of model curves to experimental data is possible by multi-parametric optimization using Box's method (Box, 1965). The model serves not only for the evaluation of the experiments performed but can also be used to improve understanding of the behavior of the diffusion cell, which could facilitate the preparation of new experiments.

16.2 DESCRIPTION OF THE MODELING WORK RELATED WITH WP1

Experimental setup

Experimental work within the Czech program in WP1 of CEBAMA focused on alteration and interaction studies on two types of hardened cementitious pastes (Večerník et al., 2016; Vašíček et al., 2018):

(1) “HCP-CEM_II”: cement paste based on Portland type CEM II A-S 42.5R, w/c = 0.45, with porosity over 40 %, and
(2) “RPM”: CEBAMA reference paste mix with low-pH porewater and porosity (capillary and gel porosity) approx. 24-30 % (Vehmas et al., 2016, 2018) in contact with groundwater from Underground Research Facility Josef (GW Josef) or bentonite 75 (B75) suspension (GW Josef:B75 ~ 5:1) in pressure vessels during three sampling campaigns (9/18/27 months) for HCP-CEM_II samples and two campaigns (9/18 months) for RPM samples under in-situ (10°C) and high temperature (95 ºC) load. The overview of the experimental program is presented in Table 16.1.

Table 16.1. *Summary of experimental program - long-term laboratory experiments, geochemical and thermal interaction in the system with cementitious samples (ca. 50 mm in diameter, 8 mm in thickness).*

Sampling periods	Ageing procedures	B75 suspension	GW Josef	Temperature
9, 18 (27) months	Bentonite suspension + HCP-CEM_II / RPM	×	×	10 / 95°C
	GW Josef + HCP-CEM_II / RPM	×	×	10 / 95°C
	HCP-CEM_II or RPM + humid air (in-situ)*			10°C

* *No ageing procedures of cements samples with humid air were considered in this contribution.*

The main goal was to understand how the geochemical interaction processes affect the mechanical, geochemical and finally transport properties of selected radionuclides (tritiated water and chloride-36) in cementitious materials. The determination of changes in diffusivities was evaluated using an analytical solution (e.g. Crank, 1975; Van Loon et al., 2003) or by a sophisticated tool for predictive modeling and evaluation of through-diffusion experiments developed in GoldSim. This tool takes into account 3 datasets: (1) breakthrough curves, (2) depletion curves, and finally (3) concentration profile in the layer (Vopálka, 2016). The whole database of interim results (without last sampling period for both materials) was presented in the 2nd data freeze of WP1 and raw data are open upon a request by partner organization UJV. Diffusion experiments on a cementitious material from the last sampling period (27 months for HCP-CEM_II and 18 months for RPM) are not yet finished (to date: beginning of February 2019) but all were evaluated till the end of January 2019 without any consideration of the third dataset.

Modeling: diffusion of tritium and chloride on cementitious materials

Based on KIT observations (Ait-Mouheb et al., 2017) on similar low-pH cementitious materials or based on literature review by Evans et al. (2008) or Ochs et al. (2016), none or minimal retardation processes (sorption, isotopic exchange, rehydration) represented by a distribution ratio R_d (or K_d in equilibrium) were expected on low pH-cement materials for tritium and chloride, and on HCP-CEM_II samples for tritium. Without the knowledge of ratio of C/S or C/A phases, the determination of the uptake of chloride-36 on HCP-CEM_II samples is still open for additional analyses (XRF, SEM), which are further planned in a Ph.D. thesis by Rosendorf (release expected by the end of 2020). These additional analyses were initiated from observations of high chloride uptake during through-diffusion experiments performed within WP1 by UJV-partner. Unfortunately, these data will not be reported till the end of CEBAMA. On contrary, the diffusion of chloride on RPM samples was very slow with minimal decrease in the inlet reservoir (minimal increase in the outlet reservoir), therefore the values for D_e were estimated as a lower than $5 \cdot 10^{-13}$ $m^2 s^{-1}$, in some cases lower than 10^{-13} $m^2 s^{-1}$.

HCP_CEM_II and RPM: diffusion of ^{3}H (HTO) without considering retardation processes

Evaluation and modeling of tritium diffusion (without considering retardation processes, K_d or R_d = 0 dm^3kg^{-1}) on HCP-CEM_II samples that were 9 months under interaction loads was discussed in previous works within WP3 (Rosendorf et al., 2016, 2018). From the evaluation of results, it can be concluded that the high-temperature load (foregoing the diffusion experiment) increased the values of HTO effective diffusion coefficients (D_e) in the case of HCP-CEM_II samples even by one order of magnitude. The effect on ageing (sampling campaigns after 18 or 27 months of interaction) was not significant. The differences of temperature load could be related to the dissolution of material under higher temperature or degraded mechanical properties (punch compressive strength test performed by CTU-CEG-partner). All results (including running experiments) are presented in Figure 16.1. The running experiments were evaluated without any consideration of the concentration profile dataset and with expected porosity 0.30 ± 0.10 for RPM, 0.45 ± 0.10 for HCP-CEM_II, respectively.

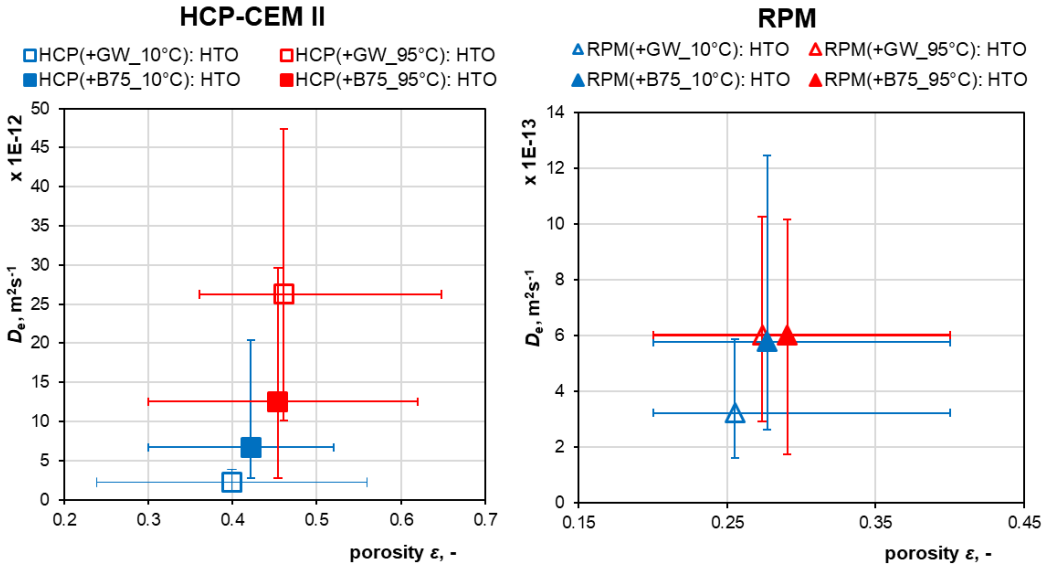

Figure 16.1. *Effective diffusion coefficient of HTO on HCP-CEM II (left) and RPM (right) samples: dependency on the fitted porosity of the samples; each series with cement materials: mean value of porosity is calculated only from finished experiments (uncertainties are included).*

RPM: diffusion of ^{3}H (HTO) considering low K_d values

The tritium diffusion on the RPM samples considering retardation processes was modeled and evaluated in the last year of the project, where 3 parameters (porosity, geometrical factor and distribution ratio K_d) were taken into account using GoldSim (considering all three datasets). To avoid the effect of voids clogging (heterogeneity of porosity) in cementitious samples caused by the contact with bentonite suspension in pressure vessels preceding the TD experiments, we selected for modeling only two experimental series that were not in contact with bentonite suspension (see below). Modeling conditions of through-diffusion experiments at laboratory conditions (~22°C) are schematically described as follows:

- Hardened RPM cylinders: ca 50 mm diameter, ca 8.2–8.4 mm thick.
- Diffusion cells identification:
  - Cells "**a**" and "**b**", series "**RPM (+GW_95°C_9M): HTO**": HTO (^{3}H) diffusion on RPM samples from interaction RPM with GW Josef at 95°C for 9 months,
  - Cells "**d**" and "**e**", series "**RPM (+GW_10°C_9M): HTO**": HTO (^{3}H) diffusion on RPM samples from interaction RPM with GW Josef at 10°C for 9 months.
- 1D-through diffusion experiment: non-constant concentration of tracer (^{3}H) in the reservoirs in diffusion cells (dataset: evolution of concentration activity in the inlet reservoir).

- Duration of diffusion experiments: 162–252 days.
- Volumes of inlet and outlet reservoirs: V = 56–59 cm^3.
- Reference diffusivity of HTO in water: D_w = 2.44×10^{-9} $m^2 \cdot s^{-1}$ (Berne et al., 2010), initial concentration activity in the inlet reservoir a ~ 5 MBq L^{-1} (C_0 ~ 4.7 nM)
- The value of an effective diffusivity D_e ($=D_w \cdot G \cdot \varepsilon$) was determined on the base of geometrical factor G fitting.
- The K_d value was limited during modeling by an interval from 0.0 to 0.4 $dm^3\,kg^{-1}$ with the aim to assess the influence of such small K_d values on the diffusion of "non-reacting" species, since Ochs et al. (2016) estimated a K_d-value (R_d) = 0. The upper limit was derived from batch sorption experiments of tritium on low-pH mixtures performed by KIT (Ait Mouheb et al., 2017) as a mean value. In the authors' opinion, the K_d (R_d) in this interval of low values can be hardly experimentally proved due to an uncertainty of the liquid scintillation detection (LSC) used for the determination of HTO concentration activity, neither for diffusion experiments performed by UJV. It can be derived that this problem could be relevant from real experiments with HTO. This selected interval can heal a difference of tracer balance in all three datasets: (1-2) measured concentration activity in both reservoirs and (3) the concentration profile in the layer. Especially the third dataset could offer wrong experimental values (for right obtained concentration of beta emitter in the layer it is necessary to achieve full tracer desorption into supernatant and to secure no evaporation of tritiated water during abrasion of samples [(1)]. If these conditions are not met, it is necessary to expect models of the third dataset with overstated values in contrary to observed values, since the real values cannot be determined). Therefore, the third dataset cannot be included in the evaluation with the same weight the first and the second ones: the third dataset has a sole condition: to be equal or higher than the model of the porewater (the total concentration in the layer subtracted by the part in the solid phase) and lower than the total concentration in the layer.
- The value of an apparent diffusivity D_a ($=D_e \cdot \alpha^{-1}$, where capacity factor $\alpha = \varepsilon + \rho_d \cdot K_d$) was determined.

Results of fitting of experimental results with the model are presented as an example in Figure 16.2 and Table 16.2 (cell "e" - diameter 50.58; thickness 8.35 from "RPM (+GW_10°C_9M): HTO" series). The biggest difference between experimental and modeled data is in the concentration profile as it was expected in the model described above. In case of K_d = 0 (models "e_M1", "e_M5" and "e_M9"), the models of the concentration profile in the whole layer and its part in the porewater are equal. Time evolution of relative concentration activity in both reservoirs proves that minimal change of K_d (that cannot be experimentally determined by batch sorption experiments) can crucially change the description of the whole diffusion process. For example, shape of depletion and breakthrough curves and the effective diffusion coefficients and other parameters can be wrongly interpreted and evaluated.

[1] Concentration profile in the layer was obtained by an abrasive technique described in (Rosendorf et al., 2018; Hofmanová et al., 2018), however an endurance of RPM samples was not satisfactory, as samples often cracked. Therefore, the number of experimental points was limited to low number – 1 to 4, where the first one was almost unusable because of an evaporation of HTO from the surface of the sample during its bonding on the surface of abrasive device.

Table 16.2. *Basic information about RPM sample in diffusion cell "e" (GoldSim models 1–12 used in Figure 16.3).*

EXPERIMENTAL Bulk (dry) density ρ_d Grain density ρ_s, kg dm^{-3}	Capacity factor $\alpha = \varepsilon + \rho_d \cdot K_d$, -		K_d, dm^3 kg^{-1}	G, - (× 10^{-4})	D_e, m^2 s^{-1} (× 10^{-13})
	Porosity ε, -	$\rho_d \cdot K_d$, -			
1.86 ± 0.06 2.46 ± 0.06	0.242 ± 0.031	0.28 ± 0.28	0.15 ± 0.15	7.0 ± 3.5	4.1 ± 2.1
MODEL: e_M1	0.211	0	0	4.1	2.1
MODEL: e_M2		0.47	0.25	7.7	4.0
MODEL: e_M3		0.56	0.30	8.3	4.3
MODEL: e_M4		0.65	0.35	9.0	4.6
MODEL: e_M5	0.242	0	0	3.8	2.2
MODEL: e_M6		0.37	0.20	6.7	4.0
MODEL: e_M7		0.47	0.25	7.0	4.1
MODEL: e_M8		0.56	0.30	7.5	4.4
MODEL: e_M9	0.273	0	0	3.5	2.3
MODEL: e_M10		0.37	0.20	5.8	3.9
MODEL: e_M11		0.47	0.25	6.3	4.2
MODEL: e_M12		0.83	0.30	6.8	4.5

Table 16.3. *Basic information about RPM samples in diffusion series "RPM (+GW_95°C_9M): HTO" – cells "a" and "b" and "RPM (+GW_10°C_9M): HTO" – cells "d" and "e".*

EXPERIMENTAL Bulk (dry) density ρ_d Grain density ρ_s, kg dm^{-3}		Capacity factor $\alpha = \varepsilon + \rho_d \cdot K_d$, -		G, - (× 10^{-4})	D_a, m^{2}s^{-1} (× 10^{-13})	D_e, m^{2}s^{-1} (× 10^{-13})
		Porosity ε, -	$\rho_d \cdot K_d$, -			
Cell a	1.78 ± 0.05 2.43 ± 0.06	0.267 ± 0.027 fit: 0.24 ± 0.09	0.18 ± 0.18	12.3 ± 9.9	19 ± 18	8.0 ± 6.0
Cell b	1.78 ± 0.05 2.48 ± 0.06	0.280 ± 0.027	0.27 ± 0.27	5.8 ± 4.2	7.2 ± 6.4	4.0 ± 3.0
Cell d	1.80 ± 0.05 2.46 ± 0.06	0.269 ± 0.027	0.18 ± 0.18	4.8 ± 1.2	7.0 ± 3.4	3.1 ± 0.8
Cell e	1.86 ± 0.06 2.46 ± 0.06	0.242 ± 0.031	0.28 ± 0.28	7.0 ± 3.5	7.9 ± 5.9	4.1 ± 2.1

Both series "RPM (+GW_95°C_9M): HTO" and "RPM (+GW_10°C_9M): HTO" with results are shown in Figure 16.3 and Table 16.3. Cell "a" shows a different trend than the second cell "b" in the same series, for now without a known reason. Table 16.3 shows how the disagreement between datasets in both reservoirs raises uncertainties. Due to the same decrease of activity (except cell "a") and different breakthrough curve in both series, we cannot exclude retardation processes in the evaluation. Therefore, even small K_d values that were determined for tritium in the cementitious systems should be taken into account.

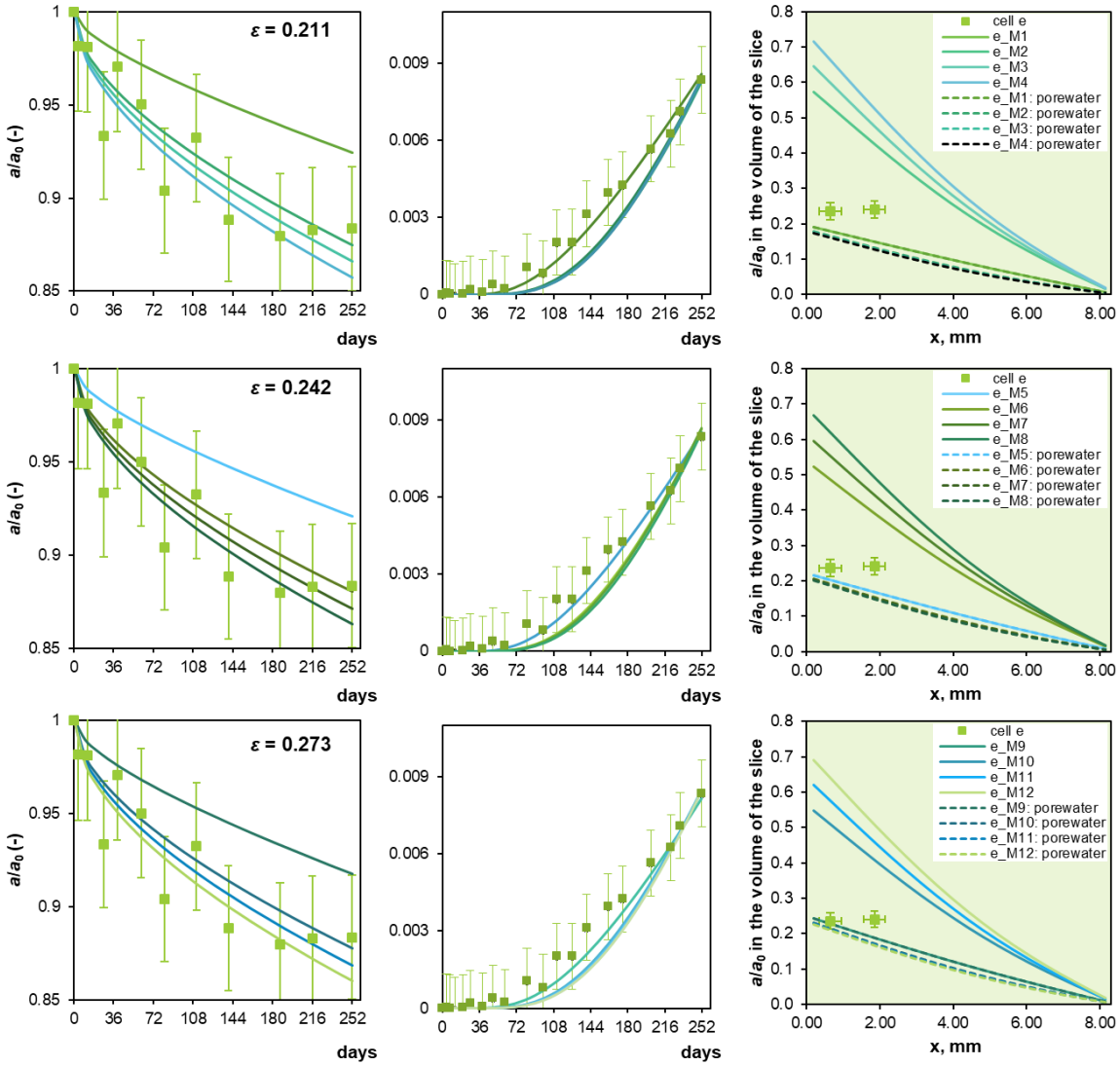

Figure 16.2. *The time evolution of the relative concentration activity of ^{3}H in both reservoirs and the profile of the RPM modeled by GoldSim; models used parameters from Table 16.2 for cell "e" (series RPM (+GW_10°C_9M): HTO), where uncertainties in the concentration profile did not include errors caused by abrasive and desorption processes mentioned in the text.*

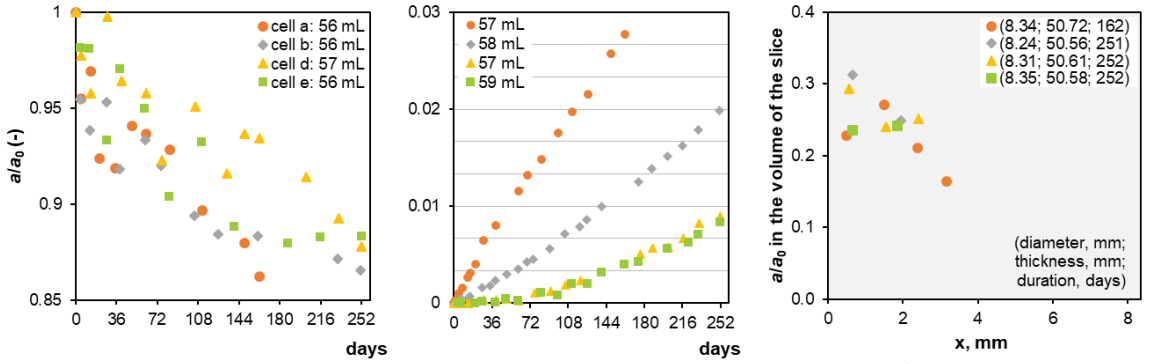

Figure 16.3. *The time evolution of the relative concentration activity of ^{3}H in both reservoirs and the profile of the RPM for cell "a" and "b" (RPM (+GW_95°C_9M): HTO), "c" and "d" (RPM (+GW_10°C_9M): HTO), respectively.*

16.3 DESCRIPTION OF THE MODELING WORK RELATED WITH WP2

Experimental

A study of sorption behavior was done on three cementitious materials: one hardened cement paste HCP CEM_II and two types of concrete (concrete based on CEM I and concrete based on CEM III); all crushed and sieved to a fraction ≤ 0.4 mm.

The isotope ^{223}Ra used in the experiments was obtained from the ^{227}Ac/^{223}Ra generator. This is a glass column with Dowex-1 × 8 resin. Elution of ^{223}Ra is carried out with 0.7 M nitric acid in 80% methanol. The eluate is evaporated to dryness in a vacuum evaporator and then dissolved in 1M nitric acid (Kozempel et al., 2015). ^{223}Ra is an almost pure α radiator with a half-life of 11.43 days decaying to ^{219}Rn, but in the order of 10^{-10} % ^{223}Ra is converted by ^{14}C emission to ^{209}Pb, while the final decay product of ^{219}Rn is ^{207}Pb (Collins et al., 2015). The radon isotope ^{219}Rn has a half-life of 4 seconds and therefore does not interfere with ^{223}Ra measurement. The use of ^{223}Ra is also less problematic in terms of the safety of experimental work in comparison with ^{226}Ra that produces the dangerous isotope ^{222}Rn. The measurement was held in a relative manner: comparison between activities in starting solution and in the sample. The sorption experiment is composed of determination of the sorption kinetics and describing the obtained sorption equilibrium using the distribution ratio K_d. First, the kinetics of sorption of radium for all cementitious materials were verified, and the duration of the equilibrium experiments was then determined as 4 days (96 hours).

All experiments were carried out in simulated leachate of cementitious materials. This medium was a saturated solution of portlandite (pH = 12.4–12.6). The variables were a phase ratio of 10–1000 L/kg (6 ml liquid phase) and a temperature of 22–80 °C. The kinetic experiment was interrupted at predetermined intervals (2, 4.5, 8, 24, 30, 48 and 96 hours) for sampling. 2 ml of solutions were taken to an activity measurement in a well-type scintillation detector NaI(Tl). The measured sample was then returned to the reaction vial. The equilibrium experiments were evaluated after 96 hours and proceeded similarly to the kinetic experiment.

Due to the relatively short half-life of the ^{223}Ra isotope, the measured decreases in radioactivity in the liquid phase samples caused by the sorption of radionuclide on the solid cementitious material have to be separated from the loss of radioactivity by the decay of the isotope used. For this correction, a procedure based on exponential decay was used to convert all measured data to the same time – t_0 corresponding to the start of the experiment.

Kinetic models for two-phase (liquid-solid) systems

The kinetic models summarized in Table 16.4 reflect the following different rate-controlling processes: mass transfer (DM), film diffusion (FD), diffusion in inert layer (ID), diffusion in reacted layer (RLD), chemical reaction (CR), and gel diffusion (GD) (Beneš et al., 1994).

In Table 16.4, concentrations in liquid (C) and solid phases (q) meet at each time the mass balance relationship ($q = Vm^{-1}(C_0 - C) + q_0$), where C_0 and q_0 are initial concentrations in the system, and q^* and C^* represent equilibrium concentrations connected with the corresponding concentrations in opposite phases by an equilibrium model (e.g. linear, Langmuir or Freundlich).This relation implies the form of the rate equation for the concentration in the liquid phase. Other symbols: $\frac{V}{m}$ – phase ratio of aqueous and solid phases, K_{DM}, K_{FD}, K_{ID}, K_{RLD}, K_{CR}, K_{GD} – over-all kinetic coefficients; r_{CR} – rate of the chemical reaction; R - mean radius of the solid phase particle; ρ – specific mass of the solid sorbent; δ - thickness of the "liquid film" on the surface of the solid particle, D – diffusion coefficient of the component in the material of solid particles.

***Table 16.4**. Kinetic models of sorption applied in two-phase system crushed cementitious material – alkaline working solutions.*

Control process	Model notation	Differential equation
mass transfer	DM	$\frac{dq}{dt} = K_{\mathrm{DM}}(q^* - q)$
film diffusion	FD	$\frac{dq}{dt} = K_{\mathrm{FD}}(C^* - C); K_{\mathrm{FD}} = \frac{3D}{\delta R \rho}$
diffusion in an inert layer	ID	$\frac{dq}{dt} = K_{\mathrm{ID}} \frac{C^* - C}{(1 - \frac{q}{q^*})^{-\frac{1}{3}} - 1}; K_{\mathrm{ID}} = \frac{3D}{R^2 \rho}$
diffusion in a reacted layer	RLD	$\frac{dq}{dt} = K_{\mathrm{RLD}} \frac{q^* - q}{(1 - \frac{q}{q^*})^{-\frac{1}{3}} - 1}; K_{\mathrm{RLD}} = \frac{3D}{R^2 \rho}$
chemical reaction (taking place in the reaction zone, here for the first order reversible reaction)	CR	$\frac{dq}{dt} = K_{\mathrm{CR}} \frac{C - C^*}{(1 - \frac{q}{q^*})^{-\frac{2}{3}}}; K_{\mathrm{CR}} = \frac{3r_{\mathrm{CR}}}{R \rho}$
gel diffusion	GD	$\frac{dq}{dt} = K_{\mathrm{GD}} \frac{(q^* - q_0)^2 - (q^* - q_0)^2}{q - q_0}; K_{\mathrm{GD}} = \frac{D\pi^2}{2R^2}$

The procedure of the kinetic experimental data evaluation

In the case of evaluation of the concentration decrease in the liquid phase the experimental data are compared with the computed concentrations corresponding to individual models (after each time of the concentration measurement). The fourth-order Runge-Kutta method was used for the numerical solution of differential equations. The Newton-Raphson non-linear regression method was used for the determination of desired parameters of kinetic models, minimizing the value of a criterion of the goodness-of-fit. The quantity $\frac{\chi 2}{\nu}$ (or $\frac{WSOS}{DF}$, see equation 16.1) is thought to be the appropriate criterion of the goodness-of-fit. It holds that the fit is acceptable if $0.1 < \frac{WSOS}{DF} < 10$ (Herbelin and Westall, 1996).

$$\chi 2 = \sum_i^n \frac{SSx_i}{s_i^2} \qquad (16.1)$$

Here $(SSx)_i$ is the square of the *i*-th deviation of corresponding experimental value from the calculated one, s_i is an estimate of standard deviation of the *i*-th experimental point, and degree of freedom, ν (or *DF*) is the number of experimental points (*n*) reduced by the number of independent parameters (n_p). Within the evaluation of real kinetic experiments, it was assumed that the relative standard deviations of all experimental uptake data are 0.1 and that the results of long-term experiments determine the shape of the equilibrium isotherm.

This approach to the evaluation of kinetic sorption experiments was successfully applied in previous work at our laboratory (e.g. Distler at al., 2018 or Lujanienė et al., 2012).

Demonstration of the evaluation approach prepared

Four sets of kinetic experiments of Ra uptake on hardened cement paste HCP CEM_II were evaluated by six kinetic models with the aim to find the best of them that could help to assess the process controlling the Ra uptake.

***Table 16.5**. The $\frac{\chi 2}{\nu}$ (WSOS/DF) values attained by evaluation of kinetics of ^{223}Ra sorption in the system HCP CEM II – saturated $Ca(OH)_2$ for various phase ratios V/m and two working temperatures. K_d model was used for the description of sorption isotherms.*

	V/m L·kg^{-1}	***K*$_d$** L·kg^{-1}		**Model**					
				DM	**FD**	**ID**	**RLD**	**CR**	**GD**
HCP CEM II $Ca(OH)_2$, 22 ^{0}C	10	77	χ^2/ν	3.8	6.7	6.9	9.1	4.2	20.6
	100	124	χ^2/ν	0.60	0.80	2.9	1.2	4.2	9.8
	1000	564	χ^2/ν	0.58	0.72	0.2	0.53	0.50	0.51
HCP CEM II $Ca(OH)_2$, 80 ^{0}C	10	472	χ^2/ν	38	257	162	32	255	27

The presented method of evaluation of kinetic experiments was applied to 15 sets of kinetic experiments of Ra on three types of cementitious materials with various conditions of experiments. A thorough analysis of the results is being prepared for a separate publication. The best agreement of model data with the experiment, i.e. the lowest value of the criterion $\frac{\chi 2}{\nu}$, was achieved, on average, for models of mass transfer (DM), film diffusion (FM), and diffusion in an inert layer (ID). No significant difference between studied materials was observed.

Table 16.5 and in Figure 16.4 show, as a demonstration, results of evaluation of four data sets belonging to the study of ^{223}Ra uptake on crushed HCP CEM_II in the working solution of saturated $Ca(OH)_2$ for two working temperatures. It is seen, from Table 16.5, that the choice of the ideal model is unambiguous, and it is clear from the pictures that the conformation of the model with the experimental course is not perfect. However, we assume that this quantitative evaluation will help us to evaluate the sorption properties of cementitious materials and eventually to prepare the transport model of the radium in the cementitious barrier.

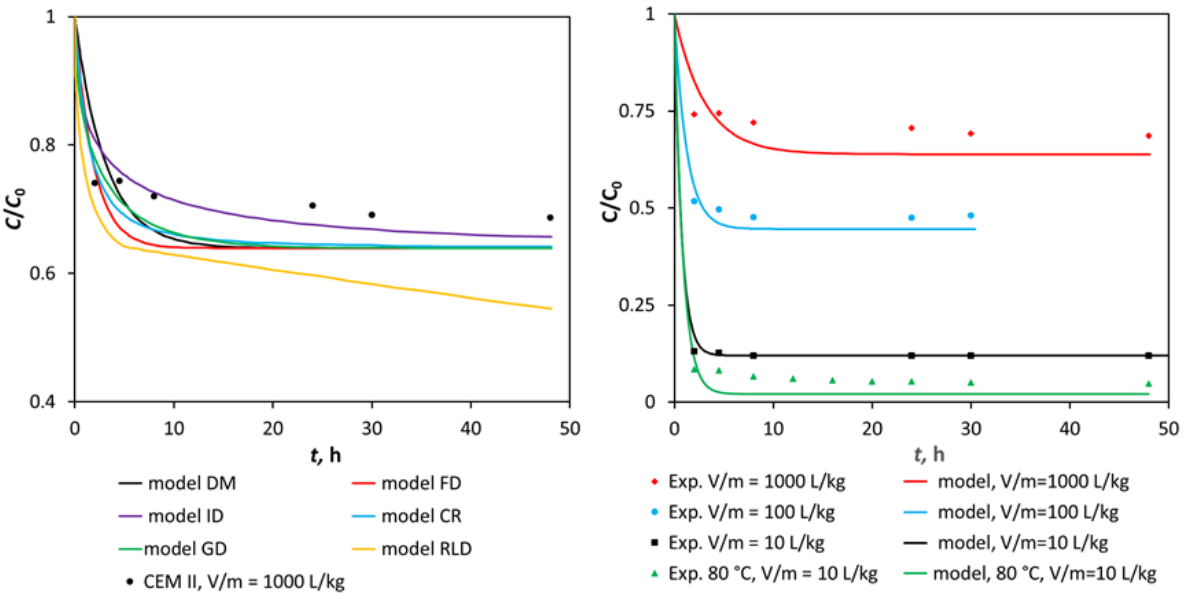

***Figure 16.4.** An example of experimental kinetic data fitting by different kinetic models (left) and application of the model of mass transfer (DM) on the evaluation of four sets of kinetic experiments (right).*

Diffusion of Ra through the pressed layer of crushed hydrated cement paste

Two diffusion experiments with ^{223}Ra were carried out in saturated $Ca(OH)_2$ solution (portlandite water) or synthetic cement water (CPW) through the HCP CEM_II layers (CEM II A-S 42.5R), which were formed by pressing a crushed cementitious material. The aim of these experiments was the continuation in the study of the influence of phase ratio *V*/*m* on the value of distribution coefficient K_d.

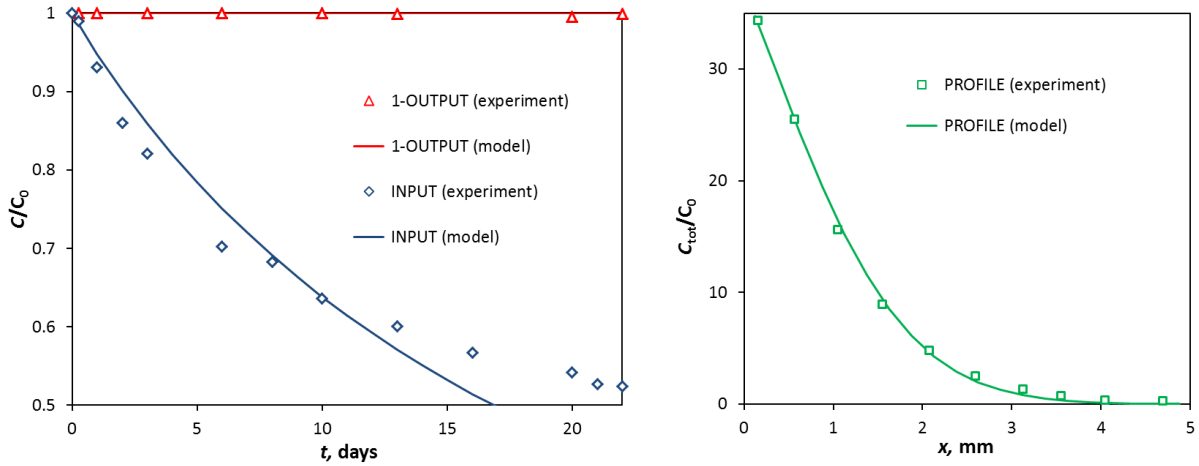

Figure 16.5. *Results of ^{223}Ra through-diffusion experiment of, which lasted 22 days, in portlandite equilibrated water and its optimal fit.*

The solid material layer of 0.5 cm width was saturated with the appropriate solution prior to the addition of the migrating ^{223}Ra. The volumes of the inlet and outlet containers were 50 ml, separating filters of 0.08 cm width were used for the separation of cementitious material from containers with working solutions. Radium used for the diffusion study was the isotope ^{233}Ra, with a concentration in the range of 10^{-12} mol·L^{-1}. The duration of the experiments was 22 days.

For the evaluation of the experiments, it was necessary to use the multicomponent fitting procedure implemented in the GoldSim environment, as the stationary state was not reached. Figure 16.5 shows the experimental results of Ra diffusion in portlandite water and model curves corresponding to the optimal fits. The quality of fits demonstrates that the model description assuming the linearity of the sorption model and reversibility of the sorption process might be valid for the retarded diffusion transport of and Ra.

The results of diffusion experiments are in agreement with results of batch experiments, as the K_d values for ^{223}Ra computed on the basis of evaluation of diffusion experiments gives similar values as the extrapolation of K_d dependence on phase ratio *V*/*m* to lower values, in both cases about 100 L·kg^{-1}.

16.4 CONCLUSIONS AND MAIN OUTCOMES

Experimental and modeling work show to the relevance of considering retardation processes (sorption, isotope exchange), even with low K_d values of tritium in the cementitious systems during diffusion experiments. Without considering these low values, the whole system can be misinterpreted and wrongly evaluated. The use of three datasets for evaluation and modeling with GoldSim has an advantage for consideration of all experimental uncertainties and difficulties related to measuring low tracer activities. The developed model of diffusion experiments implemented in the GoldSim environment was successfully applied to the evaluation of radium through-diffusion experiments in the non-steady state through the layer of crushed cementitious material. The

application of two-phase (solid and liquid) models to the description of the sorption kinetics helped to understanding the processes of radium uptake by a cementitious material.

Acknowledgements

The research leading to these results has received funding from the European Union's Horizon 2020 Research and Training Programme of the European Atomic Energy Community (EURATOM) (H2020-NFRP-2014/2015) under grant agreement n° 662147 (CEBAMA). This contribution is a partially result of Grant No. SGS16/250/OHK4/3T/14 provided by the Grant Agency of the Czech Technical University in Prague.

16.5 REFERENCES

Ait Mouheb N., Montoya V., Schild D., Soballa E., Christian A., Geyer F., Schäfer T. (2017). Proceedings of the 2nd Annual Workshop of the CEBAMA project (deliverable n° D4.12).

Beneš P., Štamberg K., Štegman R. (1994). Study of the kinetics of interaction of Cs-137 and Sr-85 with soils using a batch method: methodological problems. Radiochim. Acta. 66 (67), 315–321.

Berne P., Bachaud P., Fleury M. (2010). Diffusion properties of carbonated caprocks from the Paris Basin. Oil & Gas Science and Technology – Rev. IFP, 65, 473–484.

Box M.J. (1965) A new method of constrained optimization and a comparison with other methods. The Computer Journal, 8(1), 42–52.

Collins S.M., Pearce A.K., Ferreira K.M., Fenwick A.J., Regan P.H., Keghtley J.D. (2015). Direct measurement of the half-life of ^{223}Ra. Applied Radiation and Isotopes, 99, 46–53.

Crank J. (1975). Mathematics of diffusion. Second edition. Oxford University Press.

Distler P., Štamberg K., John J., Harwood L.M., Lewis, F.W. (2018). Modelling of the Am(III) - Cm(III) kinetic separation effect observed during metal ion extraction by bis-(1,2,4)-triazine ligands. Sep. Sci. Technol. 2018, 53(2), 277–285.

Evans N.D.M. (2008). Binding mechanisms of radionuclides to cement. Cement and Concrete Research, 38, 543–553.

Herbelin A.L., Westall J.C. (1996). FITEQL-A computer programm for determination of chemical equilibrium constants from experimental data, Version 3.2, Report 96-01. Corvallis, Oregon, Department of Chemistry, Oregon State University.

Hofmanová E., Rosendorf T., Zuna M., Havlová V., Srba O. (2018). Profile analysis of Aare granite samples after radionuclide migration. Czech Chemical Society Symposium Series: 18th Radiochemical Conference. Česká společnost chemická, 16 (2).

Kozempel J., Vlk M., Málková E., Bajzíková A., Bárta J., Santos-Oliveira R., Malta Rossi A. (2015). Prospective carriers of ^{223}Ra for targeted alpha particle therapy. Journal of Radioanalytical and Nuclear Chemistry, 304, 443–447.

Lujanienė G., Beneš P., Štamberg K., Šapolaitė J., Vopálka D., Radžiūtė E. (2012). Kinetics of plutonium and americium sorption to natural clay. J. of Environmental Radioactivity, 108, 41–49.

Ochs M., Mallants D., Wang L. (2016). Radionuclide and metal sorption on cement and concrete. Springer Intentional Publishing.

Rosendorf T., Vopálka D., Červinka R. (2016). Evaluation and modeling of through diffusion experiments of HTO on samples of hydrated OPC affected by different thermal conditions. Deliverable n° D3.05, CEBAMA: Description of and results from the modeling of external lab and/or field experiments.

Rosendorf T., Vopálka D., Červinka R. (2018). Evolution of mineralogy and radionuclide diffusion on Portland-type cementitious materials due geochemical and thermal effects. Czech Chemical Society Symposium Series: 18th Radiochemical Conference. Česká společnost chemická, 16 (2).

Van Loon L.R., Soler J.M., Jakob A., Bradbury M.H. (2003). Effect of confining pressure on the diffusion of HTO, $^{36}Cl^-$ and $^{125}I^-$ in a layered argillaceous rock (Opalinus Clay): diffusion perpendicular to the fabric. Applied Geochemistry, 18, 1653–1662.

Vašíček R., Červinka R., Večerník P., Rosendorf T., Svoboda J. (2018). Geochemical and thermal impacts on the characteristics of cementitious materials: strength, leachate pH, mineralogy and diffusion. Proc. 3rd Annual Workshop of the CEBAMA project, Nantes, France (in press).

Večerník, P., Hausmannová, L., Červinka, R., Vašíček, R., Roll, M., Hloušek, J., Havlová, V. (2016). Interaction between cement and Czech bentonite under temperature load and in in-situ conditions: an overview of experimental program. Proceedings of the 1st Annual Workshop of the CEBAMA project, KIT scientific report 7734.

Vehmas T., Leivo M., Holt E., Alonso M. C., Férnandez Á., Calvo J. L. G., Vašíček R., Červinka R., Večerník P., Rosendorf T., Svoboda J., Finck N., Montoya V., Ait Mouheb N., Dardenne K., Rothe J., Schäfer T., Geckeis H., Gaboreau S. (2018). CEBAMA reference mix design for low-pH concrete and paste, intermediate results. Proceedings of the 3rd CEBAMA Annual Workshop, Nantes, France (in press).

Vehmas T., Schnidler A., Löija M., Leivo M., Holt E. (2016). Reference mix design and castings for low-pH concrete for nuclear waste repositories. Proceedings of the 1st Annual Workshop of the CEBAMA project, KIT scientific report 7734.

Vopálka D. (2016). CTU – DNC modeling approach. Deliverable n° D3.02, CEBAMA: Review and definition of modeling approaches: scale of analysis, physico-chemical processes, software, HPC resources.

Vopálka D., Vetešník A., Hofmanová E. (2017) Methods of evaluation of through-diffusion experiments on sandwich bentonite cement layers in a simple experimental set-up. Proceedings of the 1st Annual Workshop of the CEBAMA project, KIT scientific report 7734.

18 VTT/ T. Vehmas, A. Itälä

Abstract

This contribution describes the work of VTT within WP3 of the CEBAMA project, which was undertaken during the first 28-months of the four-year project. This work was already reported in the previous deliverable of WP·, i.e. D3.05 and is included here as well for completeness.

18.1 INTRODUCTION

Cementitious materials' pore solution has a naturally high pH of 13–14. Bentonite backfill and buffer properties are potentially altered due to high -pH leachate interaction from plug materials. Some of the nuclear waste managing organizations, such as Posiva (Finland), SKB (Sweden) and NUMO (Japan), have targeted a pH limit ≤11 for cementitious leachates. It has been suggested that more natural pH limit would be pH ≤10, as silicates aqueous behaviour changes. In pH <10, silicates are in neutral SiO_2(aq) form in solution whereas in pH > 10 silicates dissociates to charged species $HSiO_3^-$. Correspondingly, the solubility of quartz increases by three orders of magnitude compared to the pH range 1–10 (Savage, 2007).

18.2 MATERIALS RELATED TO MODELLING

The highest tolerable pH of the leachate is 10 or 11 in the bentonite system. Otherwise the long-term stability of the engineered barrier system might be endangered. Mix designs having a leachate pH lower than natural pH of 13–14 have been formulated (Cau dit Coumes et al., 2006; Holt et al., 2014; Vogt et al., 2009; Martino et al., 2011; Holt et al., 2016). The low-pH mix designs consist of low alkaline Portland cements mixed with large amounts of pozzolanic materials. Pozzolanic materials are known to react with the hydration products that control the pH of the cementitious materials pore solution. Low-pH materials are still highly basic but the pH value is significantly lower than in traditional Portland cements.

The materials used to study low-pH concretes in repository environment were:

1. Ordinary Portland cement from Degerhamn manufactured by Cementa Ab.
2. Granulated silica fume (Parmix supplided by Finnsementti Oy)
3. Blast furnace slag was from Finnsementti Oy
4. Fly ash was from Denmark by E-mineral.
5. Quartz filler purchased from Silbeco Nordic
6. Concrete samples were manufactured using aggregates from ONKALO provided by Rudus Oy.
7. 3 different water compositions (ion-exchanged, saline bentonite porewater and simulated saline groundwater from ONKALO)

18.3 MODELLING

Modelling of EU Dopas samples

Thermodynamic modelling of EU Dopas experiments (Holt et al., 2016) was performed by using Gibbs energy minimization simulation method for calculating chemical equilibria in the experimental system. The software used was GEMS- Selektor v.3, developed by Paul Scherrer Institut. Suppelementary database CEMDATA14 was used for cementitious materials together with PSI-Nagra database. GEMS –Selektor software and CEMDATA14 –database have been widely used in cement and concrete research. GEMS-Selektor was chosen at this phase of the project because CEMDATA 14 database was already built-in the modelling software.

Pore solution pH of various CaO/SiO2 –ratio concretes were determined. Three water types were used. Ion exchanged water represents the pore solution pH, whereas saline groundwater sample represents the pH in the vicinity of the concrete structure when the concrete is exposed to the groundwater. Saline bentonite porewater represents the situation in which the groundwater composition is in equilibrium with the bentonite materials. Modelling of the concretes was performed by adding the exact experimental compositions of the used cement together with the used solutions to the model and thus modelling the pore solution compositions. Results of pore solution pH are presented in Figure 18.1.

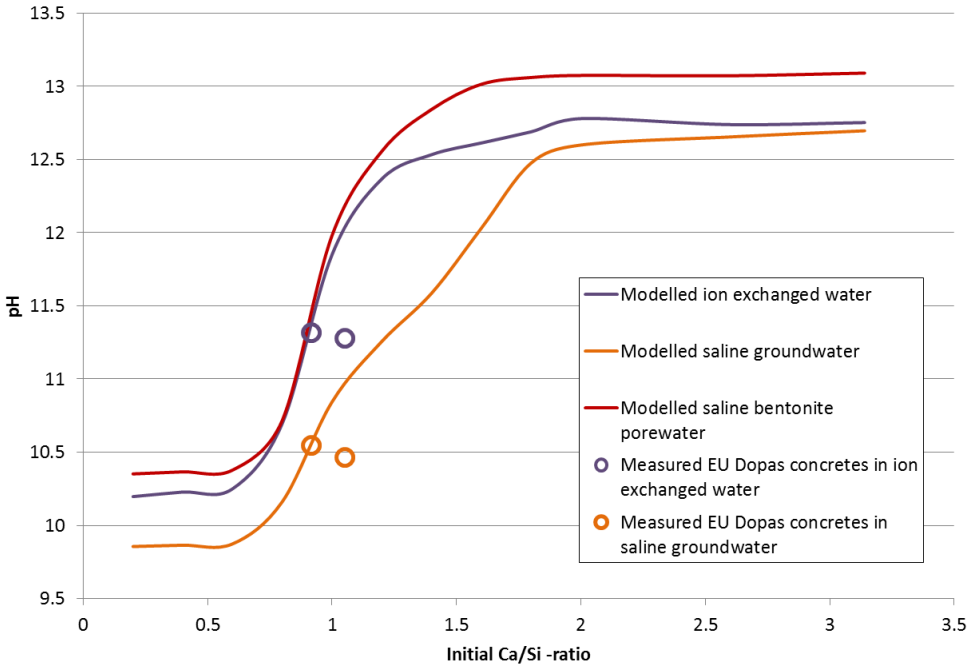

Figure 18.1. *Experimental and modelled pore solution pH of accelerated paste Samples on different water types.*

Modelling of Leaching experiments

Leaching experiments are still ongoing. The modelling of these was performed in a stepwise manner. The exact compositions of the leaching samples were modelled and the resulting solid phases were used as an input values for next leaching step. Selected method enabled comparison between modelled and measured values because the leaching processes in both cases were identical. The modelling and Leaching results can be seen in Figure 18.2.

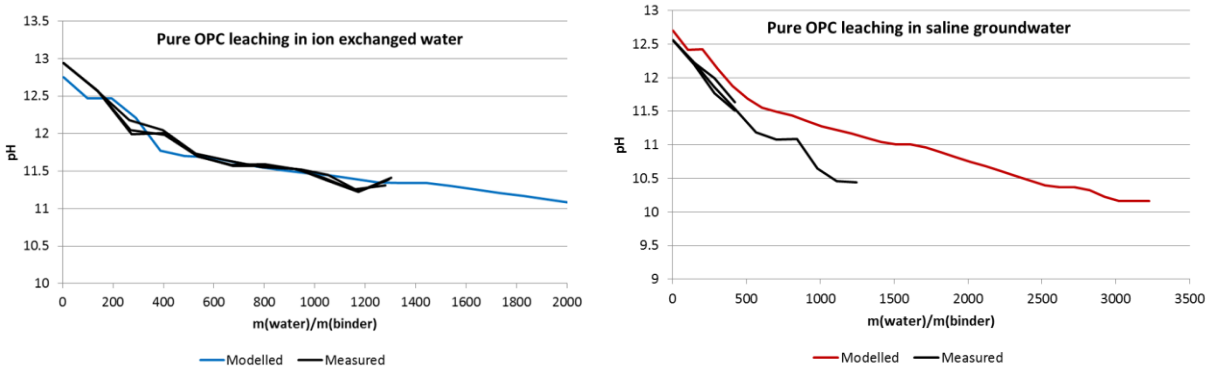

Figure 18.2. *Modelled and measured leaching of pure OPC in ion exchanged water and saline groundwater.*

Equilibrium calculations of leachate bentonite interaction with varying leachate/bentonite ratios

The results from the third modelling exercise were presented in Davos Clay conference. The leachate compositions were results from an experiment between saline groundwater and cementitious materials interaction with varying CaO/SiO_2 -ratios from 3.14 to 0.4 in equilibration. The results from an experiment having groundwater/binder ratio of 1 can be seen in Figure 18.3 and more info about the experiments can be found from (Vehmas et al., 2017).

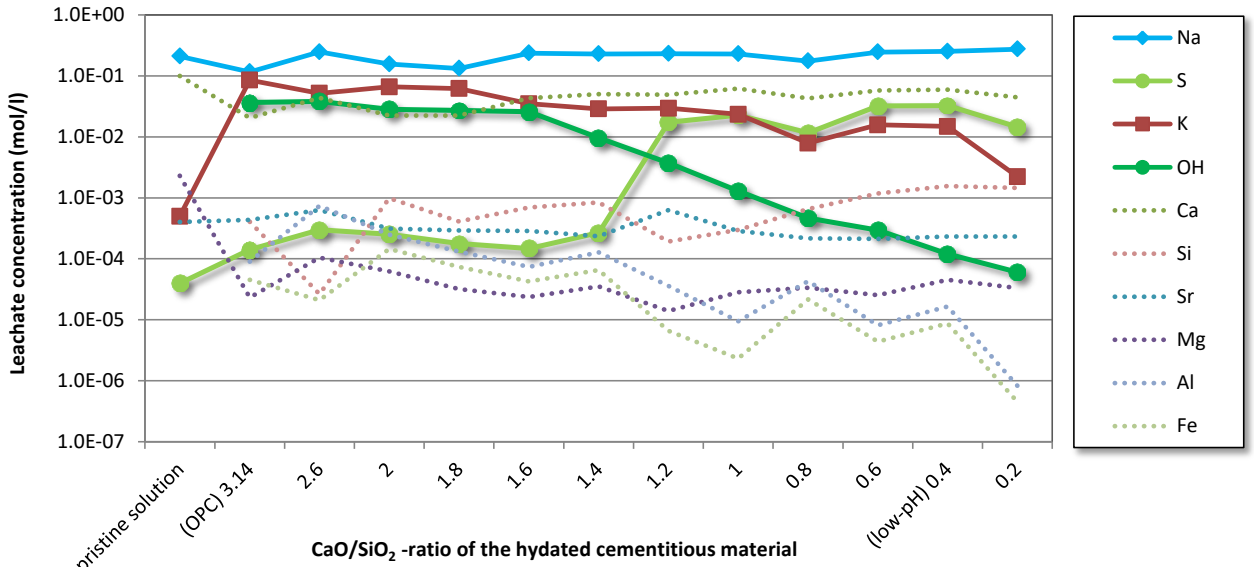

Figure 18.3. *Cementitious materials leachate composition at various CaO/SiO2 –ratios at saline groundwater. Groundwater to binder -ratio of the samples was 1.*

Ca/SiO_2 -ratios 3.14 and 0.4 were chosen as the modelling cases since they present a traditional Portland cement and "low-pH" alternative. The modelling was performed using PHREEQC and Thermoddem database. The model was calibrated using experimental samples to determine the active species and solid components that are relevant to leachate/MX-80 bentonite interaction. The experiments used in the calibration were taken from Heikola et al. (2013). Correlation between calibrated model and experimental samples was good, having correlation R=0.9999. Modelling was performed as equilibrium calculation with 3.14 and 0.4 CaO/SiO_2 -ratios chosen as relevant test cases and mass of leachate/mass of bentonite ratio chosen as variable.

The results are shown in Figure 18.4 and 18.5. The results seem to indicate that the main mechanism of MX-80 bentonite degradation caused by cementitious leachates would not be dissolution in long-term but the leachates from Portland cement would cause MX-80 to transform to cementitious reaction products, mainly calcium-silicate-hydrates. The transformation was complete as leachate/bentonite -ratio of 500 with pristine Portland cement based leachates. Low pH alternative did not cause major changes in bentonite content but formation of gypsum was observed. The modelling results in low pH and 0.4 -ratio indicate that the leachates interaction would not dissolve the clay based buffer materials but the forming of secondary reaction products will densify the bentonite structure and clog the initial porosity of buffer and backfill material.

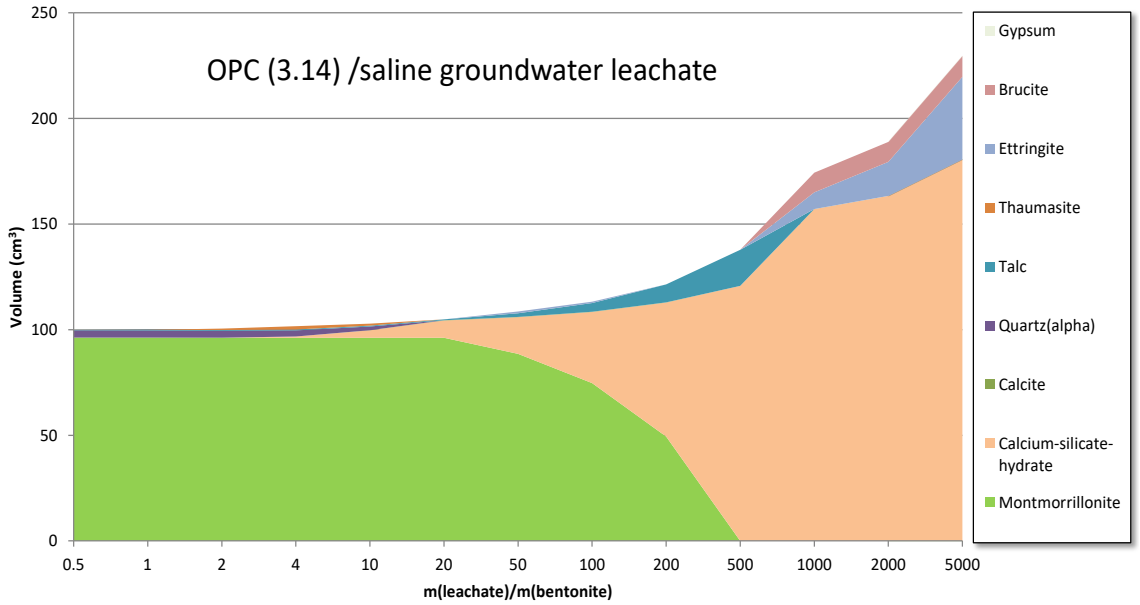

Figure 18.4. *Modelled solid compositions of Portland cement/saline groundwater –leachate and MX-80 bentonite with various leachate/bentonite –ratios.*

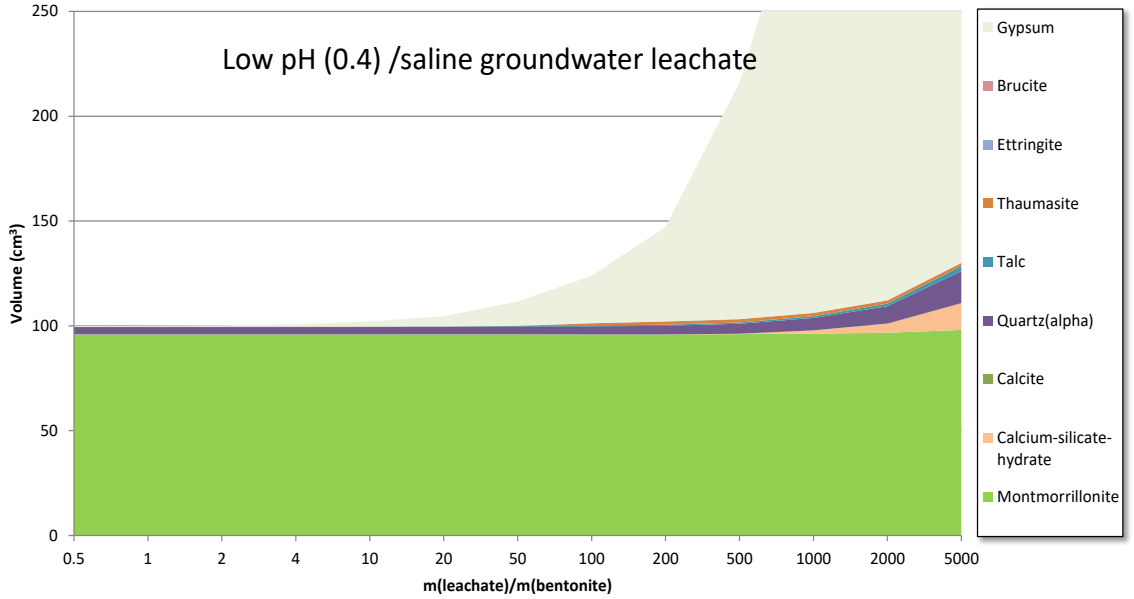

Figure 18.5. *Modelled solid compositions of low–pH cement/saline groundwater –leachate and MX-80 bentonite with various leachate/bentonite –ratios.*

18.4 DISCUSSION AND CONCLUSIONS

There are unsettled questions regarding to the nature of the CSH gel and reliability of thermodynamic modelling. These questions may not get the final answer in the current project but their effect on the uncertainty of the results can be determined. High C/S –ratio CSH is either in nanocrystalline form of defect tobermorite or jennite. Although the exact nature of CSH form is not known, both of these forms are in equilibrium with solid portlandite which determines the pH at the high C/S –ratios. C/S –ratios below 0,6, the CSH is either solid solution of tobermorite and silica or low C/S –ratio CSH. The exact nature of CSH at low C/S –ratios in not a necessity to know because the pH of the low C/S –ratio CSH can be experimentally obtained.

There are also uncertainties related to the applicability of thermodynamic modelling. For example, some databases use ion activity products which are poorly applicable or will cause errors to highly concentrated solutions above 0.1 molarity. Thermodynamic modelling should be therefore

performed with a conservative approach, so that the amount of modelled hydroxyl ions is always equal or greater than the measured values. According to the first modelled leaching results, the selected modelling method seems to do that naturally. Modelled and measured leaching of pure OPC paste in ion-exchanged water has good correlation. As the water is changed to more saline, the modelled pH values become greater than the measured values. According to first results, the difference originates from precipitating phases. As equilibrium modelling assumes that each phase is in fully equilibrated, the measured values have not reached full equilibrium. This tends to lower the solubility of the phases in modelled leaching and causes higher pH values compared to the measured values. Thus, kinetics should be included in the leaching models.

Acknowledgements

The research leading to these results has received funding from the European Union's Horizon 2020 Research and Training Programme of the European Atomic Energy Community (EURATOM) (H2020-NFRP-2014/2015) under grant agreement n° 662147 (CEBAMA).

18.5 REFERENCES

Cau Dit Coumes C., Courtois S., Nectoux D., Leclercq S., Bourbon X. (2006). Formulating a low-alkalinity, high-resistance and low-heat concrete for radioactive waste repositories. Cem. Concr. Res., 36(12), 2152–2163.

Heikola T., Kumpulainen S., Vuorinen U., Kiviranta L., Korkeakoski P., (2013). Influence of alkaline (pH 8.3-12.0) and saline solutions on chemical, mineralogical and physical properties of two different bentonites. Clay Minerals, 48, 309-329.

Holt E., Koho P. (eds.) (2016). DOPAS Deliverable D4.5 POPLU Experimental Summary Report. 170 p. available from http://www.posiva.fi/en/dopas/deliverables.

Holt E., Leivo M., Vehmas T. (2014). Low-pH concrete developed for tunnel end plugs used in nuclear waste containment. In Concrete Innovation Conference (CIC 2014), 11-13 June, Oslo, Norway.

Martino J., Dixon D., Holowick B., Kim C.-S. (2011). Enhanced sealing project (ESP) Seal Construction and Instrumentation. NWMO report.

Savage D. (2007). Low pH Cements, SKI Report 2007:32.

Vehmas T., Leivo M., Holt E., (2017). Comparison of experimental and modelled pore solutions of low-pH Ordinary Portland Cement based mix designs. Proceedings of the 2nd annual Cebama workshop.

Vogt C., Lagerblad B., Wallin K., Baldy F., Johansson J.-E. (2009). Low pH self compacting concrete for deposition tunnel plugs. Swedish Nuclear Fuel and Waste Management Co. SKB report R-09-07.

20 LML/ C. Gong, Z. Liu, X. Chen, S. Xie, J. Shao

Abstract

In this study, we shall investigate the hydromechanical behaviour of interfaces between claystone and concrete in the context of geological disposal of radioactive waste. A series of triaxial shear tests are first performed under different values of confining stress and water pore pressure. The tested samples are composed of a semi-cylinder of claystone and a semi-cylinder of concrete. The concrete is directly cast beside the claystone and bonded interfaces between two materials are obtained. The shear strength of interfaces is then determined. The effect of water pore pressure on the shear strength is identified by a generalized effective stress concept. Based on the experimental data, we shall propose an elastic-plastic model for the description of stress-strain relations of interfaces. After the calibration of model's parameters, the proposed model is applied to the laboratory shear tests. Numerical results are compared with experimental data and a good agreement is obtained.

20.1 INTRODUCTION

Geological disposal is considered as an efficient way for the management of high-level radioactive waste. In the French concept of disposal, the waste canister is stored in deep underground units confined by a double barrier system that consists of the engineering barrier and the geological barrier. The engineering barrier is made up of artificial materials including the high performance (HP) concrete and the geological barrier refers to the Callovo-Oxfordian (COx) claystone. Two barriers will form interfaces of different shapes. Those interfaces may constitute weak zones which affect the confining capacity of underground disposal facilities. Mechanical properties of the COx claystone and the HP concrete have widely been investigated in various previous studies. The mechanical behaviour of claystone/concrete interfaces is still an open issue.

The COx claystone is quite different from clays or clay soils in mineralogy, texture structure, as well as physical and mechanical properties. As a hard rock, the COx claystone cannot be remoulded as what has been widely done for clay soils in laboratory studies. Interfaces between the soils and the concrete are made mostly at present by compaction of the crushed soil particles onto the surface of the premade concrete blocks. There are no interface cementation processes between the soils and the concrete. Under repository conditions, the geological barrier, i.e. the COx claystone, is pre-existing. The concrete lining or plug is poured in a slurry form onto the surface of the claystone. Hence, the interfaces between the COx claystone and concrete are very different from those between the soil and concrete ones (Hossain and Yin, 2014; Chen at al., 2015). The method for fabricating samples of soil and concrete interface is no longer valid for making the interface samples between the COx claystone and the HP concrete.

Therefore, contributions are needed to develop new techniques for making interface samples and further to evaluate the performance of the interfaces between these two materials. There are so far some discussions on mechanical properties of contact interfaces between clay soils and concrete (Stavropoulou et al., 2018) or interfaces between non-water-sensitive rock and concrete (Buzzi et al. 2008; Kosakowski and Berner, 2013; Flansbjer and Magnusson 2014; Dong and Zhu 2016; Mader et al., 2017). In González-Santamaría et al. (2015), interactions between low-pH cement mortar and bentonite have been studied in a small-scale pilot laboratory experiment. Clay Miner. 2018; 53(2): 237-254. In those previous studies, two materials were just put together without bonding at the interface. The bonded interface between the claystone and the concrete has been rarely characterized and very few quantitative evaluations are so far available.

In the framework of the project CEBAMA, our principal objective is to improve the current knowledge on mechanical and hydromechanical behaviour of interfaces between claystone and HP concrete. The present study is composed of two parts. In the first part, a series of new laboratory tests will be performed in order to characterize the deformation and mechanical strength of the interface. In the second part, we shall propose a constitutive model to describe the hydromechanical behaviour of interface. The proposed model will be evaluated against the experimental data.

20.2 EXPERIMENTS PERFORMED AT UNIVERSITY OF LILLE

We have carried out triaxial direct shear tests on interface samples under different values of confining pressure and injected water pressure in a specifically designed experimental device. Each of the interface samples is composed of two semi-cylinders. The first one is made of COx claystone and the other one of a low-pH high performance concrete. The compositions of the concrete are presented in detail in Leung et al. (2015) and Bernard et al. (2018). The semi-cylinder COx claystone is previously prepared and placed into one side of a cylindrical stainless-steel mold. The concrete is directly cast into the other side of the cylindrical mold, beside the COx claystone. With the help of the casting procedure proposed in this study, we have obtained good quality cylindrical samples including planar interfaces between the claystone and the HP concrete, as shown in Figure 20.1. One can observe that the two materials have an apparent boundary at the interface and at the same time they are well bonded together after concrete hardening and curing.

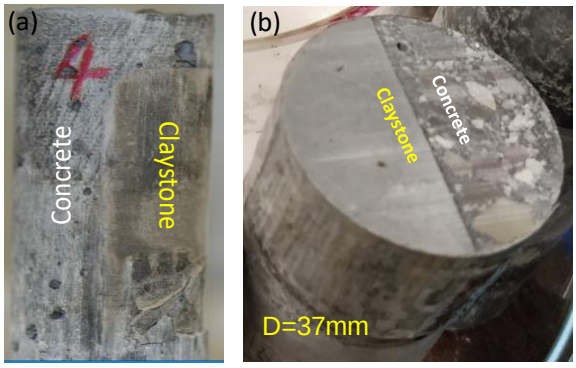

Figure 20.1. *Image of samples including well-bonded planar interface between COx claystone and concrete: (a) sample during concrete curing; (b) sample before test.*

The confining pressure used ranges from 2MPa to 12MPa while the injected water pore pressure varies from 1MPa to 4MPa. The specific values of confining stress and pore pressure are chosen such that their difference is the same between a pair of tests respectively with and without injection water pressure. The objective is to investigate the effect of pore pressure on the shear strength of the interface and to check the validity of the effective stress concept for the interface.

The representative stress-strain curves are shown in Figure 20.2 for the test with a confining pressure of 12 MPa and an injected water pressure of 4 MPa. In Figure 20.2(a), there is a nonlinear relation between the shear strain and shear stress even during the first stage of loading. The radial strain corresponds to the relative diameter change of sample ($\Delta D/D$) or the opening/closure of the interface. Negative values denote closure. The radial strain remains very small during the first stage of shearing. It means that the shear stress does not induce significant interface opening or closure when it is less than some critical threshold. After that threshold, the negative radial strain increases rapidly. The shear stress induces a significant closure of the interface, probably due to the degradation of asperities in the interface zone.

The image of the tested sample is presented in Figure 20.2(b). One can see that the two semi-cylinders are clearly slipped with respect to each other, but the two parts still hold together due to

the induced compaction of the interface. The two surfaces of the tested sample are shown in Figure 20.2(c). We can clearly observe frictional traces of shearing on the two surfaces. In addition, claystone powder is found on the sheared surfaces of both semi-cylinders, due to the fact that the claystone is much weaker and more sheared than the concrete. Some claystone powder can also be pushed into concrete pores, leading to a decrease of the permeability of the interface zone.

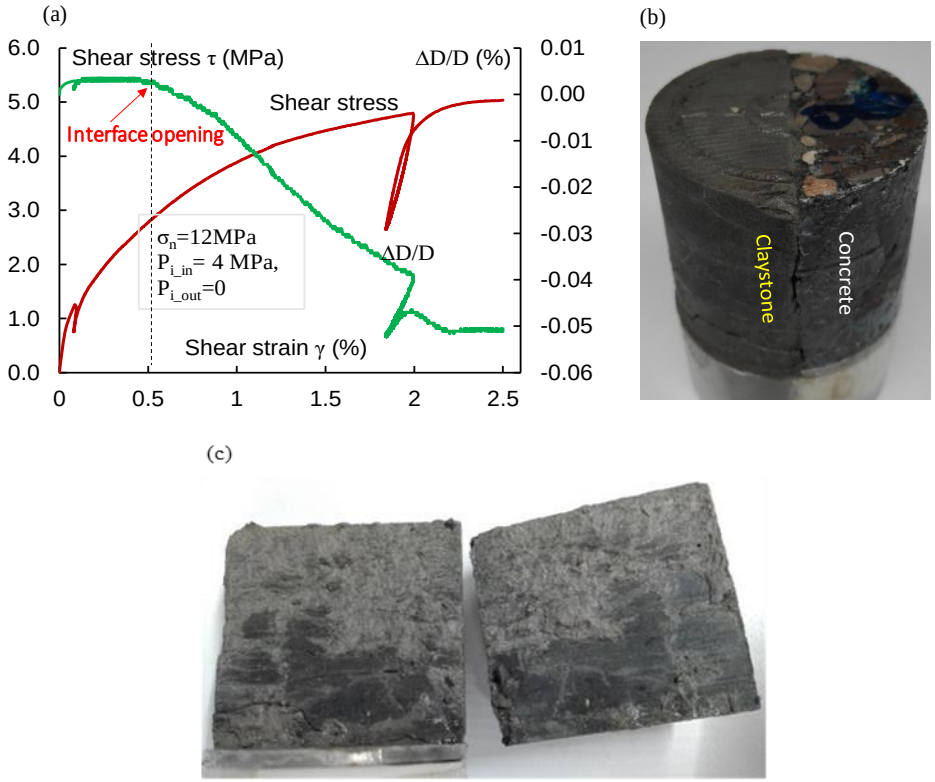

Figure 20.2. *(a) Mechanical responses of an interface sample during direct shear under confining pressure of 12 MPa with water injection pressure of 4 MPa; (b) Sample overview after test; (c) Sheared interface surface.*

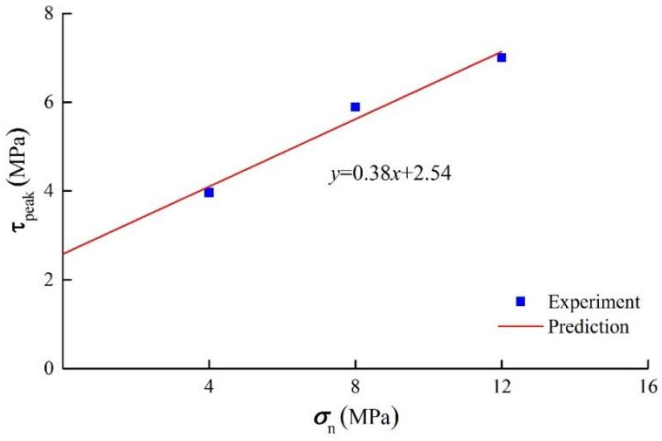

Figure 20.3. *Peak strength surface of interface samples under direct shear tests.*

The values of the peak shear stress obtained from the direct shear tests are presented in Figure 20.3. It is found that a linear Mohr-Coulomb type criterion can be adopted for the description of shear strength of the interface, except for the test performed without normal stress (simple shear test). For the case of saturated samples with water pressure, it is found that the shear strength of the interface can be described by a generalized effective normal stress. The average effective stress coefficient

for the studied interfaces is about 0.75. The classical Terzaghi's effective stress is not valid for these interfaces.

The water permeability of the interface samples is also estimated by injection of the synthetic water that has the similar chemical compositions than that of in situ ground water of the COx layer. Due to the ultra-low permeability of the interface sample, the saturation and permeability measurement lasts several months. It is found that the permeability of the interface sample is at the magnitude of $10^{-20}m^2$. This value is similar to the permeability of the intact COx claystone and of the high-performance concrete. This means that the initial interface does not represent a weak zone of permeability. In addition, the interface permeability increases up to 50% when the normal stress is increased to 12MPa.

20.3 MODEL FORMULATION

Based on the experimental data, the mechanical behavior of claystone/concrete interface is described by an elastic-plastic model. The deformation of the interface is characterized by its normal strain (opening or compaction) and shear strain. The assumption of small strains and the classical additive decomposition of strain are here adopted. The total strain increment is then decomposed into an elastic and a plastic part:

$$\begin{cases} d\varepsilon_n = d\varepsilon_n^e + d\varepsilon_n^p \\ d\varepsilon_t = d\varepsilon_t^e + d\varepsilon_t^p \end{cases} \tag{20.1}$$

$\varepsilon_n$denotes the total normal strain, ε_n^e the elastic normal strain and ε_n^p the plastic normal strain; ε_t is the total shear strain, ε_t^e the elastic shear strain and ε_t^p the plastic shear strain. The incremental stress-strain relations can be written as:

$$\begin{cases} d\sigma_n - \chi dp = K_n\left(d\varepsilon_n - d\varepsilon_n^p\right) \\ \quad d|\tau| = K_t\left(d\varepsilon_t - d\varepsilon_t^p\right) \end{cases} \tag{20.2}$$

σ_n and τ are respectively the normal stress and shear stress. K_n and K_t respectively denote the normal and tangential elastic stiffness of interface. It is noted that these elastic coefficients can be functions of normal stress. For saturated interfaces, the pore fluid pressure has an influence on the plastic deformation. Based on the experimental data issued from shear tests with injected water pressure, the concept of effective stress is here generalized. The plastic deformation is driven by an effective normal stress defined by $d\sigma_n^{ep} = d\sigma_n - \chi dp$, with χ being the effective stress coefficient.

Plastic strains are described by the definition of a plastic yield function, a plastic potential and a plastic hardening law. Based on the experimental shear peak stresses shown in Figure 20.2, it appears convenient to use a linear Mohr-Coulomb type criterion for the plastic yield function:

$$F = |\tau| - tan\,\phi\,\sigma_n^{ep} - C \leq 0 \tag{20.3}$$

ϕ and C denote the frictional angle and the cohesion of the interface. According to the experimental data from triaxial shear tests, the friction angle increases with plastic shear strain while the cohesion remains nearly constant. Therefore, the plastic hardening is described by the evolution of frictional angle with the accumulated plastic shear strain. The following hardening function is proposed:

$$\phi = \phi_m - (\phi_m - \phi_0)e^{-a\bar{\varepsilon}_t^p}\ ,\ \bar{\varepsilon}_t^p = \int\left|d\varepsilon_t^p\right| \tag{20.4}$$

ϕ_0 and ϕ_m are respectively the initial and asymptotic values of the frictional angle. $\bar{\varepsilon}_t^p$ is the accumulated plastic shear strain. The parameter *a* controls the rate of plastic hardening.

In order to properly describe the normal plastic strain induced by shear stress, a non-associated plastic flow rule is here proposed. The following plastic potential is given by:

$$G = |\tau| - \beta\sigma_n^{ep} \tag{20.5}$$

The parameter β defines the ratio between the plastic normal strain rate and plastic shear strain rate as follows:

$$\begin{cases} d\varepsilon_n^p = d\lambda \frac{\partial G}{\partial \sigma_n^{ep}} = \beta d\lambda \\ d\varepsilon_t^p = d\lambda \frac{\partial G}{\partial |\tau|} = d\lambda \end{cases} \text{ if } F = 0 \text{ and } \dot{F} = 0 \tag{20.6}$$

The plastic multiplier $d\lambda$is determined by the following plastic loading-unloading conditions:

$$d\lambda \geq 0\,,\, F \leq 0\,,\, d\lambda F = 0 \tag{20.7}$$

In three-dimensional loading conditions, the shear stress on the interface is defined by the vector $\vec{\tau}$. Accordingly, the plastic shear strain is given by the vector $d\vec{\varepsilon}_t^p$. Its direction is co-axial to that of the shear stress vector $\vec{\tau}/|\vec{\tau}|$.

On the other hand, from Figure 20.2, it is seen that the normal plastic strain remains very small when the shear stress is less than some critical value. It seems that there is a characteristic threshold at which the normal plastic strain (interface opening or compaction) becomes significant. Based on this observation, in the present study, we assume that the parameter β is equal to zero when this threshold is not reached. After that the value of β varies with the accumulated plastic shear strain:

$$\beta = ln(\, b\langle \bar{\varepsilon}_t^p - \bar{\varepsilon}_t^{pc} \rangle)\ ,\ \bar{\varepsilon}_t^p = \int \left| d\varepsilon_t^p \right| \tag{20.8}$$

$\bar{\varepsilon}_t^{pc}$ is the critical plastic shear at the plastic normal onset threshold, and b is the parameter controlling the evolution rate of β.

20.4 MODEL CALIBRATION AND VERIFICATION

The parameters involved in the proposed model can be easily identified from the laboratory tests performed within WP1 and presented above. The elastic stiffness coefficients K_n and K_t are first determined from the linear part or the unloading part of stress-strain curves obtained respectively in a normal compression test and a direct shear test with or without confining stress. The asymptotic value of frictional angle ϕ_m and the cohesion C together define the failure surface of interfaces. Their values can be determined from the best fitting of peak shear stresses obtained in shear tests with different confining stresses or normal stresses. The comparison between the theoretical failure locus and experimental data is presented in Figure 20.3. The initial value of frictional angle should be identified from the elastic limit stress obtained in shear tests. As shown in Figure 20.2, it seems that the elastic limit stress is very small and not easy to identify. For practical purposes, the influence of this parameter on plastic deformation is not very important and a small value can be adopted. The plastic hardening parameter a is calibrated by the optimal fitting of the shear stress versus shear strain curve in a direct shear test. Finally, the values of three parameters involved in the plastic potential (β_0,β_m,b) are obtained from the optimal fitting of the radial strain versus shear strain curve. For the interfaces studied here, the set of parameters obtained are given in Table 20.1. It is found that the shear elastic stiffnessK_t, the plastic hardening parameter a, as well as the parameter controlling the interface normal deformation, b, vary with normal stress. For a detailed description of these evolutions, it is needed to perform additional tests in future.

Using these parameters, triaxial shear tests under different normal stresses are simulated with the help of the proposed model. Numerical and experimental results are compared in Figures 20.4 to

20.6 for three values of normal stress. It seems that the proposed model well reproduces the mechanical response of claystone/concrete interfaces under triaxial shear conditions.

Table 20.1. *Set of parameters for claystone/concrete interface.*

σ_n /MPa	τ_{peak} /MPa	a	φ_0 /°	φ_m /°	K_t	b
4	3.9642	1200	0	20.81	360	24
8	5.8899	340	0	20.81	480	0.95
12	7.0038	130	0	20.81	480	0.26

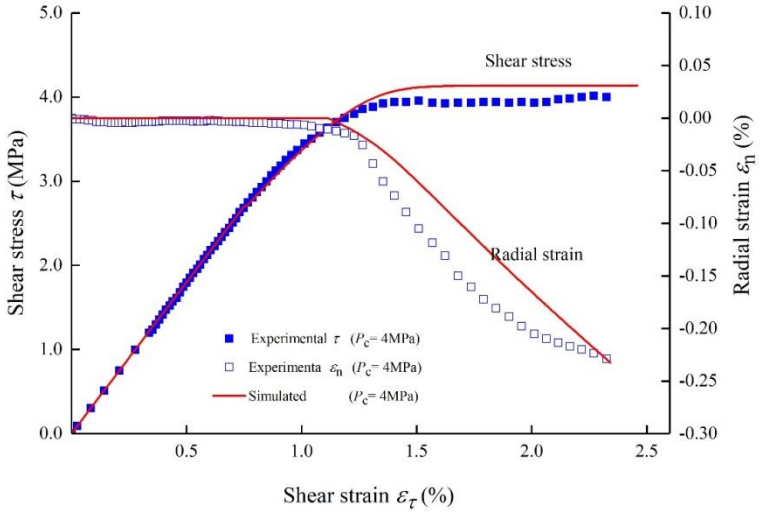

Figure 20.4. *Evolution of shear and normal strains versus shear stress in the test under the normal stress of 4MPa.*

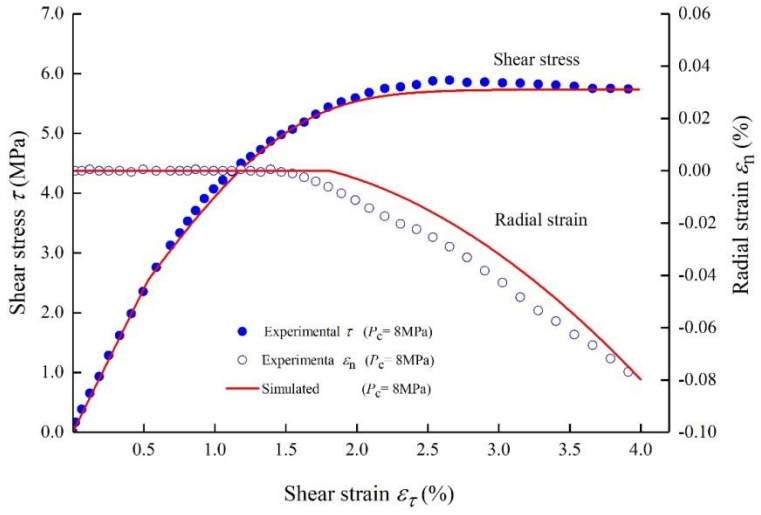

Figure 20.5. *Evolution of shear and normal strains versus shear stress in the test under the normal stress of 8MPa.*

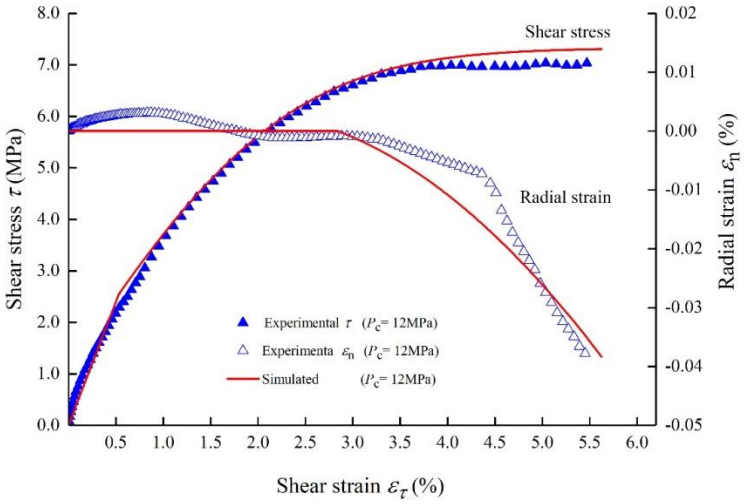

Figure 20.6. *Evolution of shear and normal strains versus shear stress in the test under the normal stress of 12MPa.*

20.5 CONCLUSIONS AND OUTLOOK

In this study, the hydromechanical behavior of an interface between COx claystone and low-pH high performance concrete has been investigated. A series of triaxial shear tests have been performed. The shear strength of the interface is quasi linearly dependent on the normal stress. The effect of fluid pore pressure can be captured through an effective normal stress and the related effective stress coefficient, which is a priori less than 1. Under shear stress, the interface exhibits an important plastic shear strain and normal strain. The plastic normal strain is mainly compressive corresponding to the plastic compaction of the interface. Based on experimental data, we have developed an elastic-plastic model with the plastic shear hardening and a non-associated plastic potential. The proposed plastic model is able to reproduce all main features of mechanical behaviour of the interface under triaxial shear conditions. The proposed model should be extended in future to include the permeability evolution of the interface as a function of normal plastic strain which corresponds to the interface opening or compaction, in particular in the post-failure regime. Finally, the proposed model can be implemented in the computer code in view of calculation of structures of disposal facilities.

Acknowledgements

The research leading to these results has been jointly funded by the European Union's Horizon 2020 Research and Training Programme of the European Atomic Energy Community (EURATOM) (H2020-NFRP-2014/2015) under grant agreement n° 662147 (CEBAMA), and the French Agency for radioactive waste management (ANDRA).

20.6 REFERENCES

Bernard E, Dauzères A, Lothenbach B. (2018). Magnesium and calcium silicate hydrates, Part II: Mg-exchange at the interface “low-pH” cement and magnesium environment studied in a C-S-H and M-S-H model system. Applied Geochemistry, 89, 210-218.

Buzzi O, Boulon M, Hervé M, Su K. (2008). Leaching of rock-concrete interfaces. Rock Mech Rock Eng. 41(3), 445-466.

Chen X, Zhang J, Xiao Y, Li J. (2015). Effect of roughness on shear behavior of red clay – concrete interface in large-scale direct shear tests. Can Geotech J., 52(8), 1122-1135.

Dong W, Wu Z, Zhou X. (2016). Fracture Mechanisms of Rock-Concrete Interface: Experimental and Numerical. J Eng Mech., 142(7), 04016040.

Flansbjer M, Magnusson J. (2014). System design of Dome plug - Mechanical properties of rock-concrete interface. Stockholm: SKB Report P-13-38, Svensk Kärnbränslehantering AB.

González-Santamaría DE, Angulo M, Ruiz AI, Fernández R, Ortega A, Cuevas J. (2018). Low-pH cement mortar-bentonite perturbations in a small-scale pilot laboratory experiment. Clay Miner., 53(2), 237-254.

Hossain MA, Yin J-H. (2014). Behavior of a Pressure-Grouted Soil-Cement Interface in Direct Shear Tests. Int J Geomech., 14(1), 101-109.

Kosakowski G, Berner U. (2013). The evolution of clay rock/cement interfaces in a cementitious repository for low- and intermediate level radioactive waste. Phys Chem Earth., 64 (Sup. C), 65-86.

Leung Pah Hang T. (2015). Les bétons bas pH : comportements initial et différé sous contraintes externes. Laboratoire Matériaux et Durabilité des Constructions de Toulouse. Doctorat. Université Toulouse 3 Paul Sabatier (UT3 Paul Sabatier).

Mäder U, Jenni A, Lerouge C, et al. (2017). 5-year chemico-physical evolution of concrete–claystone interfaces, Mont Terri rock laboratory (Switzerland). Swiss J Geosci., 110(1), 307-327.

Stavropoulou E, Briffaut M, Dufour F, Camps G. (2018). Experimental Characterisation of the Mechanical Properties of the Clay-Rock/Concrete Interfaces and Their Evolution in Time. In: Arzoumanidis A, Silberstein M, Amirkhizi A, eds. 2017 Annual Conference on Experimental and Applied Mechanics. Cham: Springer International Publishing, 1-3.

Yang H., Xie S.Y., Secq J., Shao J.F. (2017). Experimental study and modeling of hydromechanical behavior of concrete fracture, Water Science and Engineering 10(2): 97-106.

24 PSI/ G. Kosakowski (PSI), L. Hax Damiani (PSI, Univ. Bern)

ABSTRACT:

In WP3 of the CEBAMA project PSI is involved in developing a reactive transport framework that makes it easier to investigate the electrochemical transport in porous media, such as cementitious materials or clays. We validated the approach with experimental data similar to those from Glaus et al. (2015). In addition, we present results from a modelling study on cement-clay interaction on a low-pH – Opalinus Clay interface investigated in the framework of the Mont-Terri CI experiment and in WP1 of CEBAMA. We show that consideration of cement hydration in the reactive transport model - with an approach also used for description of the hydration of the CEBAMA reference mix – is needed for reproduction of major experimental findings.

24.1 INTRODUCTION

In the planned Swiss repository, design cement and clay materials are essential parts of the engineered barrier system (Kosakowski and Berner, 2013). To be able to predict or reconstruct the spatial and temporal evolution of such systems, reactive transport codes are commonly applied (Steefel et al., 2005). There is a variety of different codes available, and each one has specific advantages and limitations (Steefel et al., 2015).

Within the CEBAMA project, we developed a new reactive transport framework FENICS-Reaktoro that allows modeling reactive transport processes in a more versatile way. We furthermore used OpenGeoSys-GEM and the new framework to model different aspects in the evolution of cement-based materials:

- the electrochemical coupling of solutes migrating in porous media with and without the presence of charged surfaces,
- the hydration of CEBAMA reference mix,
- and the evolution of a low-pH cement (ESDRED) in contact with Opalinus Clay on data from the Mont Terri CI experiment (Jenni et al., 2014), which is the focus of the work conducted by the Uni Bern group in WP1.

24.2 ELECTROCHEMICAL TRANSPORT

For the modelling of electrochemically coupled transport, we use our newly developed reactive transport framework FEniCS-Reaktoro. It allows to model reactive electrochemical mass transport in saturated porous media. It combines two state-of-the art simulation codes for solution of partial differential equations and for calculation of chemical equilibria. We implemented the sequential non-iterative approach (SNIA) for coupling transport (FEniCS) and chemical solvers (Reaktoro).

FEniCS (Alnæs et al., 2015) is a Finite Element library that offers an intuitive math-alike scripting interface that allows one to set up the physical processes directly by defining the partial differential equation easily and straightforwardly. Reaktoro (Leal et al., 2017) is a chemical solver that combines advantages of existing law of mass action (LMA) and Gibbs Energy Minimization (GEM) solvers to speed up the equilibrium calculation. Reaktoro also allows definition of chemical problems by using GEMS (Kulik et al., 2013) and Phreeqc (Parkhurst and Appelo, 2013) files as input.

We implemented the so-called Poisson-Nernst-Planck system of equations in its weak form:

$$\int_\Omega \frac{\Delta c}{\Delta t} \cdot V_i dx = \int_\Omega \left(-D_i \nabla c_i - \frac{z_i D_i F\, c_i}{RT}\, \nabla \phi\right) \cdot \nabla V_i \, dx \tag{24.1}$$

$$\int_\Omega \nabla \phi \cdot \nabla V_\phi dx - \frac{F}{\epsilon} \int_\Omega \left(\sum_{i=1}^{Ns} z_i c_i\right) \cdot V_\phi dx = 0 \tag{24.2}$$

where c is the concentration, Δt is the time step, V is the test function, D is the diffusion coefficient, z is the charge, F is the Faraday constant, R is the gas constant, T is the temperature, ϕ is the electric potential, and ϵ is the dielectric constant.

To analyse the effect of the electrochemical migration during the diffusion of ions, we model an experiment conducted at PSI to measure the flux of charged species between two reservoirs, similar to Glaus et al. (2015). The experimental setup consists of two reservoirs separated by a cellulose acetate membrane. Both tanks contain a solution with KCl and HNO_3. A volume adjustment factor is introduced into the weak formulation to take into account the different cross-sectional areas and volumes of the membrane and the reservoirs. The membrane porosity is 0.44, the diameter is 23 mm and the width is 0.13 mm. The domain is discretized into 29 cells and the volume adjustment factor for the membrane cells is 4.156e-4. A neutral species (HTO) was added as a non-sorbing tracer in one reservoir.

Figures 24.1 and 24.2 present the evolution of the concentration in each reservoir over time. The initial concentrations in the reservoirs and the diffusion coefficients in water are given in Table 24.1. In the experiment, fluxes of K^+ and Cl^- are measured during the course of the experiment even though there is no initial concentration gradient present. This so-called "uphill fluxes" are created because of the different mobilities of the ions involved. The electrochemical fluxes of K^+ and Cl^- are triggered by the HNO_3 concentration gradient imposed at time zero. The diffusion of H^+ and NO_3^- with different diffusion coefficients induces additional fluxes of K^+ and Cl^- to maintain the charge balanced at all times.

It is possible to see a good agreement between our results, other codes and experimental data. The electromigration term fully controls the transport phenomena observed in this model and, therefore, the traditional Fickian approach is not suitable for describing adequately the short-term fluxes in such setups.

Table 24.1. *Chemical composition, diffusion coefficients and right and left reservoirs initial concentrations.*

Species	Diffusion Coefficient [$m^2\ s^{-1}$]	Concentration right reservoir [mol L^{-1}]	Concentration left reservoir [mol L^{-1}]
H^+	9.0×10^{-9}	0.001×10^{-3}	1.0×10^{-3}
NO_3^-	1.9×10^{-9}	0.001×10^{-3}	1.0×10^{-3}
K^+	2.0×10^{-9}	1.0×10^{-3}	1.0×10^{-3}
Cl^-	2.0×10^{-9}	1.0×10^{-3}	1.0×10^{-3}
HTO	2.3×10^{-9}	3.44×10^{-14}	1.0×10^{-3}

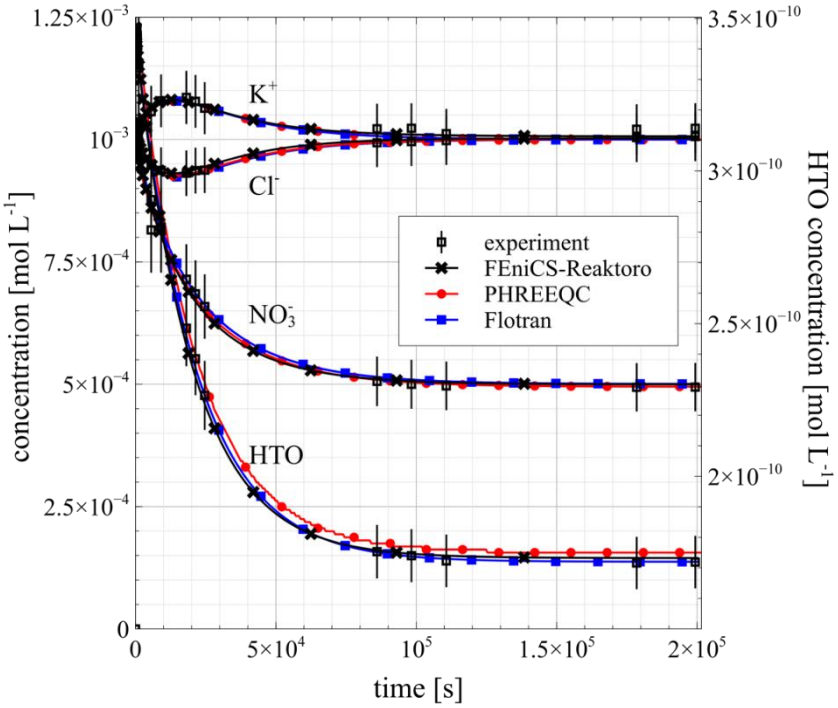

Figure 24.2. *Left upstream reservoir concentration evolution demonstrating the effect of charge coupling in the K^+ and Cl^- species.*

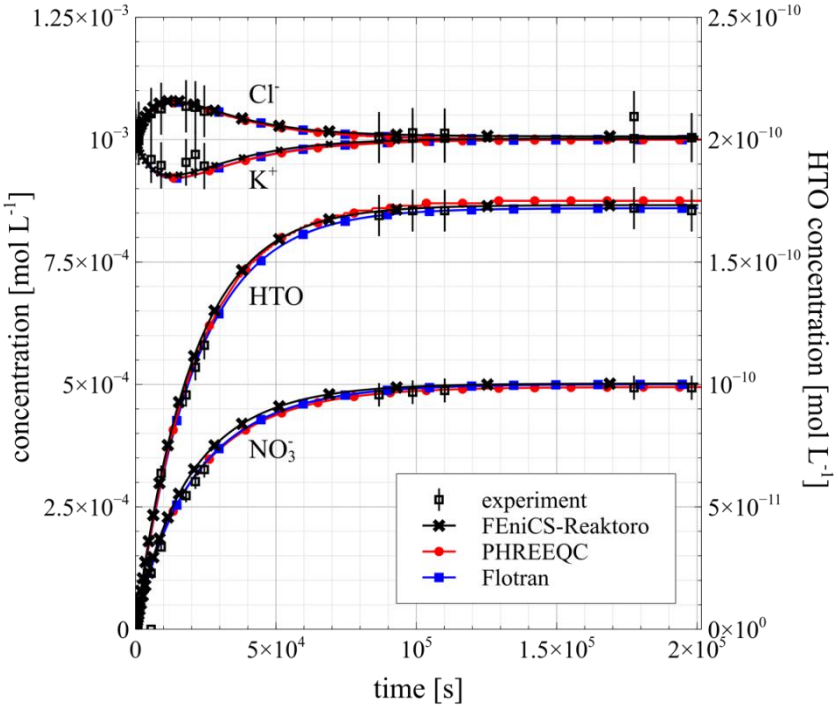

Figure 24.3. *Right downstream reservoir concentration evolution demonstrating the charge coupling in the K^+ and Cl^- species.*

24.3 HYDRATION OF THE CEBAMA REFERENCE MIX AND MODELLING OF CEMENT CLAY INTERACTION

For the WP3 Modelling Task benchmark study (Idiart et al., 2019), the initial state of the hardened low-pH concrete had to be calculated. For the CEBAMA reference mix no modelling study existed and detailed experimental data on the long-term hydration of the concrete were not available at the

time the Modelling Task was launched. Amphos 21 and PSI therefore conducted a modelling study on the hydration of the reference mix. While Amphos 21 modelled the system using the Thermochimie thermodynamic database (Giffaut et al., 2014) with Phreeqc, we used the scripting engine of GEM-Selektor V3 and the CEMDATA thermodynamic database (Lothenbach et al., 2019). Details regarding the calculations are reported in Idiart et al. (2019).

For enhancing our understanding of cement-clay interactions we did reactive transport calculations on results of the Mont Terri CI experiment (Jenni et al., 2014; Mäder et al., 2017). Unfortunately, the results of the study conducted by University of Bern in WP1 could not be integrated, as they were only available after calculations were finished.

The evolution of OPC and a low pH-concrete (ESDRED) in contact with the Opalinus Clay was modelled, as described in detail in Kosakowski (2018). Here, only a summary of the most important results related to the modelling of the ESDRED-Opalinus Clay interface is given.

The biggest difference between calculations for the Mont Terri CI experiment and the WP3 benchmarking study on clay/cement interaction is that for the specific setup of the CI experiment, where fresh concrete mixtures were poured into the boreholes, the explicit consideration of the cement hydration process in the reactive transport model was necessary for reproduction of most experimental observations.

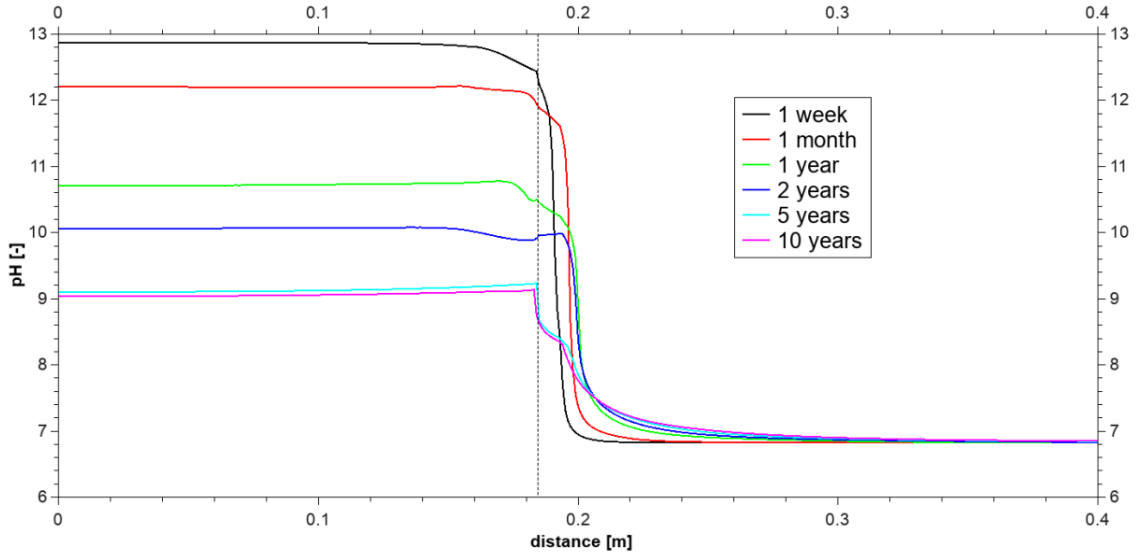

***Figure 24.3**. Modelled pH evolution with time at the ESDRED/OPA interface. The vertical line at x=0.1845 m indicates the position of the interface between ESDRED low-pH concrete (left) and Opalinus Clay (right).*

The thermodynamic setup and the modelling strategy for cement hydration follows the modelling study conducted by Barbara Lothenbach (Lothenbach, 2011a, 2011b) on laboratory experiments.

As an example of the influence of cement hydration, the calculated pH evolution across the concrete/clay interface is shown in Figure 24.3. The pH decreases considerably during the course of the modelled time span of 10 years. This is caused by the combined effect of cement hydration, the kinetically controlled dissolution of silica fume and the diffusive exchange of dissolved ions across the interface. Uptake of alkali ions (Na^+, K^+, Sr^{2+}) is implemented in the C-S-H model and helps to limit the otherwise high alkali concentrations in the concrete compartment. The measurements of Lothenbach (2011a) show a significant reduction of the alkali concentrations with time, which indicates a kinetically controlled uptake of alkali independent from the actual C-S-H formation process. Not considering such kinetic effects might influence alkali concentrations in the cement

pore waters and indirectly affects the pH evolution. In the actual field experiment, the cement hydration in the borehole is also influenced by diffusive exchange of alkalis and other solutes between cement and clay pore water (compare Figure 24.7).

The reactive transport models reproduce the main features reported in Jenni et al. (2014) and Mäder et al. (2017). This includes specifically the precipitation of ettringite and M-S-H in ESDRED near the interface that is visible in the modelled mineralogical profile after 5 years (Figure 24.4).

The Mg content of Opalinus Clay pore water will promote the conversion of C-S-H to M-S-H and to a lesser degree the formation of hydrotalcite ($MgCO_3 \cdot Fe/Al_2O_3 \cdot 5MgO$). Andreas Jenni (Univ. Bern) provided unpublished SEM-EDX point measurements from which the Mg/Si and Ca/Si ratios in Figure 24.5 were extracted. For comparison, modelled Mg/Si and Ca/Si ratios based on total elemental amounts per volume rock are superimposed. Although the reference model has a discretization which is relatively coarse in comparison to the altered zones, agreement is very good. The averaged EDX spot measurements do not necessarily correspond to the continuum-scale average composition used in the model, as selectively amorphous looking phases were probed, and obvious calcite or quartz grains were ignored. In order to mimic such biased measurements, the plot contains modelled element curves where the silica amount was corrected by removing silica from quartz and calcium was corrected with respect to calcite. This causes much better agreement for the Ca/Si ratio specifically in Opalinus Clay.

The ingress of sulfate SO_4^- causes the formation of ettringite and at very high sulfate concentrations, gypsum. The dissolution of AFm phases provides the aluminum required for ettringite formation. The precipitation/dissolution processes are linked to long-term changes in porosity, as shown in Figure 24.6. Experimental investigations of samples from CI experiments suggest porosity changes (Jenni et al., 2014; Mäder et al., 2017), but quantitative evaluations which can be compared to model results are not yet available.

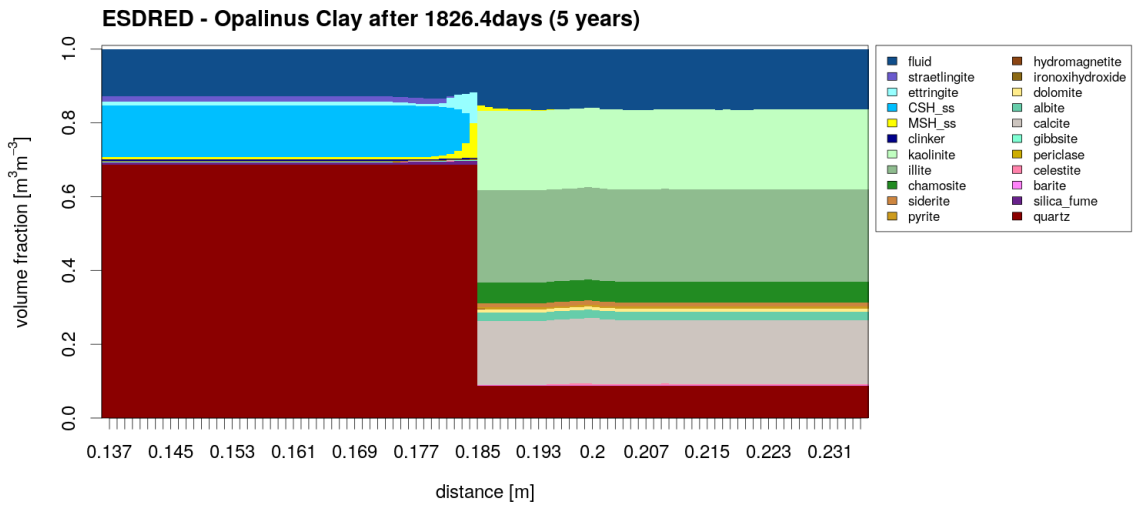

Figure 24.4. *Mineralogical profile across the OPA/ESDRED interface after 5 years of interaction. The interface between ESDRED concrete and OPA is positioned at x = 0.1845 m.*

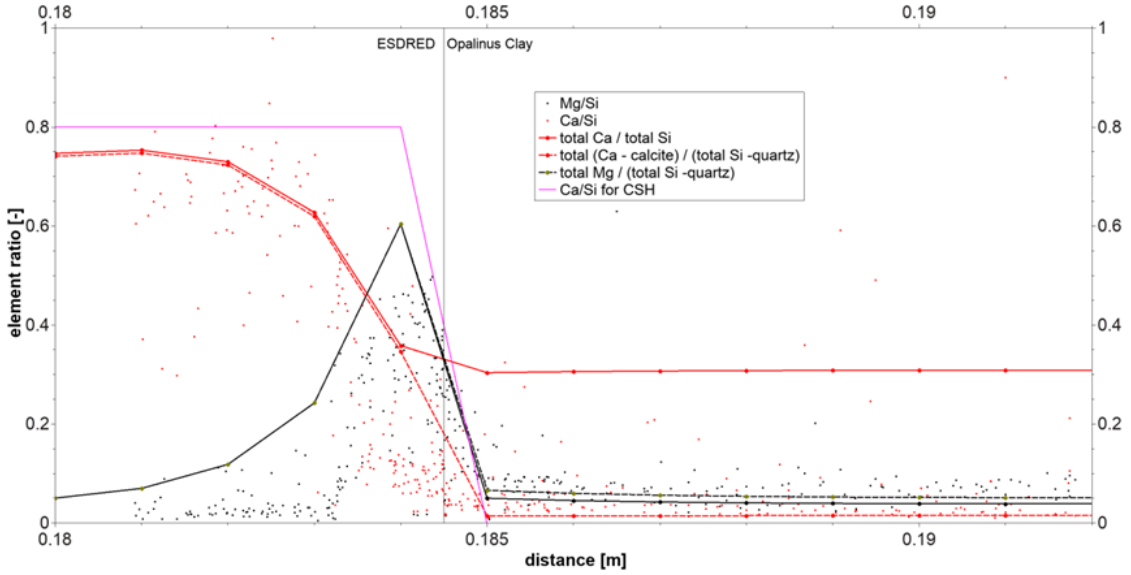

Figure 24.5. *Profiles for Ca/Si and Mg/Si element ratios from experiments (point data) and from model (lines) after 5 years of interaction. The experimental data are courtesy of Andreas Jenni (Univ. Bern). For the different modeled data, see Kosakowski (2018).*

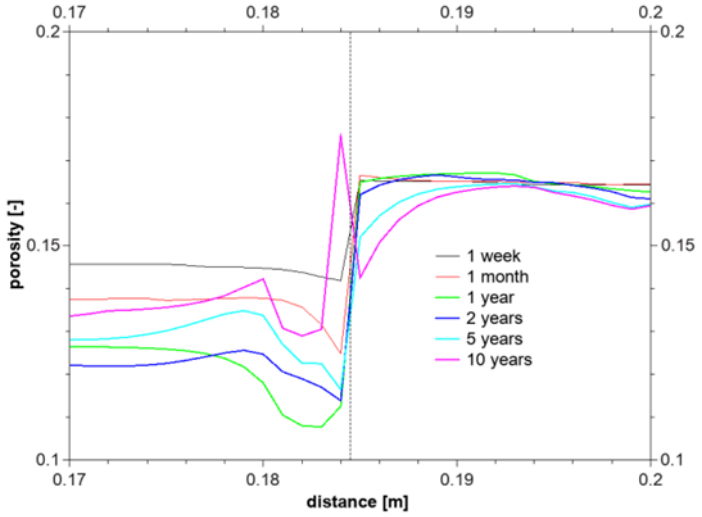

Figure 24.6. *Modeled porosity evolution with time at the ESDRED/OPA interface.*

In order to achieve a good agreement between modelled and experimentally observed behaviour it was necessary to include the cement hydration process in the model. This proved to be very successful for the OPC case, as the kinetic model of Lothenbach (2011b) in combination with the CEMDATA V14 database proved very successful to describe the hydration of the OPC. In agreement with the results of Lothenbach (2011b) the same kinetic model was less good to describe the hydration of ESDRED concrete, because either the kinetic parameters for the dissolution of clinker phases need to be adapted or some relevant intermediately formed cement phases are missing in the thermodynamic setup. Figure 24.7 compares measured concentrations of selected solutes (Lothenbach, 2011a) in batch experiments and the modelled concentration for hydration of ESDRED at the borehole centre (upper part) and near the ESDRED/OPA interface (lower part). The simulation times at which diffusion fronts from Opalinus Clay reach the locations are marked with vertical lines. The borehole centre shows already some significant deviations between measured and modelled concentrations.

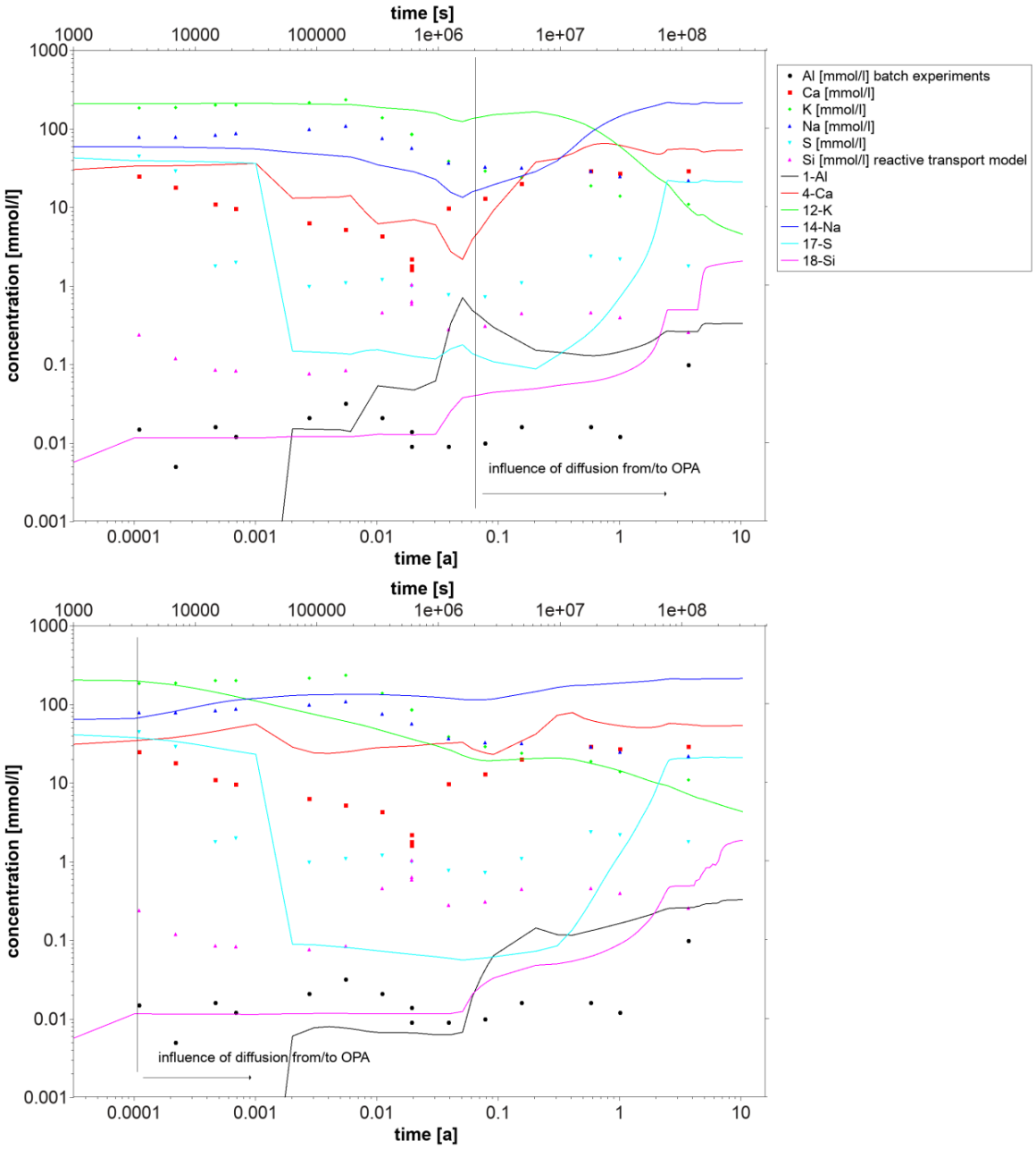

Figure 24.7. *Comparison between measured concentrations of selected solutes (Lothenbach, 2011a) in batch experiments and numerical calculations for hydration of ESDRED at the borehole center (upper part) and near the ESDRED/OPA interface (lower part). Please note the logarithmic scales of time and concentration axes.*

The simulations show that a model without kinetic control of slow reacting phases (like clay, silica) cannot explain the evolution over a period of 5 years for which experimental results are published. On the other hand, cement hydrates are known to react fast and can be largely treated as equilibrium phases. In addition, cation exchange processes in Opalinus Clay and sorption of alkalis on C-S-H are treated with an equilibrium approach. The dissolution of clays and other minerals like zeolites needs restriction by kinetics. There exist some measurements on the kinetic rate constants, but only indirect evidence on the "reactive surface area" in dense clay rocks. Model variants in this work show unrealistic results for models with too high reactivity of clay minerals. In addition, the kinetic control of mineral precipitation on continuum scale is not well investigated. It is known that precipitation is influenced by several sub-grid processes as e.g. pore size distribution (Putnis, 2015),

but applicable approaches for up-scaled (and parameterized) dissolution/precipitation rates in complex media are not yet available. Currently the “reactive surface area” is used as fudge parameter and adjusted for each kinetically controlled mineral phase in order to reach a desired mineral assembly in space and time.

We note that many details of the evolution of clay/cement interfaces are well represented in current state-of-the-art reactive transport models. However, large uncertainties still exist in terms of the temporal evolution of effective parameters like porosity or pH front. This relates to difficulties or even impossibilities to measure directly diffusion or kinetic parameters. Very long-term experiments like the Mont Terri CI-experiments are inevitable, as they offer the possibility to test the process understanding and knowledge about the system. Such long-term datasets offer the only possibility to calibrate model setups and extend predictability beyond the current limit of a few years.

Acknowledgements

The research leading to these results has been partly funded by the European Union's Horizon 2020 Research and Training Programme of the European Atomic Energy Community (EURATOM) (H2020-NFRP-2014/2015) under grant agreement n° 662147 (CEBAMA).

24.4 REFERENCES

Alnæs, M., Blechta, J., Hake, J., Johansson, A., Kehlet, B., Logg, A., Richardson, C., Ring, J., Rognes, M.E., Wells, G.N. (2015). The FEniCS Project Version 1.5. Arch. Numer. Softw. 3.

Glaus, M.A., Aertsens, M., Maes, N., Van Laer, L., Van Loon, L.R. (2015). Treatment of boundary conditions in through-diffusion: A case study of 85Sr2 + diffusion in compacted illite 177–178, 239–248.

Idiart, A.E., et al. (2019). Final Report on the Modelling Task. CEBAMA Deliverable D3.07, Brussels, Belgium.

Jenni, A., Mäder, U., Lerouge, C., Gaboreau, S., Schwyn, B. (2014). In situ interaction between different concretes and Opalinus Clay. Phys. Chem. Earth 70–71, 71–83.

Kosakowski, G. (2018). CI experiment: Reactive transport modeling of interface evolution with OpenGeoSys-GEM (PSI Technical Note TM-44-18-5). Paul Scherrer Institut, Villigen, Switzerland.

Kosakowski, G., Berner, U. (2013). The evolution of clay rock/cement interfaces in a cementitious repository for low- and intermediate level radioactive waste. Phys. Chem. Earth, Parts A/B/C 64, 65–86.

Kulik, D.A., Wagner, T., Dmytrieva, S. V., Kosakowski, G., Hingerl, F.F., Chudnenko, K. V., Berner, U.R. (2013). GEM-Selektor geochemical modeling package: revised algorithm and GEMS3K numerical kernel for coupled simulation codes. Comput. Geosci. 17, 1–24.

Leal, A.M.M., Kulik, D.A., Smith, W.R., Saar, M.O. (2017). An overview of computational methods for chemical equilibrium and kinetic calculations for geochemical and reactive transport modeling. Pure Appl. Chem. 89, 145–166.

Lothenbach, B. (2011a). CI Experiment: Thermodynamic modelling of the hydration of ordinary Portland cement and low-pH cements (Technical note TN 2009-33). Empa, Dübendorf, Switzerland, Switzerland.

Lothenbach, B., Kulik, D.A., Matschei, T., Balonis, M., Baquerizo, L., Dilnesa, B., Miron, G.D., Myers, R.J. (2019). Cemdata18: A chemical thermodynamic database for hydrated Portland cements and alkali-activated materials. Cem. Concr. Res. 115, 472–506.

Lothenbach, B. (2011b). CI experiment: Hydration experiments of OPC, LAC and ESDRED cements: 1h to 3.5 years (Technical Note 2010-75). Mont Terri Project.

Mäder, U., Jenni, A., Lerouge, C., Gaboreau, S., Miyoshi, S., Kimura, Y., Cloet, V., Fukaya, M., Claret, F., Otake, T., Shibata, M., Lothenbach, B. (2017). 5-year chemico-physical evolution of concrete–claystone interfaces, Mont Terri rock laboratory (Switzerland). Swiss J. Geosci. 110, 307–327.

Parkhurst, D.L., Appelo, C.A.J. (2013). Description of input and examples for PHREEQC Version 3 - A computer program for speciation , batch-reaction , one-dimensional transport , and inverse geochemical calculations. U.S.G.S. Tech. and Meth., book 6, chapter A43, 497 p.

Putnis, A. (2015). Transient porosity resulting from fluid-mineral interaction and its consequences. Rev. Mineral. Geochemistry 80, 1–23.

Steefel, C.I., Appelo, C.A.J., Arora, B., Jacques, D., Kalbacher, T., Kolditz, O., Lagneau, V., Lichtner, P.C., Mayer, K.U., Meeussen, J.C.L., Molins, S., Moulton, D., Shao, H., Šimůnek, J., Spycher, N., Yabusaki, S.B., Yeh, G.T. (2015). Reactive transport codes for subsurface environmental simulation. Comput. Geosci. 19, 445–478.

Steefel, C.I., Depaolo, D., Lichtner, P.C. (2005). Reactive transport modeling: An essential tool and a new research approach for the Earth sciences. Earth Planet. Sci. Lett. 240, 539–558.